Development of a software based automatic exposure control system for use in image guided radiation therapy

by

Daniel R. Morton
B.Sc., The University of British Columbia, 2011

A Thesis Submitted in Partial Fulfillment of the
Requirements for the Degree of

MASTER OF SCIENCE

in the Department of Physics and Astronomy

Development of a software based automatic exposure control system for use in image guided radiation therapy

by

Daniel R. Morton
B.Sc., The University of British Columbia, 2011

Supervisory Committee

---

Dr. A. Jirasek, Co-supervisor
(Department of Physics and Astronomy)

---

Dr. W. Beckham, Co-supervisor
(Department of Physics and Astronomy)
(British Columbia Cancer Agency - Vancouver Island Center)

---

Dr. C. Araujo, Departmental Member
(Department of Physics and Astronomy)
(British Columbia Cancer Agency - Center for the Southern Interior)

**Supervisory Committee**

---

Dr. A. Jirasek, Co-supervisor
(Department of Physics and Astronomy)

---

Dr. W. Beckham, Co-supervisor
(Department of Physics and Astronomy)
(British Columbia Cancer Agency - Vancouver Island Center)

---

Dr. C. Araujo, Departmental Member
(Department of Physics and Astronomy)
(British Columbia Cancer Agency - Center for the Southern Interior)

## ABSTRACT

Modern image guided radiation therapy involves the use of an isocentrically mounted imaging system to take radiographs of a patient's position before the start of each treatment. Image guidance helps to minimize errors associated with a patients setup, but the radiation dose received by patients from imaging must be managed to ensure no additional risks. The Varian On-Board Imager (OBI) (Varian Medical Systems, Inc., Palo Alto, CA) does not have an automatic exposure control system and therefore requires exposure factors to be manually selected. Without patient specific exposure factors, images may become saturated and require multiple unnecessary exposures.

A software based automatic exposure control system has been developed to predict optimal, patient specific exposure factors. The OBI system was modelled in terms of the x-ray tube output and detector response in order to calculate the level of detector saturation for any exposure situation. Digitally reconstructed radiographs are produced via ray-tracing through the patients' volumetric datasets that are acquired for treatment planning. The ray-trace determines the attenuation of the patient and subsequent x-ray spectra incident on the imaging detector. The resulting spectra

are used in the detector response model to determine the exposure levels required to minimize detector saturation.

Images calculated for various phantoms showed good agreement with the images that were acquired on the OBI. Overall, regions of detector saturation were accurately predicted and the detector response for non-saturated regions in images of an anthropomorphic phantom were calculated to generally be within 5 to 10 % of the measured values. Calculations were performed on patient data and found similar results as the phantom images, with the calculated images being able to determine detector saturation with close agreement to images that were acquired during treatment. Overall, it was shown that the system model and calculation method could potentially be used to predict patients' exposure factors before their treatment begins, thus preventing the need for multiple exposures.

# Contents

# List of Tables

# List of Figures

# List of Acronyms

**3D-CRT** - 3D conformal radiation therapy
**a-Si** - Amorphous silicon
**AEC** - Automatic exposure control
**CT** - Computed tomography
**DRR** - Digitally reconstructed radiograph
**EBRT** - External beam radiation therapy
**EPID** - Electronic portal imaging device
**HU** - Hounsfield units
**HVL** - Half value layer
**IC** - Ionization chamber
**IGRT** - Image guided radiation therapy
**IMRT** - Intensity modulated radiation therapy
**ISL** - Inverse square law
**KERMA** - Kinetic energy released in the medium
**kVp** - Peak voltage
**mmAl** - Millimetres of aluminium
**MLC** - Multi-leaf collimator
**MRI** - Magnetic resonance imaging
**OAR** - Organ at risk
**OBI** - On-board imager
**PET** - Positron emission tomography
**Poly** - Polystyrene
**PTV** - Planned treatment volume
**PV** - Pixel value
**ROI** - Region of interest
**SAD** - Source to axis distance
**SDD** - Source to detector distance
**SF** - Scatter fraction

**SSD** - Source to surface distance
**SW** - Solid Water
**TPS** - Treatment planning system
**VMAT** - Volumetric modulated arc therapy
**Xi** - Unfors Xi semiconductor diode detector
**Z** - Atomic number

# ACKNOWLEDGEMENTS

I would like to begin by acknowledging the immeasurable amount of support from all of the staff and students within the BCCA-CCSI and BCCA-VIC physics departments that I have had the pleasure of working with. As a student I have met many people who have assisted me in many various ways, all of which are greatly appreciated. Specifically, I want to thank Dr. Andrew Jirasek, Dr. Rasika Rajapakshe, and Dr. Cynthia Araujo for their supervision, guidance, patience, and for the many long discussions that I have enjoyed having with them. I'd also like to acknowledge the financial support and opportunities that were presented to me by the BC Cancer Agency, the BC Cancer Foundation, and the University of Victoria.

Finally, I want to thank my wife, Hailey, and the rest of my family for their unconditional support, assistance, and encouragement during the course of my studies. I can not thank them enough for everything that they have done for me, and I consider myself extremely lucky to have such amazing people in my life.

# Chapter 1

# Introduction

Radiation therapy has evolved into a highly complex process that aims to treat cancerous regions with high doses of radiation while sparing normal, healthy tissue. Due to the small margins and high spatial modulation of radiation treatments, patient setup errors must be minimized. Image guided procedures are implemented in order to ensure that the treatment is being delivered to the exact location that it had been planned. One concern with daily imaging procedures is the increased radiation dose received by the patient which must be managed to ensure no additional risk. Dose reduction includes ensuring that proper imaging techniques are always being used and that no unnecessary exposures are taken. Without a physical automatic exposure control on an imaging system, patient images may become saturated and require multiple exposures before a correct technique is determined. The aim of this work is to develop a software based automatic exposure control system in order to predict patient specific exposure factors that will result in the optimal image being taken on the first attempt.

## 1.1 Radiation Therapy

With the discovery of x-rays and radioactivity in the 1890's, the benefits of radiation in medicine were quickly recognized, which lead to the introduction of radiology and radiation therapy in the early 1900's [1]. Early applications of radiation therapy were limited to the use of low energy x-rays that were useful for the treatment of skin lesions and shallow tumours, but could not be used to effectively treat deep-seated tumours due to the high skin dose that would be received by the patient [2]. The transition of

radiation therapy from a primarily palliative procedure to a major curative treatment began in the 1930's through improved planning of the treatment dose, field size, and patient positioning [3]. The development of the first cobalt-60 treatment units in 1951 in Canada [4, 5] lead to the widespread use of megavoltage (MV) treatment and became the primary device used in external beam radiation therapy for the next 30 years world-wide [2]. High energy x-rays have the advantage of being able to deliver a curative dose to deep seated tumours while sparing the patient's skin as the maximum dose is delivered below the skin surface. The process of utilizing ionizing radiation to cause irreparable damage to cancerous cells is known as radiation therapy, or radiotherapy. Currently, more than half of all cancer patients receive some form of radiation therapy during their treatment and nearly every radiotherapy center in the developed world uses MV radiation which is primarily produced by high energy medical linear accelerators [1–3, 6].

### 1.1.1 Principles of Radiation Therapy

Radiation therapy treatments involve exposing target volumes to high doses of radiation by either directly introducing radioactive material into the tumour in a process known as brachytherapy, or through the use of high energy linear accelerators in a process known as external beam radiation therapy (EBRT). In either method, irradiation of the biological tissue begins a system of biological events that may ultimately lead to cellular death. When the ionizing radiation interacts with the atoms in a cell it produces immediate physical changes by exciting or ejecting orbital electrons which can break chemical bonds and lead to the creation of highly reactive free radicals. These free radicals engage in a chain of successive reactions in order to restore electronic equilibrium. The chemical damage from these reactions may result in lesions in the DNA which, if not fully repaired, leads to the subsequent death of the irradiated cell [6].

The effects of radiation damage are present in both cancerous and normal functioning tissues that are unavoidably exposed to radiation during treatment. Destroying stems cells, and the subsequent losses of the cells that they produce, results in short term side effects such as skin irritation and haemopoietic damage, while damage to functional cells can result in late side effects such as organ damage and even the induction of secondary cancers [6]. The goal of radiation therapy is therefore to achieve local tumour control by destroying tumour cells to prolong a patient's life, but also

to reduce normal tissue complications such that the patient's life is also of a high quality [7]. The two goals conflict due to the proximity of healthy tissue and organs to the target volume, and therefore complex and extensive treatment planning as well as careful delivery must be performed in order to achieve the best possible outcome.

### 1.1.2 Treatment Planning and Delivery

Radiation therapy treatment planning refers to the combined processes from a physician's analysis of diagnostic images to the calculations of dose distributions that make up a patient's treatment [8]. The treatment process generally begins with the generation of a 3-dimensional volumetric data set on which the planning is performed. Currently, computed tomography (CT) is by far the most widely used imaging modality for treatment planning, but other options such as magnetic resonance imaging (MRI) and positron emission tomography (PET) are also available [9]. When the images are taken, the patient is positioned in the proposed treatment position, and may include immobilization devices when needed. The data set is then imported into a computerized treatment planning system (TPS) where oncologists and dosimetrists will contour the planned treatment volume (PTV) and the organs at risk (OAR) and prescribe the dose and dose constraints to each. For conventional 3D conformal radiation therapy (3D-CRT), the standard technique for many treatment sites [9], the contour information is used to select the initial beam configurations and design the fields' energy, size, shape, entry angle, and the addition of any other beam modifiers. The plan is evaluated and modified in order to achieve a sufficiently high dose to the PTV, minimal dose gradient throughout the tumour, a high dose volume that conforms to the PTV, and doses to OARs that are below the set thresholds [8, 9].

With the final evaluation and approval of the treatment plan by the physicists and oncologists, the treatment plan is sent to the linear accelerator to be delivered to the patient, often in multiple fractions over several weeks of treatment. In order for the treatment to be successful, adequate dose must be given to the tumour over each fraction. The clinical target is subject to changes in size and position during the course of treatment and therefore the PTV includes a margin around the target volume to accommodate these variations. In the process of delivering a uniform dose throughout the PTV the surrounding normal tissues are unavoidably irradiated and may result in unacceptably high doses to OARs using conventional 3D-CRT techniques. The large PTV is one disadvantage of 3D-CRT and a reason why radiation therapy has

shifted away from this technique for certain treatment situations that require more conformal delivery [7].

### 1.1.3 Intensity Modulated Radiation Therapy

The probability of local tumour control is directly related to the amount of radiation that a tumour is exposed to, with evidence showing that an increase in dose by 20% can result in a significant increase in tumour control probability [6, 7, 10]. Conventional 3D-CRT is generally operated at the limits of normal tissue tolerance and therefore such dose escalation would not be accepted. This has lead to the development of more conformal external beam radiation techniques that aim to increase the tumour control probability while achieving the same, or less, normal tissue complications as conventional 3D-CRT. With modern advances in treatment planning and delivery, a more conformal dose can be achieved through intensity modulated radiation therapy (IMRT). IMRT offers the ability to shape the high dose region of a treatment to a PTV and can achieve highly uniform coverage of target volumes [2]. The benefits of IMRT have made it the standard treatment for several complicated sites, especially for head and neck treatments partially due to a significant reduction in the severity of xerostomia caused by the irradiation of the parotid glands [11].

The process of IMRT involves delivering multiple fields that are spatially modulated such that each field conforms to the treatment volume. Field modulation is generally done using a dynamic multi-leaf collimator (MLC) which varies the intensity of the radiation at different points in space by sliding small tungsten plates that attenuate the beam at different positions, with millimetre resolution, for varying amounts of time. Modulation allows for the radiation to be shielded over OARs and open over target regions. Smaller doses from a single field can be compensated for by another one of the fields, which are arranged at multiple different angles around the patient. Due to the complexity of the treatment, IMRT uses an inverse planning method. Opposed to traditional forward planning used in 3D-CRT, inverse planning requires the planner to weight doses and dose constraints to the PTV and OARs while an optimizer will calculate the MLC positions required for each field in order to achieve the best dose coverage. One disadvantage of traditional IMRT is the increased treatment time required due to the longer beam times and the multiple gantry angles. Volumetric modulated arc therapy (VMAT) has been developed to reduce treatment time without sacrificing the quality of the delivery [9, 12, 13]. The rapid treatment

time is achieved by delivering the dose in a single, continuous rotation around the patient using similar inverse planning optimization.

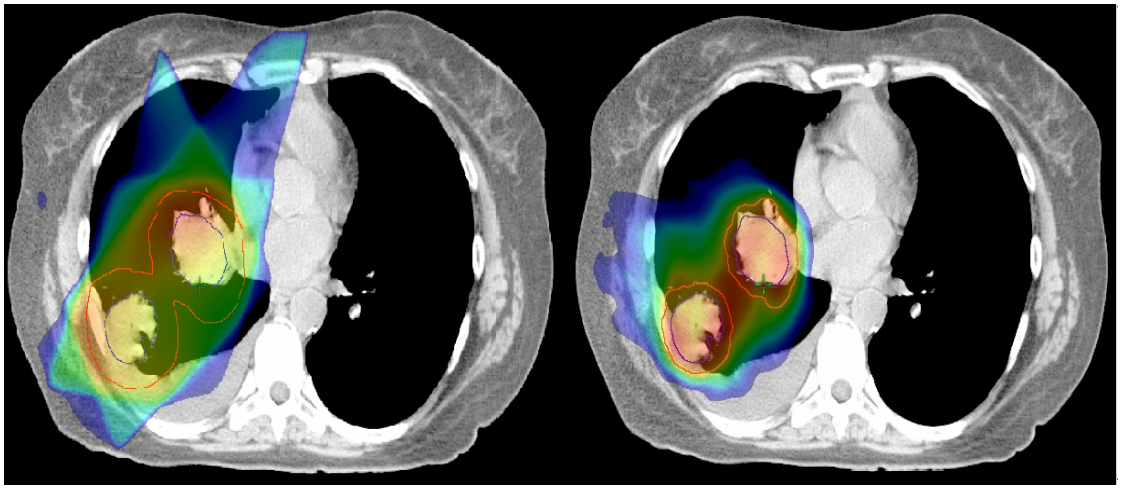

Figure 1.1: Example dose distributions in a lung treatment using 3D-CRT (left) and VMAT (right). The orange contour line in the treated volume corresponds to the PTV and is much smaller on the VMAT plan. Higher doses are shown in red and lower doses in blue.

As with IMRT, VMAT utilizes a highly conformal delivery process that is designed to give a large, uniform dose to the PTV while giving as little dose as reasonably achievable to normal tissues. The dose distributions are able to better conform because these techniques can allow sharp dose gradients near the boundaries of the PTV and OARs (Figure 1.1). Although smaller PTVs result in a significant therapeutic advantage, modulated radiation therapy is therefore also much more sensitive to geometric uncertainties than 3D-CRT methods and the benefits may be lost if the treatment cannot be implemented and reproduced exactly as planned [7, 14].

## 1.2 Image Guided Radiation Therapy

The use of highly conformal radiation in modern external beam treatments requires spatial uncertainties to be minimized. A patient's daily setup may vary on the order of several centimetres and the small margins of these treatments increases the risk of missing the target [15]. The need for spatial conformation has lead to the development of imaging systems mounted on the treatment unit that can be used to image the patient's setup. Imaging allows for the opportunity to visualize the position of a patient's anatomy before treatment begins and to make the appropriate adjustments

to ensure that the PTV is in the correct treatment location. The principle of image-guided radiation therapy (IGRT) is to reduce spatial uncertainties and better account for internal organ motion in order to allow for further dose escalation and conformal planning than IMRT/VMAT alone, and hence achieve a better treatment result [14].


Figure 1.2: Varian iX medical linear accelerator with the portal imaging device (below treatment couch) and on-board imager source (left) and detector (right) extended for image guided radiation therapy. The treatment field which exposes the portal imager emerges from the accelerator head at the top of the image.

Accurate and reproducible positioning of the patient is fundamental to the success of the treatment, especially when dealing with the small margins used in IMRT. Missing a part of a tumour during a few fractions or accidental irradiation of critical structures may reduce the probability of tumour control or increase healthy tissue morbidity, with an error tolerance of only a few millimetres. For example, the area between the 95% isodose line (the area to receive at least 95% of the prescribed dose) and the 50% isodose line may only be 5 mm for a conformal treatment. Therefore, a shift of only 5 mm could result in a portion of the PTV being severely under dosed,

thus risking tumour control. Figure 1.3 shows how a 0.5 cm shift in the field relative to the patient can result in an increased dose to normal tissues while underdosing a volume of the PTV by up to 40% due to the steep gradient at the field edge [16]. Patient offsets in head and neck IMRT treatments using only conventional immobilization and alignment techniques have been shown to average 6.97 mm, resulting in a decrease in the effective uniform dose delivered to the tumour by 3 to 21% depending on the plan and the magnitude of the offset [17]. Such an offset could result in a significant "cold spot" in the target volume which can severely affect the outcome of the treatment. Underdosing 1% of a tumour by 20% can result in an 11% decrease in the tumour control probability [17]. These errors can at least be partially correct for using daily image guidance.

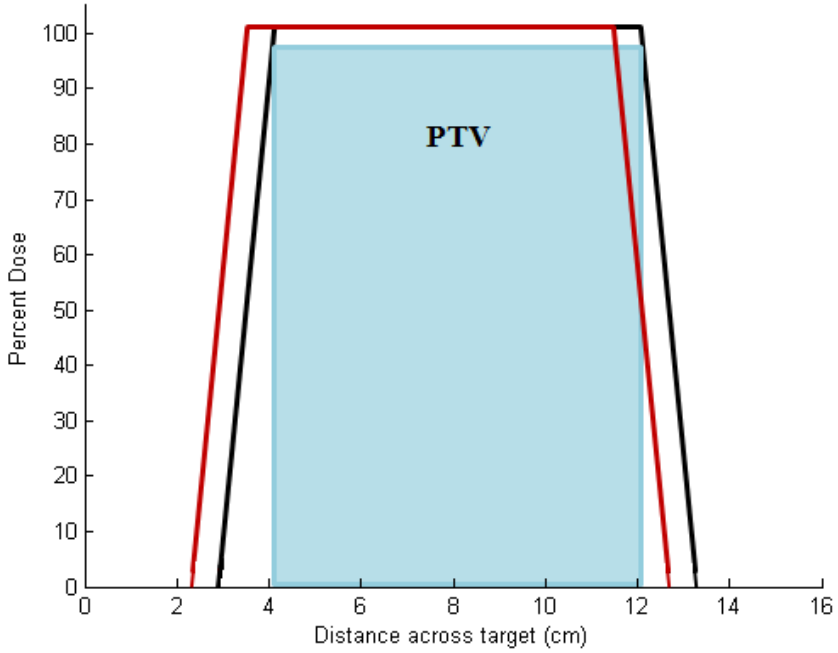


Figure 1.3: The planned field surrounds the PTV at the 95% isodose (black line). A 0.5 cm shift in the field position (red line) results in normal tissues being moved into the field (left) while underdosing the PTV on the right.

Uncertainties in the planning and delivery of radiation therapy are inevitable, which is why various quality assurance processes are used to monitor factors such as dose calculations and variations in machine output [16]. IGRT can be used to account for the various forms of patient uncertainties that may occur daily. Although patients are given setup tattoos and a variety of immobilization devices are used, reproducibility and motion can still result in significant errors. For example, skin

markings may shift relative to deeper tissues and rapid weight loss can create room for movement in the immobilization devices. Both of these can result in variations on the order of 5mm compared to the planned treatment [16]. Organs such as the stomach, bladder, and rectum change size and shape daily, while tumour volumes constantly shrink over the course of a treatment. The movement and shaping of internal structures can create uncertainties on the order of 5 to 10 mm[16]. Since these types of errors can not feasibly be eliminated, they must be accounted for by daily imaging techniques.

### 1.2.1 On-Board Imaging

Early IGRT techniques involved the use of portal images which used a short burst of the treatment beam to expose a film on the exit side of the patient. The radiographic films were compared to simulation films that were created as part of the planning process. Weekly portal image films were generally taken in order to assess the progress of the treatment, but this method did not provide information on the daily positioning errors that could be encountered [2]. The introduction of the electronic portal imaging device (EPID), an imaging system that was attached directly to the gantry of the treatment unit, allowed for quicker image acquisition with setup images generally taken daily, thus being able to detect setup errors prior to each treatment [16]. Figure 1.2 shows an electronic portal imaging device extended below the treatment couch. Advances in technology have enhanced the quality of images that could be taken with the MV beam, but portal images severely lack subject contrast, making images difficult to analyse. The requirement for higher quality images lead to the development of mounted kilovoltage (kV) imaging for use in IGRT.

The Varian on-board imager (OBI) (Varian Medical Systems, Inc., Palo Alto, CA) is a gantry mounted kV imaging system which has a distinct advantage over MV portal imaging due to the significantly improved image contrast [9]. Figure 1.4 shows anterior chest radiographs of two patients taken with MV portal imaging and kV on-board imaging and clearly displays the contrast difference between the two modalities. The increased contrast in kV images makes it much easier to spot setup errors from the daily images. Patient planning is now generally performed using a 3D CT dataset. During planning, a digitally reconstructed radiograph (DRR) will be produced using the CT data. DRRs are simulated 2D projection kV images which are calculated at orthogonal angles representing, for example, a chest and lateral

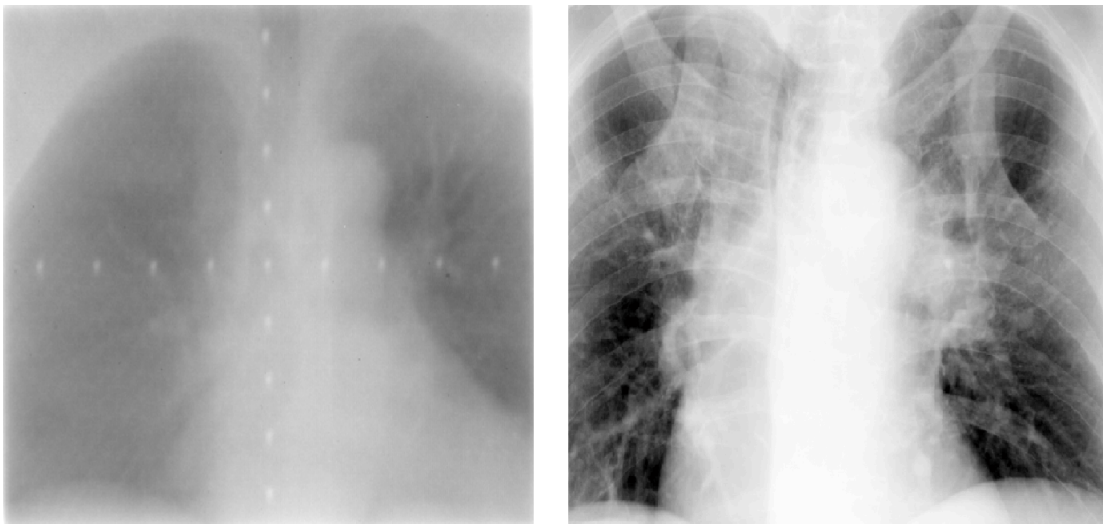

Figure 1.4: Comparison of anterior chest radiographs taken by MV portal imaging (left) and kV on-board imaging (right).

radiograph for a lung patient. Before each treatment the same orthogonal image set will be acquired using the OBI (as shown in Figure 1.2) and compared to the DRRs that show the planned patient position. The acquired images are used with Varian's 2D matching software that verifies the patient's positioning compared to the DRRs created during treatment planning and defines the appropriate adjustments, such as the treatment couch translations, to achieve the optimal positioning for the radiation delivery [18].

### 1.2.2 Imaging Dose

Over the course of radiation therapy treatment a patient may be exposed to multiple sources of imaging radiation. Dose is acquired from diagnostic and planning CTs, as well as the daily imaging used for target localization. Due to the increased amount of imaging dose received by patients in modern radiation therapy it is no longer safe to assume that the cumulative imaging dose is negligible compared to the therapeutic dose [19]. The primary concern with imaging dose is the stochastic risks affiliated with accumulated exposures [20]. Stochastic effects, such as induced cancers and hereditary effects, have no threshold dose that will cause the effect to occur. Instead the probability, not the severity, of a response increases with increasing dose. This is a concern for the large volumes of tissue outside of the treatment field which can be exposed to concomitant dose from scattered radiation and leakage from the treatment

unit as well as the imaging dose received from large field images [19].

During a single fraction of IGRT, a patient will generally receive a pair of orthogonal images. Depending on the treatment site and technique used, the dose to the patient is approximately 1 - 3 mGy per image [19]. With daily imaging, the dose can be repeated over 30 fractions, resulting in a fairly significant out of field dose to the patient. While the imaging dose is small compared to the dose received by the PTV during treatment (approximately 2 Gy per fraction), it is of the same magnitude as the peripheral dose that normal tissues receive during a fraction of IMRT, which has been shown to be relevant when considering the long term health and the risks of induced cancers in radiation therapy patients [20, 21]. Therefore, imaging doses must be managed to ensure as little additional risk to the patient as possible. The general rule in imaging is to keep the dose as low as reasonably achievable [9]. While a trade-off between dose and image quality always exists, the imaging dose in IGRT can be limited by ensuring that the proper techniques that result in the lowest dose possible are always used, and by ensuring that no unnecessary exposures are taken.

## 1.3 Automatic Exposure Control

An automatic exposure control (AEC) is a standard system used in diagnostic radiology. These systems are used instead of manual exposure time settings by monitoring the actual amount of radiation incident on the image receptor and terminating x-ray production when a predetermined level of exposure is reached [22]. The AEC allows the system to automatically compensate for variables such as patient thickness and achieve a consistency in image quality. A very thin patient would receive a shorter exposure than a thicker patient and receive less dose for the same level of image quality. These systems are therefore an important part of dose management in radiography. The AEC will ensure that the lowest dose possible is delivered to the patient in order to achieve a useful image. They are also important in ensuring that the imaging detector does not saturate. Modern digital detectors have a saturation point where additional exposure will not result in a change in the image. The AEC can be set to terminate an exposure before the detector will saturate because no information is gained from a saturated image. Saturation can be a common occurrence in chest radiography due to the fact that the lungs do not highly attenuate the radiation and therefore the detector will be overexposed in the lung regions. In IGRT, the important part of the image is the visibility of structures which can be lined up to

ensure proper patient positioning. Structure alignment can not be done if the image is saturated because important anatomical information that would be used for image matching will be removed from the image. When the image quality is not of a high concern, the AEC could be set to a lower level, ensuring that the image is of high enough quality to be used for the procedure while still limiting the dose as much as possible and completely preventing imager saturation.

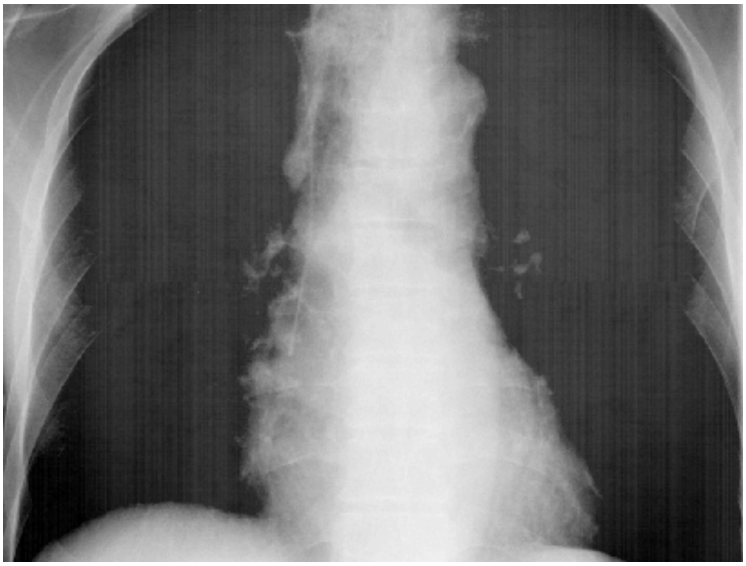

Figure 1.5: An anterior chest radiograph shows how detector saturation can compromise image matching by eliminating anatomical structure information from the image.

The Varian OBI used for IGRT is a standard kV imaging device which lacks an AEC. Exposure techniques must be selected manually from technique factor tables. These tables are based on global population data and may not be optimal for certain individual patients. Since the exposure factors are not patient specific, the resulting images may be over or under exposed. Figure 1.5 shows how an over-exposure can saturate an image and remove important anatomical information when compared to a optimally exposed image such as the kV radiograph shown in Figure 1.4. Such exposures result in suboptimal images being used for image matching and may require additional exposures until the proper technique for the patient is determined. Repeated exposures violates the principle of keeping imaging dose as low as reasonably achievable. If a saturated image is acquired then by definition the exposure was higher than necessary. If the image is saturated to the point where it cannot be used for image matching then the entire exposure has added additional dose that has

no benefit to the treatment because a new image must be taken. In certain treatment situations images can be acquired multiple times before the proper technique is found. In addition to the dose given to the patient, repeated exposures can severely impact the treatment time. While a patient is immobilized while waiting for an IMRT treatment, the additional time that it takes to acquire multiple images can risk the comfort and positioning of the patient. A unique opportunity exists in IGRT in that every patient has a planning CT dataset, something that is not generally available in standard radiography. Access to the patients' CT information is beneficial because this data can be used to analyse the anatomy and attenuation properties of a patient before imaging.

## 1.4 Thesis Scope

The objective of this thesis is to develop a software based AEC in order to predict the optimal, patient specific exposure factors so that the techniques required for the best image can be determined before treatment begins, thus preventing the need for multiple unnecessary exposures. Predicting the exposure factors is done by simulating a kV exposure through the CT data and determining how the patient will attenuate an x-ray spectrum. The attenuation data is used in combination with a model of the OBI, based on system output and detector response, to determine the level of detector saturation per unit exposure time. By setting a desired saturation level, the optimal exposure can then be calculated. These calculations are tested by evaluating the simulation's performance for various phantom studies as well as comparing the calculated images to patient images that were acquired during IGRT treatments.

The next chapter of this work will provide an overview of the fundamental physics and imaging principles used in kV imaging. This includes the interactions that result in x-ray production and image creation, as well as a description of the Varian OBI system. Chapter 3 will describe the measurement processes used in modelling the OBI, and the algorithm developed to generate quantitative DRRs. Chapter 4 presents the experimental system model results, while the results of the DRR calculations and their comparisons to phantom and clinical images are presented in Chapter 5. These results, their success, and their significance are discussed in Chapter 6, and Chapter 7 concludes the work and discusses future considerations.

# Chapter 2

# Background

The presented research aims to model and simulate the interactions and processes involved in producing radiographic images in order to predict the detector response before an actual image is taken. The following chapter explains the relevant physics and imaging principles necessary to understand how radiographic images are formed. Background information includes a description of the x-ray production and detection, as well as an overview of automatic exposure control systems and the Varian OBI.

## 2.1 Particle Interactions

Medical imaging is based on the fundamental interactions of photons and electrons with matter. The useful electron interactions in diagnostic imaging are limited to the creation of x-rays, while the photon interactions involve the removal of these x-rays from the primary beam as they are attenuated by the material. The level of attenuation of the x-rays is what ultimately leads to the formation of an image.

### 2.1.1 Electron interactions

The interactions of high energy electrons with matter are essential for the process of medical imaging. When an electron travels through a medium it may undergo a large number of different encounters or collisions. A single 100 keV electron may have 1000 individual interactions before it comes to rest [23]. The majority of electron interactions will be small energy exchanges with orbital electrons which leads to the ionization of the atoms. With a large enough energy transfer, the resulting secondary electrons may go on to ionize other atoms as well. Ionizations, which lead to the sub-

sequent biological damage in cells, are important when considering the dose delivered to a patient, but not for image formation. The important electron interactions in radiography are the rare events resulting in the production of x-rays.

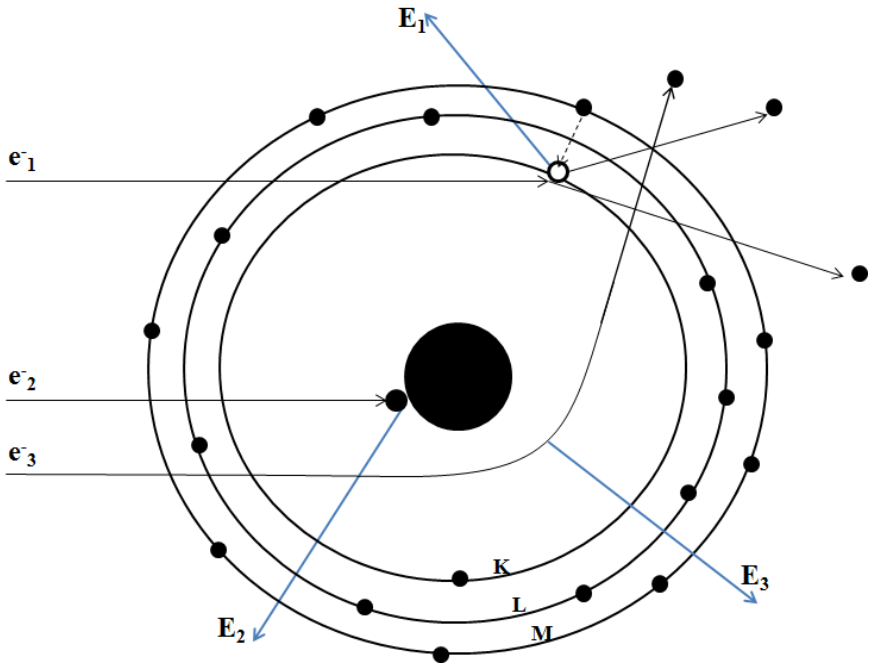


Figure 2.1: High energy electrons ($e^-_{1,2,3}$) interact with an atom to produce characteristic ($E_1$) and bremsstrahlung ($E_{2,3}$) x-rays.

A free electron ($e^-$) can be accelerated to high energies and collide with a target material (discussed further in Section 2.2), producing a spectrum of x-rays. Figure 2.1 shows the different types of electron interactions within an atom that can result in the production of x-rays. An incident electron ($e^-_1$) may collide with an orbital electron, and if its energy is greater than the energy that binds the electron to its orbit then the electron will be ejected from its shell. The ejected electron leaves a hole in the shell which will be filled by an atomic electron from an outer shell, resulting in the production of an x-ray ($E_1$) with an energy that is equal to the difference in the binding energies of the two shells. The x-rays that are produced are called "characteristic" because each element has its own unique binding energies for each shell, and therefore the energies of the x-rays are characteristic to the atom. For example, a tungsten atom that loses a K-shell electron (70 keV) can be filled by the adjacent L-shell electron (11 keV) and emit a 59 keV photon, referred to as a $K_\alpha$ emission [24]. The hole could instead be filled by an M-shell electron (3 keV) and

emit a 67 keV $K_\beta$ photon ($\beta$ meaning that the hole was filled by an electron that is 2 or more shells away) [24]. This process can cascade to more distant shells until a hole in the outermost shell is filled by a free electron. The electrons in the same shell also have minor differences in binding energies, so the same transition can produce x-rays with slightly different energies. For example, the $K_\alpha$ emission of a tungsten nucleus will be either 59.32 keV or 57.98 keV [24]. Variations in the binding energies, while existent, are generally not resolved for other transitions due to the very small differences in binding energies.

The number of orbital electrons and electron shells increases with an element's atom number ($Z$), so a higher Z material can therefore produce a large variety of characteristic x-rays, although the differences in binding energies for outer shells are very small. An N-shell to M-shell transition in tungsten will only result in the production of a 2.5 keV x-ray [24]. If one of the characteristic x-rays is absorbed by an outer shell electron, then the electron will be released with an energy equal to the difference between the characteristic energy and the binding energy of the ejected electron. The electron, known as an Auger electron, will proceed to interact further in the material.

Also shown in Figure 2.1 is the production of bremsstrahlung x-rays. Bremsstrahlung production occurs when electrons ($e_2^-$ and $e_3^-$) travel close to the nucleus and are decelerated by the nucleus's positive charge, causing the electrons to radiate energy as they experience a change in velocity [24]. A deflected electron ($e_3^-$) will emit a small fraction of its initial kinetic energy as a bremsstrahlung x-ray ($E_3$) and then continue to interact with other atoms in the material. Electrons that travel closer to the nucleus will experience a greater change in velocity and therefore produce a photon with higher energy [23]. The upper limit of bremsstrahlung production is therefore the rare occurrence when an electron ($e_2^-$) collides directly with a nucleus and comes to a complete stop where it emits its total kinetic energy as an x-ray photon ($E_3$) [23]. The total intensity of bremsstrahlung radiation produced by charged particles with mass $m$ and charge $ze$ is proportional to:

$$I_{bremsstrahlung} \propto \frac{Z^2 z^4 e^6}{m^2} \tag{2.1}$$

where the target nuclei has a charge of $Ze$ [24]. Equation 2.1 shows that electrons ($m$ = $9.11\times10^{-31}$ kg) are much more efficient at producing bremsstrahlung than heavier particles such as protons ($m = 1.67\times10^{-27}$ kg), and that high $Z$ targets will increase

the intensity of bremsstrahlung production.

### 2.1.2 Photon Interactions

The x-ray photons used in medical imaging can undergo several different types of interactions that will lead to their attenuation from the primary path while travelling through a medium. Interactions can involve the entire energy of the photon being deposited in the medium, or the scattering of the photon from its primary path. At the energies used in medical imaging, four different photon interactions can occur. Three of these interactions involve the transfer of energy to the medium, while the fourth (Rayleigh scattering) only involves the elastic scattering of the photon. The important interactions involved in the production of kV images, the focus of this thesis, are the photoelectric effect and Compton scattering.

#### Rayleigh Scattering

Rayleigh scattering, also known as coherent scattering, is a photon interaction that occurs primarily at low energies. In the scattering process, ionization of an atom does not occur. Instead all of the energy from an incident photon is redirected, or scattered, in the medium. Coherent scattering occurs when the oscillating electric field of the photon causes the electrons in an atom to vibrate. These oscillating electrons emit radiation that combines to form the scattered wave with an energy equal to the incident photon's energy, but travelling in a different direction [23]. Rayleigh scattering is predominately a low energy interaction and is more likely to occur in high-Z materials. Less than 5% of the photon interactions that occur in soft tissue above 70 keV, and only about 10% of interactions at 30 keV, will be Rayleigh scattering [22]. Therefore, Rayleigh scattering does occur in kV imaging, but it has a small overall effect.

#### Photoelectric Effect

The dominant interaction in the medical imaging is the photoelectric effect. This process involves the collision between a photon and an atom in which the photon is completely absorbed and all of its energy is transferred to a bound electron [23]. The electron will eject from the atom with kinetic energy equal to the difference between the incident energy of the photon and the binding energy of the electron shell. The ejected photoelectron will proceed to interact with additional atoms in the medium.

The ejection of an electron leaves a vacancy in the shell, resulting in the production of characteristic x-rays in the same process described in Section 2.1.1.

The photoelectric effect is most likely to occur when the incident photon's energy is equal to the binding energy of the electron that it interacts with [24]. If the photon's energy is less than the binding energy of the electron then a photoelectric interaction is energetically impossible, but the probability of an interaction occurring also decreases as the incident photon's energy increases above the binding energy. Therefore, photoelectric interactions are more likely to occur in kV imaging than in MV imaging or radiation therapy. The probability of a photoelectric interaction is also highly dependent on the atomic number of the atom that the photon interacts with. The interaction's dependence on the atomic number, empirically observed to be approximately proportional to $Z^3$, results in the large differences in x-ray attenuation between bone and soft tissues seen in radiographic imaging (discussed further in Section 2.1.2) [23].

### Compton Scattering

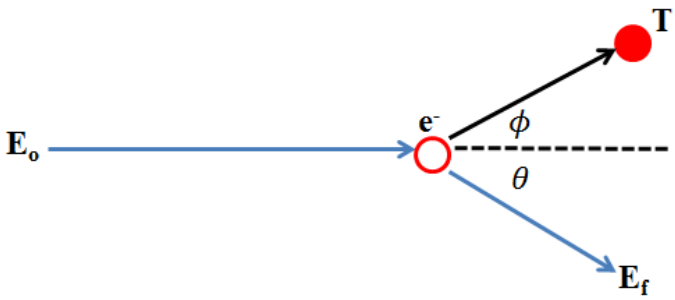


Figure 2.2: Compton scattering between an incident x-ray and a free electron.

The other predominate photon interaction in kV imaging is Compton (incoherent) scattering. Compton scattering involves the collision of a photon with an electron, typically when the photon's energy is much greater than the binding energy of the electron. Scattering generally occurs with outer-shell, essentially free, electrons due to their relatively low binding energies [24]. Figure 2.2 shows an incident photon with an energy of $E_o$ colliding with a free electron ($e^-$). The electron is set into motion with a kinetic energy of $T$ travelling away from the collision at an angle of $\phi$. The scattered photon, having transferred some of its energy to the electron, will be left with a reduced energy of $E_f$ travelling away from the collision at an angle of $\theta$. The

relationship between fractional energy loss of the photon and its scattering angle is

$$\frac{E_f}{E_o} = \frac{1}{1 + \frac{E_o}{m_o c^2}(1 - cos\theta)} \tag{2.2}$$

where $m_o c^2$ is the 511 keV rest mass energy of an electron [24]. Since energy is conserved in the collision, the energy of the recoil electron is equal to the difference between the incident and final photon energies ($T = E_f - E_o$).

The probability of a Compton interaction occurring in a material is dependent on the electron density of the material (number of electrons per gram times the density of the material) [22]. The scattering angle, and thus the energy transferred to the electron, is dependent on the incident photon's energy. As the energy increases, Compton scattering is more forward peaked, meaning that the scattered photon is more likely to continue in the direction that the incident photon was travelling. In high energy collisions, more energy is transferred to the scattered electron. Equation 2.2 shows that a 100 keV photon scattering at 60 degrees will retain more than 90% of its energy, while a 5 MeV photon scattering at the same angle will be left with only 17% of the incident energy after the collision [22]. Therefore, at the lower energies that are used in kV imaging, the majority of the energy will be transferred to the scattered photon. Therefore, even with maximum energy losses the scattered photons may have high enough energies to continue to travel through tissue. Therefore, scattered photons can possibly reach the imaging detector after they have already been attenuated from the primary beam. The effect of scatter on radiographic images will be discussed more in Section 2.3.1.

### Pair & Triplet Production

The last high energy photon interactions that can occur in matter are pair production and triplet production. Pair production occurs when an x-ray interacts with the electric field of the nucleus. The photon's energy is transformed into an electron-positron pair which will go on to interact in the medium. Since the photon's energy is being converted into the rest mass energy of a positron and an electron (511 keV each), the minimum energy threshold for pair production to occur is 1.022 MeV [23]. If the photon's energy is greater than 1.022 MeV, then the remaining energy will be split between the electron and positron. A high energy photon may also interact with an atomic electron instead of the nucleus. The interaction results in the

creation of an electron-positron pair, as well as the ejection of the orbital electron in a process called triplet production with a minimum energy threshold of 2.04 MeV (due to the conservation of momentum in the interaction) [24]. The work in this thesis only involves kV diagnostic imaging, so the energy thresholds for pair and triplet production are not met and hence do not occur.

### Linear Attenuation

As an x-ray beam travels through matter, the individual photons will be attenuated by the processes previously described. Attenuation means that the photons are removed from the incident primary path, either by being completely absorbed or scattered. The probability of an interaction occurring per centimetre thickness of matter is called the linear attenuation coefficient, $\mu$ ($\mathrm{cm}^{-1}$), and is unique to every type of material. The attenuation coefficient is also highly energy dependent, as high energy x-rays are generally less likely to be attenuated than low energy x-rays. The total probability of an interaction occurring is equal to the combined probabilities of each individual interaction, such that

$$\mu = \tau + \sigma_{coh} + \sigma_{inc} + \kappa \tag{2.3}$$

where $\tau, \sigma_{coh}, \sigma_{inc}$, and $\kappa$ represent the probabilities of photoelectric, Rayleigh, Compton, and pair production occurring, respectively. Therefore, the change in the number of photons ($\mathrm{d}N$) as a beam of $N$ photons travels through a thin slab of material ($\mathrm{d}X$) is given by

$$\mathrm{d}N = -\mu N \mathrm{d}X. \tag{2.4}$$

Integrating Equation 2.5 over the entire thickness of material gives the Lambert-Beer law for exponential attenuation [24]

$$N = N_o \, e^{-\mu t} \tag{2.5}$$

where $N$ is the number of photons remaining after $N_o$ photons travel through a thickness, $t$, of material. Since the attenuation coefficients are unique for every type of material, a photon beam travelling through a series of $n$ different materials with different thicknesses will be attenuated by the exponential product of each:

$$N = N_o \, e^{-\sum_{i=1}^{n} \mu_i t_i}. \tag{2.6}$$

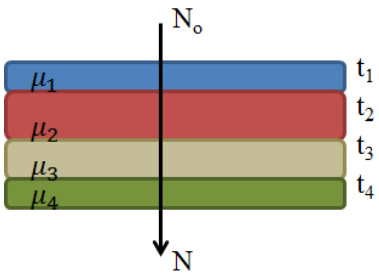


Figure 2.3: Attenuation of a primary beam of photons through a stack of different materials.

For example, applying Equation 2.6 to the material in Figure 2.3, the primary beam will be attenuated by

$$N = N_o \, e^{-(\mu_1 t_1 + \mu_2 t_2 + \mu_3 t_3 + \mu_4 t_4)}. \tag{2.7}$$

The attenuation through various types and thicknesses of materials is what ultimately leads to the creation of x-ray images.

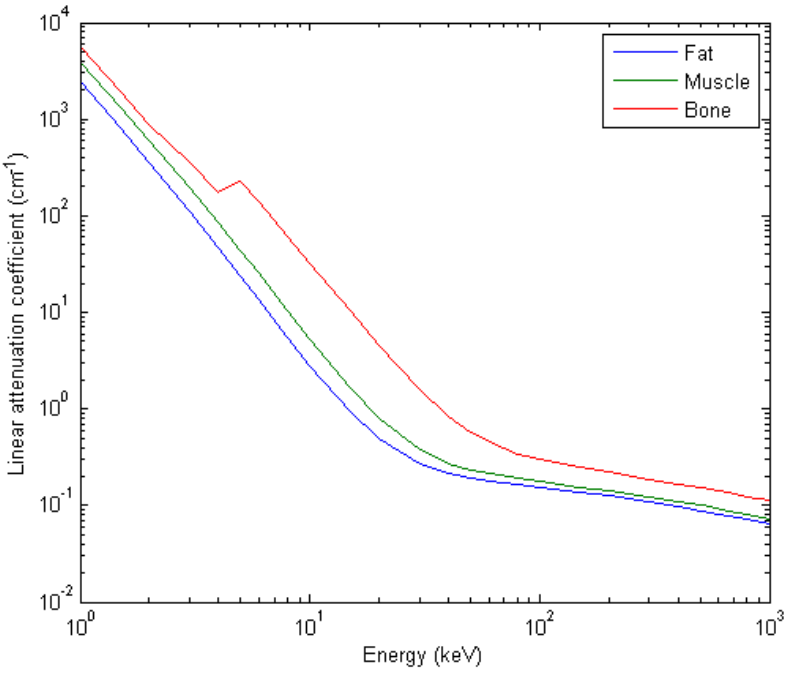


Figure 2.4: Attenuation coefficient of fat, muscle, and bone from 1 to 1000 keV (Johns and Cunningham, 1983).

Figure 2.4 shows how different materials can result in differences in photon attenuation. In the diagnostic imaging range (30 to 120 keV), photons are much more

likely to interact in bone than in muscle and fat. At higher energies, the attenuation coefficients appear closer together and is the cause of the low contrast of MV imaging. The probability of an interaction occurring is greater at lower energies. An exception of this trend can be seen in the spike in the attenuation coefficient of bone at approximately 4.1 keV due to the increased probability of photoelectric absorption for photons with energies near the K-shell binding energy.

## 2.2 X-ray Production

### 2.2.1 kV x-ray tubes

The fundamental interactions that lead to the production of high energy photons has been described in Section 2.1.1. These interactions are implemented in diagnostic radiology in order to create the x-rays that are used for imaging. In order to acquire enough energy to produce x-rays, the electrons are required to be accelerated, generally through the use of an x-ray tube. Figure 2.5 is a schematic diagram of the functional components of a standard x-ray tube used in radiography.

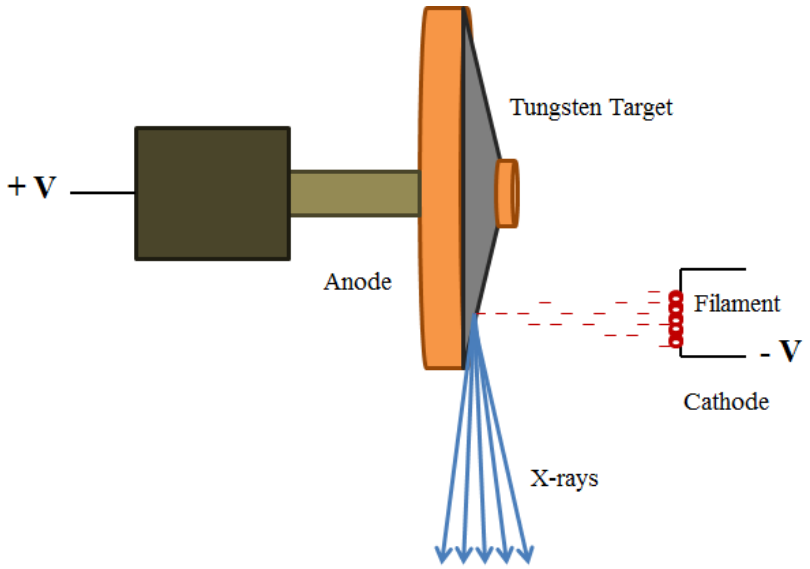


Figure 2.5: Schematic diagram of an x-ray tube used for radiography.

X-ray production begins in the cathode, which is the negative voltage pole of the circuit. The cathode contains a tungsten filament that is heated by passing a filament current of around 5 A at 10 V through it [24]. As the filament is heated, electrons are

emitted from it in a process called thermionic emission, which results in a cloud of electrons forming around the filament. These electrons are then accelerated towards the positively charged pole of the high-voltage circuit (anode). The x-ray tube current (mA) determines the number of electrons per second that are accelerated, where 1 mA is defined as $6.24\times10^{15}$ $e^-/s$ [22]. The amount of energy obtained by these electrons depends on the potential difference between the cathode and anode. An electron that is accelerated by 100 kV of applied potential will reach the anode with 100 keV of kinetic energy. The maximum energy that an electron can obtain is defined by the peak voltage (kVp) of the x-ray tube.

When the electrons collide with the anode they produce x-rays via the processes described in Section 2.1.1. In order to increase the efficiency of x-ray production, as shown in Equation 2.1, the anode target is generally made of tungsten due to its high atomic number ($Z = 74$). Tungsten is also used because it has a high melting point (3300°C) which helps to prevent damage to the anode due to the large amounts of heat that is produced during x-ray production. Heating effects are also minimized through the use of a rotating anode design. Rotation of the contact surface allows the heat to dissipate over the anode, instead of at a single point. X-rays are produced isotropically within the anode, which is slightly angled (7 to 20 degrees) in order to improve heat dissipation and increase the effective field-of-view due to the attenuation of the beam on the anode side [22]. The resulting cone-shaped beam exits the tube after it passes through various filters and is collimated to the appropriate size.

### 2.2.2 X-ray tube output

The x-rays produced by an x-ray tube are not monoenergetic, and instead emerge as a spectrum of energies. The maximum energy of a bremsstrahlung x-ray is equal to the energy of an electron when it collides directly with a nucleus, and the electron's maximum energy is defined by the kVp of the x-ray tube. Therefore, when a tube potential of 100 kVp is used, the absolute maximum energy x-ray that can be produced is 100 keV. Figure 2.6 shows the theoretical unfiltered 100 kVp bremsstrahlung spectrum. Glancing interactions are the most likely to occur so there are many more low energy photons produced than the high energy photons that are created from rare direct collisions. Figure 2.6 also shows an example of a spectrum that may actually emerge from an x-ray tube. Due to the fact that low energy x-rays have almost no chance of passing all the way through a patient and reaching the detector, filters are

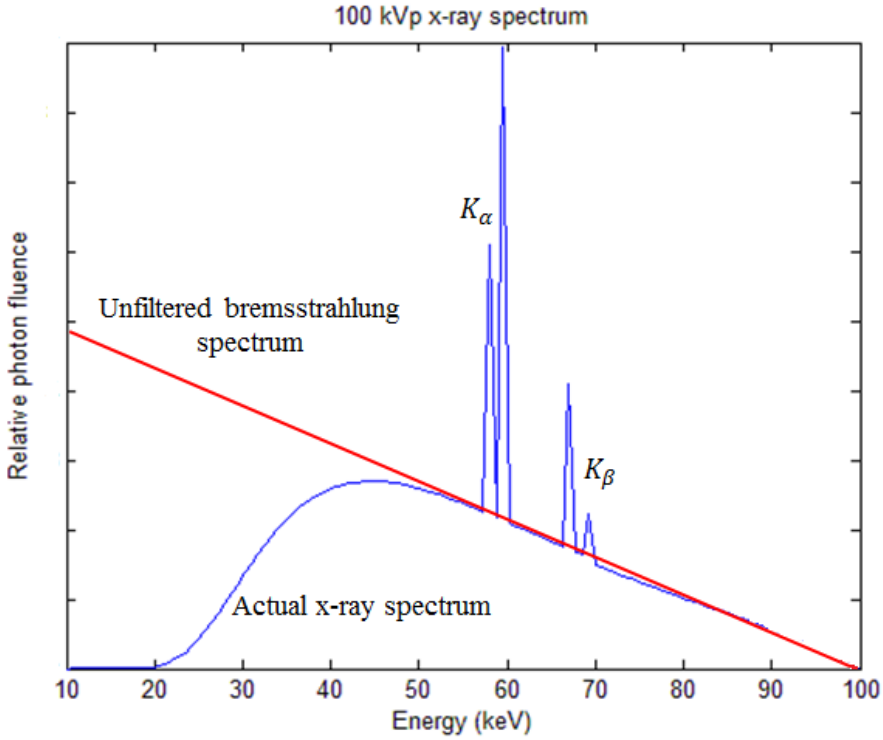


Figure 2.6: A comparison of a theoretical bremsstrahlung spectrum to the spectrum that actually emerges from an x-ray tube.

generally added to the x-ray tube in order to remove these x-rays from the spectrum. Inherent filters such as the exit window of the tube and even the anode itself remove some of these low energy x-rays as well [22]. The filtered bremsstrahlung spectrum in Figure 2.6 also includes the K-shell characteristic x-rays. The characteristic x-rays produced in the anode appear as large spikes on the spectrum due to the high probability of K-shell transitions. These spikes occur in doublets due to the slight differences in binding energies within a shell.

The number of photons at each energy is directly proportional to the number of electrons used to produce the x-rays. A higher tube current results in a higher number of electrons being accelerated from the cathode to anode, and a longer exposure duration will increase the amount of time for x-ray production to occur. Doubling the tube current will result in the same increase in the number of x-rays being produced as doubling the exposure time since both will double the number of electrons being used. Therefore, the spectrum can be scaled by the milliampere seconds (mAs) of the exposure, which is the product of the tube current (mA) and the exposure time

(s). Changing the mAs of an exposure will change the amount of photons that are produced at each energy, but the overall shape of the spectrum will be maintained.

The half-value layer (HVL) of a spectrum is used to define the *beam quality* of an x-ray beam. The quality of a beam generally describes the penetrating ability and the effective energy of the spectrum. A particular x-ray beam's HVL is the thickness of material, typically aluminium (Al), that is required to reduce the intensity of an exposure to one half of its initial value. Since the attenuation coefficients are dependent on energy, the HVL gives an indication of the energy distribution of the beam. A higher HVL implies that more photons are passing through the material unattenuated, and therefore the beam has an overall higher energy. As an x-ray beam passes through additional material, like the filtration in the x-ray tube, more low energy photons are removed from the spectrum than high energy photons. Therefore, the average energy of the spectrum, and subsequently the HVL, increases. The process of removing low energy photons from a spectrum is known as beam hardening.

As an x-ray beam travels through a medium, some of its energy is transferred to charged particles via the processes described in Section 2.1.2. The amount of energy transferred is called the *KERMA*, which is an acronym that stands for the kinetic energy released in the medium. The KERMA is measured in grays (Gy), where 1 Gy is equivalent to 1 joule (J) of energy transferred to charged particles in 1 kg of matter. For an x-ray spectrum that contains energies 0 to $E_{max}$, the KERMA ($K$) can be calculated by:

$$K = \int_{E=0}^{E_{max}} E\ \Phi(E) \left( \frac{\mu_{tr}(E)}{\rho} \right)_{med} \mathrm{d}E \tag{2.8}$$

where $\Phi(E)$ is the fluence (photons/cm$^2$) of photons with energy $E$, and $\left(\frac{\mu_{tr}(E)}{\rho}\right)_{med}$ is the mass energy transfer coefficient of the medium at energy $E$ [24]. The mass energy transfer coefficient is the fraction of the linear attenuation coefficient (normalized by the material's density) that is transferred to the kinetic energy of charged particles in the medium. In diagnostic radiology the KERMA in air can be used to describe the output of an x-ray tube. Roentgens (R) can also be used to describe the system's output by measuring the exposure, or the charge created per unit mass, in air due to ions created from the x-ray interactions. An exposure ($X$) can be converted to air

KERMA using

$$K(\text{Gy}) = X(\text{R}) \times 2.58 \times 10^{-4}\text{C/kg} \times 33.97 \text{ J/C}, \tag{2.9}$$

where 1 R is equal to $2.58 \times 10^{-4}$ C of charge created in 1 kg of air, and it takes 33.97 eV to produce an ion pair in air, which is equivalent to 33.97 J/C [22]. The product results in the energy absorbed in air per unit mass (J/kg). Due to the low energies of diagnostic x-rays and the low-$Z$ absorbers in air, radiative losses from the electrons emitting bremsstrahlung are negligible. Therefore, the energy absorbed in air is essentially equivalent to the energy transferred to charged particles in air, or the air KERMA [22]. The KERMA and exposure are directly proportional to the mAs used in x-ray production, and therefore the system's output is defined as an exposure per mAs (mR/mAs), or in $\mu$Gy/mAs of air KERMA.

## 2.3 Radiographic Imaging

### 2.3.1 Imaging Principles

Radiography involves passing x-rays through a three-dimensional object in order to create a two-dimensional image. The photons emerge from an isotropic point in the x-ray tube and travel in straight lines, resulting in a cone of x-rays. By placing an object between the source and detector, these x-rays are attenuated and removed from the primary path. X-rays travelling through different parts of the object will be attenuated by various amounts depending on the thickness and attenuation properties of the materials, as explained in Section 2.1.2. Differences in attenuation result in the spectra that emerge from the object to vary in terms of the photon fluence and energy distribution at different points on the detector. The spectral differences result in a difference in the exposure at the corresponding detector points, thus creating contrast in the radiographic image. Tissues that attenuate similar amounts of x-rays, such as muscle and fat, can appear very similar to each other in a radiograph. However, dense bones can attenuate much more radiation and therefore will have a high contrast when compared to soft tissues (Figure 2.4).

The divergence of a typical beam, shown in Figure 2.7, results in a change in the field size depending on the distance from the source. The field size on the OBI system is defined at the point of intersection between the central ray and the axis of rotation

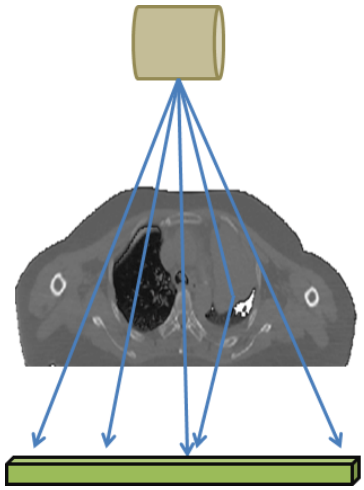

Figure 2.7: X-rays travelling from the source to the detector in a straight line will reveal anatomical information about the patient. Scattered photons contribute a signal to the detector that contains no information about the attenuation along the path.

of the system, known as the isocenter. The cone-shaped beam will therefore result in magnification in the image. An object that is imaged close to the source will appear larger than when the same object is imaged closer to the detector. Because the beam diverges, the intensity of the x-rays also decreases with increasing distance from the source. If the x-ray source is considered an isotropic point, the area over which the radiation is distributed increases by the square of the distance from the source and therefore the intensity of the radiation decreases at the same rate [22]. This principle is known as the *inverse square law* (ISL):

$$X_2 = X_1 \left( \frac{d_1}{d_2} \right)^2 , \tag{2.10}$$

where $X_2$ and $X_1$ are the exposures rates at distances $d_1$ and $d_2$. Therefore, doubling the distance from the source will decrease the exposure by a factor of 4, while halving the distance from the source will increase the exposure by a factor of 4.

Figure 2.7 shows several rays travelling from the x-ray source to the x-ray detector while passing through a patient at different points. Since primary x-rays travel in straight lines, each point on the detector will correspond to one particular ray of photons. Detecting these primary photons will reveal the anatomical information about the patient by determining the level of attenuation along that ray. Scattered radiation violates the premise that radiation travels in straight lines. The scattered photon

in Figure 2.7 will contribute a signal to the point on the detector that corresponds to the central ray. However, the scattered signal contains no information about the attenuation along the central ray and is therefore detrimental to the image. Signals from scattered radiation result in reduced image contrast and additional noise [22]. The scatter fraction ($SF$) can be defined by:

$$SF = \frac{S}{S+P}, \tag{2.11}$$

where $S$ and $P$ are the signals from the scatter and primary photons, the sum of which equals the total detected signal. As the object thickness and the size of the field on the object increase, the scatter fraction typically increases (up to a saturation limit) due to the presence of more scattering material [22, 25]. The scatter fraction also slightly increases with increasing x-ray tube voltage, but is nearly constant across the range used in diagnostic imaging [25].

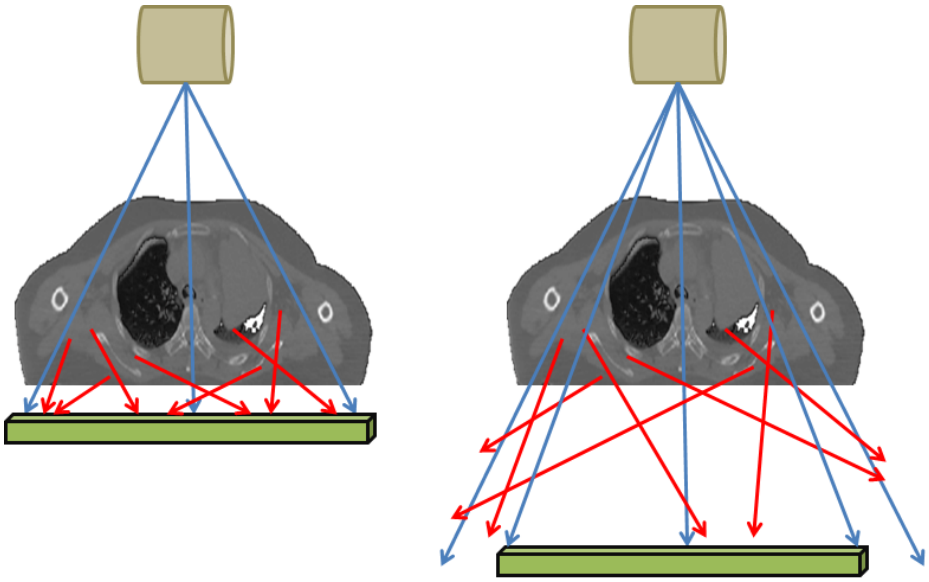

Figure 2.8: Increasing the air gap between the patient and the detector (~20 cm) reduces the number of scattered photons (red) that reach the detector. Primary photons (blue) maintain their path from the source to the detector, but the imaged field of view may be smaller due to the beam's divergence.

The amount of scattered radiation in a diagnostic image can be very high, with scatter fractions reaching over 90% of the total detector signal depending on field size and object thickness [25]. It is therefore beneficial to eliminate as much scatter as possible in order to maintain good image quality. Several scatter reduction techniques

exist, the most common being the anti-scatter grid [26]. Anti-scatter grids use a series of attenuating partitions which create small gaps that are oriented in the direction of the beam divergence. Primary photons have a high probability of transmission through the grid due to the orientation, while scattered photons travelling at oblique angles to the primary path are more likely to be attenuated.

Another method that can be used to reduce the scatter in an image is by increasing the distance between the imaged object and the detector. Scattered photons created within the object can be directed at any angle. Figure 2.8 shows that by increasing the air gap between the object and the detector, more scattered photons will leave the primary field before reaching the detector. Fewer scattered photons will be detected, while the primary photons will continue to travel in straight lines towards the detector. A 20 cm air gap has been shown to be as effective at reducing noise due to scatter as a highly selective grid [26]. However, increasing the distance between the patient and detector will result in increased magnification of the anatomy as well as a decrease in the imaged field of view due to the cone extending beyond the detector.

### 2.3.2 X-ray detection in radiography

The spectra that emerge from an imaged object vary in terms of photon fluence and energy distribution, depending on the locations that they pass through the objects. These differences must be detected and quantified in order to create a radiographic image. The standard method for 2D x-ray detection for most of the $20^{th}$ century has been screen-film radiography [22]. Film systems use an intensifying screen composed of a scintillator that produces visible light when exposed to ionizing radiation. The light exposes the photosensitive film adjacent to the screen, causing it to darken. The screen responds linearly to x-ray exposure, therefore a higher KERMA at a point results in more light and therefore a greater film response [22]. Film systems required films to be manually transported and developed, which can take an extended amount of time. The need for faster image viewing is the primary reason for the development of digital radiography which has the advantage of immediate image display [24].

Standard detectors in digital radiography utilize flat panel thin-film transistor arrays, which are generally composed of amorphous silicon (a-Si), a semiconductor. During an x-ray exposure, each element in the array accumulates and stores electrical charge in a capacitor. After the exposure is finished, the charge in each element is collected, amplified, converted to a voltage, and digitized [22]. The digitized voltage

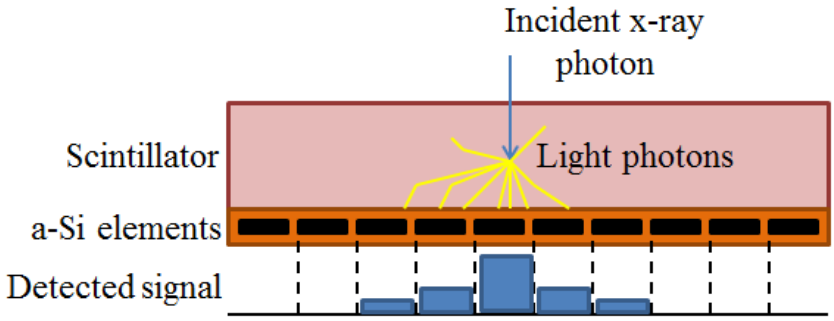


Figure 2.9: Schematic diagram of an indirect detection thin-film transistor array. A single x-ray photon interacts with the scintillator to produce light which is detected by the photosensitive a-Si elements.

is subsequently converted into a gray scale value which is used to display an image. The magnitude of the signal charge in the different pixels, and hence the gray scale value (or pixel value), is dependent on the exposure variations of the x-ray beam. One of the ways that x-ray detection and charge production can occur is through a method called *indirect detection*. In this method, the array utilizes a scintillator that converts the energy from the incident x-rays to light. The light is detected by the photosensitive a-Si photodiode that generates an electrical charge proportional to the intensity of the light incident on the element. The intensity of the light produced, and the subsequent charge, is related to the intensity of the x-ray beam incident on the surface of the detector at that point [24]. Due to the fact that x-ray interactions are more likely to occur near the entrance side of the scintillator, the light photons must travel a distance (several millimetres) before reaching the photosensitive elements. Ideally, only the detector element that is directly in line with the incident photon will receive any signal. However, Figure 2.9 shows how the light photons can scatter and potentially produce small signals in multiple detector elements, resulting in blurring in the image [22]. Most flat panel systems use CsI as the scintillator because it forms in columnar crystals that reduce the lateral spread of light and preserve spatial resolution [22].

### 2.3.3 Computed Tomography

Radiography reduces the 3D anatomy of a patient into a 2D projection image. While this can be useful for locating certain structures, a large amount of information can be lost in the dimension parallel to the x-ray beam. X-ray computed tomography, or

CT, is used to create 3D images in order to reveal, in high detail, all of the patient's anatomy. CT involves the use of an x-ray source and detector which rotate around the patient and takes a series of thin radiographic images. These images represent the attenuation properties of the patient at each angle and are combined to produce an image of a single slice through the patient [22]. Repeating this process over a series of slices and combining them will produce a full 3D volumetric data set.

The grey scale values in CT, called Hounsfield units (HU), are used to quantitatively describe each small volume element (voxel) of the image. The HU in each voxel at location $(x, y, z)$ in the image is defined as

$$HU(x, y, z) = 1000\frac{\mu(x, y, z) - \mu_w}{\mu_w}, \tag{2.12}$$

where $\mu(x, y, z)$ is the average linear attenuation coefficient of the material in the voxel and $\mu_w$ is the linear attenuation coefficient of water for the x-ray spectrum used to acquire the image [22]. In a voxel that contains only water, $\mu(x, y, z) = \mu_w$ and HU=0, while a voxel in air has negligible attenuation so HU = -1000. Dense bone generally has a HU $\approx$ 1000 which represents the approximate range of HU values seen in a patient CT. Due to the high contrast resulting from CTs being able to differentiate materials based on small differences in attenuation coefficients, computed tomography has become the most widely used imaging modality for radiation therapy treatment planning [9]. Therefore, nearly every patient that undergoes external beam radiation has an associated CT dataset that can be used in the production of digitally reconstructed radiographs.

## 2.4 Summary

The OBI detector responds linearly with the exposure, meaning that the gray scale value (or pixel value) of an image will change at the same rate as the exposure to the detector, as shown in Figure 2.10. Increasing the exposure beyond a certain level (set by the properties of the electronics in the detector) will not increase the pixel value displayed by the detector, thus saturating the image. Therefore, large differences in the exposure in the saturated region will not produce any contrast. The effects of detector saturation can be eliminated through the use of an automatic exposure control, which would integrate the exposure signal and terminate the exposure when a preset exposure limit is reached. For some digital imaging systems, the signal

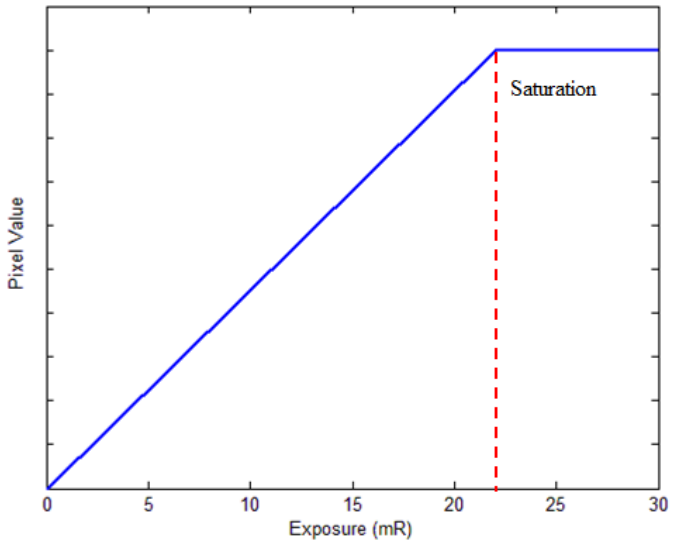


Figure 2.10: A characteristic curve for a digital detector shows the linear response to exposure and the subsequent saturation when an exposure limit is reached.

from the detector itself is used as the automatic exposure control (AEC) and would terminate the exposure when any point on the image reaches saturation [22].

As mentioned previously, the Varian OBI does not have an AEC, and therefore there is nothing in place to prevent detector saturation from occurring. The fundamental interactions and processes that are involved in the production of radiographic images have been discussed in this chapter. Chapter 3 describes how these imaging fundamentals are modelled and simulated to create virtual radiographs which can be used as a software based AEC that can predict detector saturation before images are acquired on the OBI.

# Chapter 3

# Materials & Methods

Development of a software based automatic exposure control requires the exposure setting (mAs) to be known before the patient is imaged. If the total level of detector saturation per unit mAs ($\%Sat/\text{mAs}$) is known, the mAs required to achieve a desired level of detector saturation ($\%Sat_F$) can be determined

$$mAs = \frac{\%Sat_F}{\frac{\%Sat}{mAs}}. \tag{3.1}$$

Prediction of the detector response involves the simulation of a radiographic image. Quantitative images that represent the saturation values that are produced by the OBI system can be created by determining the incident x-ray spectrum produced from the x-ray tube, calculating the attenuation of the spectrum through the imaged object, and modelling the response of the detector to the attenuated x-rays. Chapter 3 describes the methods used to produce virtual radiographic images to predict the detector response that is produced for any exposure situation.

## 3.1 OBI Characterization

The Varian on-board imager (Varian Medical Systems, Palo Alto, CA) is composed of an x-ray tube (Varian X-Ray Model G242, Varian Medical Systems, Inc., Salt Lake City, UT) and an a-Si flat panel detector (PaxScan® 4030CB, Varian Medical Systems, Inc., Salt Lake City, UT), shown on in Figure 1.2. The x-ray tube is a rotating tungsten anode device with a tube potential range of 40 to 150 kVp [27]. The source can be moved between 80 and 100 cm from the unit's isocenter, where the

standard source to axis (or isocenter) distance (SAD) is 100 cm [18]. The system's CsI indirect detector has a 397 × 298 mm active area containing a total of 2048 × 1536 individual pixel elements [18, 28]. The system uses a resolution of 0.390 mm per pixel for imaging [28]. There is no anti-scatter grid on the detector, and therefore air gaps must be utilized to reduce image scatter. The standard source to detector distance (SDD) used in IGRT is 150 cm, leaving anywhere from a 20 to 40 cm air gap depending on the patient positioning.

Characterization of the system was designed to predict the optimal exposure settings based on the x-ray tube output and the detector response. Treatment situations were simulated on a single Varian iX gantry mounted OBI. All measurements were set up with the standard SAD of 100 cm and SDD of 150 cm. Exposure and beam quality measurements were performed using a Radcal 10X5-6 diagnostic ionization chamber (Radcal Corporation, Monrovia, Ca), and a Unfors (Raysafe) Xi (Unfors Instruments AB, Billdal, Sweden) semiconductor diode detector.

### 3.1.1 OBI System Output

Several sets of measurements were performed in order to characterize the open beam that emerges from the system's x-ray tube. By placing the ionization chamber at the unit's isocenter and varying the mAs, a linear relationship between the exposure and mAs was derived. Output measurements were repeated for several clinically relevant tube voltages (kVp) in the range of 40 to 150 kVp. Small field sizes (5 × 5 $cm^2$) were used in order to reduce additional exposure due to scattered radiation, thus giving the results for only the primary mR/mAs of the open beams. Output values could vary slightly for each measurement, so the consistency needed to be monitored. Measurements at 80 and 100 kVp were performed weekly in order to observe any trends in the system's output.

The HVL, measured in mmAl, for each of the kVp used in modelling the system output was also measured to characterize the quality of the beams. The HVL of a beam can be determined by attenuating a narrow beam through incremental thicknesses of aluminium. An ionization chamber was positioned approximately 50 cm from the attenuators in order to prevent scattered radiation from being measured. The exposure was measured for each thickness of aluminium until the incident, unattenuated exposure had been reduced by more than half. By fitting an exponential curve to the values, the thickness of aluminium required to reduce the exposure by

half was determined.

The Unfors Xi diode can directly measure the HVL of a beam up to 14 mmAl [29]. Measurements were done with the diode and compared to the values that were calculated with the ionization chamber in order to verify the consistency of the two methods. In addition to measuring the HVLs of open beams, the two methods were compared on beams that had been hardened by 5 and 10 cm of polystyrene and Solid Water (RMI Gammex, Middleton, WI). With the confirmation of the accuracy of the device, the Unfors diode was used for all subsequent HVL measurements.

### 3.1.2 OBI Detector Response

Predicting the level of imager saturation requires that its response to different levels and qualities of exposure are known. By measuring how the detector responds to a range of exposures, a model can be built to determine the exposures required to saturate the detector. In order to determine the sensitivity, range, and energy dependence of the detector, characteristic curves for several different open beams in the diagnostic spectrum were generated. The response was measured by adjusting the mAs of a narrow beam ($5 \times 5$ cm$^2$) and recording the exposure in mR as well as the image pixel value produced by the OBI's detector in a region of interest (ROI). The measured exposures were used to calculate the exposure at the detector surface using the inverse square law (Equation 2.10).

The OBI produces a range of pixel values from 65535 for an unexposed image, to 40691 in a saturated image. For each exposure, the pixel values were recorded in a 50 $\times$ 50 pixel ROI in the center of the image and converted to a percentage of detector saturation ($\%Sat$) by

$$\%Sat = \frac{Dark - PV}{Dark - Sat} \times 100, \tag{3.2}$$

where $Dark$ and $Sat$ represent the unexposed and saturated pixel values, respectively. Using these values, the percentage of detector saturation was plotted as a function of the exposure at the detector surface, resulting in a characteristic curve for the OBI system for different energies.

The characteristic curves for the detector showed a distinct energy dependence which decreased with increasing kVp of the open beams. The response of the detector was therefore modelled as a function of the beam quality (HVL) of the beam reaching the detector so that the response could be predicted regardless of added filtration. The slope of the characteristic curves ($\%Sat$/mR) were plotted as a function of the HVL,

Table 3.1: Various beams attenuated by Solid Water (SW) and polystyrene (poly) and their corresponding HVLs.

| kVp / Filtration | HVL (mmAl) | kVp / Filtration | HVL (mmAl) |
|---|---|---|---|
| 40 / Open | 1.48 ± 0.01 | 65 / Open | 2.52 ± 0.02 |
| 80 / Open | 3.04 ± 0.01 | 100 / Open | 3.93 ± 0.02 |
| 110 / Open | 4.35 ± 0.02 | 120 / Open | 4.77 ± 0.01 |
| 135 / Open | 5.31 ± 0.02 | 150 / Open | 5.84 ± 0.01 |
| 100 / 5 cm poly | 4.98 ± 0.01 | 125 / 5 cm poly | 6.10 ± 0.02 |
| 100 / 10 cm poly | 5.82 ± 0.02 | 85 / 15 cm poly | 5.56 ± 0.01 |
| 100 / 15 cm poly | 6.53 ± 0.02 | 120 / 15 cm poly | 7.67 ± 0.02 |
| 105 / 20 cm poly | 7.45 ± 0.01 | 125 / 20 cm poly | 8.49 ± 0.02 |
| 100 / 5 cm SW | 6.02 ± 0.01 | 115 / 5 cm SW | 6.79 ± 0.01 |
| 110 / 10 cm SW | 7.96 ± 0.01 | 135 / 10 cm SW | 9.14 ± 0.01 |
| 100 / 10 cm SW | 7.37 ± 0.01 | 105 / 15 cm SW | 8.66 ± 0.01 |
| 120 / 15 cm SW | 9.45 ± 0.02 | 135 / 15 cm SW | 10.18 ± 0.02 |
| 110 / 15 cm SW, 5 cm poly | 9.28 ± 0.02 | 135 / 15 cm SW, 5 cm poly | 10.53 ± 0.02 |

which were measured as described in Section 3.1.1. In order to test that the model would represent all beam qualities, the detector responses were measured for a variety of hardened beams with different combinations of tube potentials and attenuating materials placed between the source and detector, shown in Table 3.1. A logarithmic function was fit to the measured data that could subsequently be used to calculate the $\%Sat/\text{mR}$ given the HVL.

As discussed in Section 2.3.1, scattered radiation could result in a large signal during measurements with added material, but the detector model was based only on primary radiation. Since the scatter fraction is dependent on the material thickness and kVp, the exposure that would produce the most amount of scatter from Table 3.1 (15 cm Solid Water, 5 cm polystyrene, 135 kVp) was tested to determine the air gap required to eliminate the scatter. If scattered radiation was not detected for this exposure then that would also be true for all of the other exposures due to their smaller scatter fractions. A 5 × 5 $\text{cm}^2$ field size was used to expose the ionization chamber, positioned at isocenter, with the material placed directly beside the chamber. The material was incrementally moved further from the ionization chamber in order to increase the air gap, thus reducing the exposure by eliminating some scattered x-rays. Additionally, due to the divergence of the beam, moving the material closer to the source resulted in a decreased field size on the exit side of the

material and therefore further reduced scatter. Theoretically, with a large enough air gap, scattered radiation is effectively removed from the point of measurement, so further increases in the air gap would not result in a further decrease in the exposure [25]. The scatter was found to be negligible when the material was placed directly against the source housing (22.2 cm from source). This positioning was used for all of the measurements to ensure that only the primary signal was being detected for the response measurements.

### 3.1.3 Scatter Characterization

In order to determine the total level of detector saturation in an image, scattered radiation must be considered in addition to the primary exposure. As discussed in Section 2.3.1, scattered photons can result in a significant amount of signal to the detector that contributes to the level of saturation while providing no information content to the resulting image. Therefore, the response model must contain a scatter component in order to determine the actual exposure to the detector. Referring to Equation 3.1, it can be seen that the detector saturation level per mAs is required. The scatter fraction given in Equation 2.11 can represent the scatter fraction per unit mAs:

$$SF = \frac{\frac{\%Sat}{mAs}(S)}{\frac{\%Sat}{mAs}(T)} = \frac{\frac{\%Sat}{mAs}(S)}{\frac{\%Sat}{mAs}(S) + \frac{\%Sat}{mAs}(P)}, \tag{3.3}$$

since the total level of detector saturation per mAs, $\frac{\%Sat}{mAs}(T)$, is equivalent to the sum of the scatter $\left(\frac{\%Sat}{mAs}(S)\right)$ and primary $\left(\frac{\%Sat}{mAs}(P)\right)$ components of the signal.

The level of detector saturation from scattered radiation needed to be determined for different exposure situations in order to accurately model the scatter fraction in on-board imaging. Stacks of Solid Water ranging from 5 to 20 cm (5 cm increments) were centred at the system's isocenter, as shown in Figure 3.1. With an SAD of 100 cm and an SDD of 150 cm, this positioning resulted in air gaps ranging from 47.5 to 40 cm. Images were taken with tube potentials of 80, 100, 110, 120, 135 kVp and square field sizes of 4 × 4, 7 × 7, 10 × 10, 15 × 15, 20 × 20, 25 × 25, and 30 × 30 $cm^2$ (at isocenter). The resulting saturation percent in an ROI in the center of the image was recorded using multiple different mAs. The slopes of the linearly related data give the $\frac{\%Sat}{mAs}(T)$ since the signal contained both the primary and scattered components.

In order to determine the amount of scatter in each exposure, the primary signal was measured and subtracted from the total detector response. The primary signal

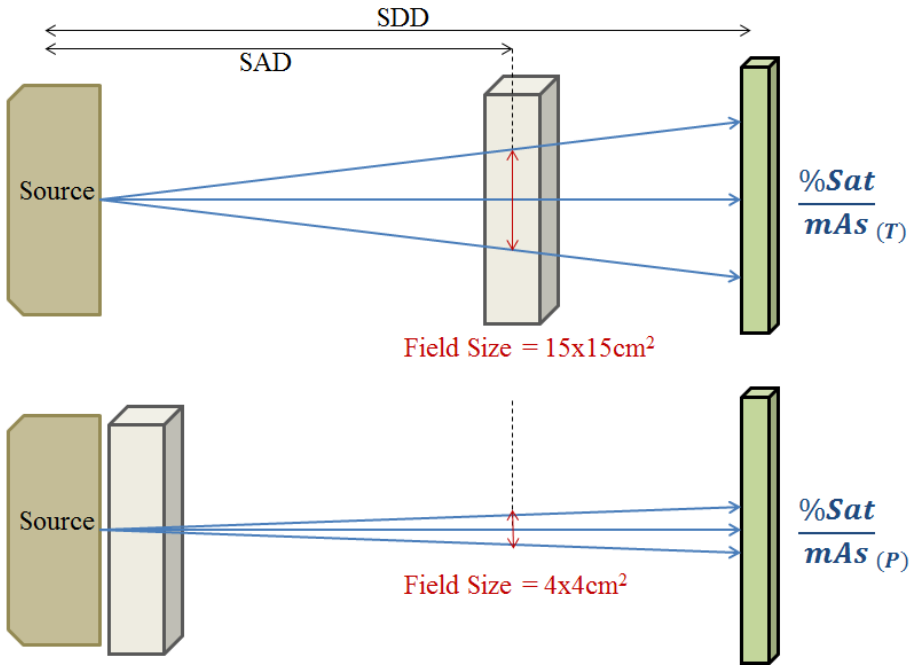


Figure 3.1: Moving an imaged object further from the detector and reducing the field size effectively removes the scattered component from the signal.

was determined by repeating the same set of measurements while utilizing a small ($4 \times 4$ cm$^2$) field size with the material placed against the source housing (Figure 3.1). The small field size and large air gap ensured that no scattered radiation was being detected by the OBI, therefore resulting in the detector response due to primary radiation only. By taking the difference between the total and primary signals, the scatter component, and thus the scatter fraction, could be determined for each exposure situation.

### 3.1.4 System Model

The goal of modelling the system, as shown by Equation 3.1, was to find the detector response per unit mAs in order to determine the mAs required to produce a given level of detector saturation. The response equation must be separated into primary and scatter components as both respond differently in certain exposure situations. The total detector response is a combination of the primary and scatter signals, so the two components could be split as was done in Equation 3.3. From the data that was measured for the model, $\frac{\%Sat}{mAs}_{(P)}$ can be expanded to the product of the primary exposure per mAs that reaches the detector and the detector response per mR as a

function of the beam quality:

$$\frac{\%Sat}{mAs} = \frac{mR}{mAs_{\,(P)}} \times \frac{\%Sat}{mR}\,(HVL)_{(P)} + \frac{\%Sat}{mAs_{\,(S)}}. \tag{3.4}$$

As discussed in Section 3.1.3, the scatter fraction can be defined by Equation 3.3. Using the measured scatter fractions, the detector response per mAs due to scattered radiation can be substituted into the model in terms of the primary response. Rearranging Equation 3.3 and expanding the primary $\%Sat$/mAs gives

$$\frac{\%Sat}{mAs_{\,(S)}} = \frac{SF \times \frac{mR}{mAs}_{(P)} \frac{\%Sat}{mR}_{(P)}}{1 - SF}. \tag{3.5}$$

Substituting the scatter component into Equation 3.4 and simplifying gives the final equation for the model:

$$\frac{\%Sat}{mAs} = \frac{mR}{mAs_{\,(P)}} \times \frac{\%Sat}{mR}\,(HVL)_{(P)} \times (1 - SF)^{-1}. \tag{3.6}$$

Therefore, for a given exposure, if the $\frac{mR}{mAs}$ and the HVL of the primary beam reaching the detector are known then the primary detector response can be determined using the detector response model. Combining these values with the scatter fraction for the exposure will result in the total level of detector saturation per mAs for any known exposure situation.

## 3.2 Digitally Reconstructed Radiograph Production

Application of the system model requires that the exposure at each point on the detector to be known after the x-rays pass through the imaging object. A calculation of these values can be performed by constructing a digitally reconstructed radiograph (DRR). A DRR is a virtual representation of a radiographic procedure. Many different algorithms exist to calculate spatially accurate DRRs in optimized times [30–32]. These programs are generally used to produce *qualitative* images where the values do not physically represent the actual exposure or pixel value on a detector [31]. A DRR calculation method was developed in order to determine the energy spectrum that emerges from an imaged object. Calculation of the spectrum allows the exposure, as

well as the beam quality to be calculated which may be used in conjunction with the system model to determine the actual level of detector saturation in an exposure.

### 3.2.1 X-ray Spectrum Production

DRR generation began with the production of the spectrum that would emerge from the x-ray tube. Direct measurement of an x-ray spectrum is a complex task that generally requires expensive equipment and extensive amounts of time [33]. Instead of measuring the spectrum produced by the tube for different kVp, the x-ray spectra were generated using SpekCalc (Institute of Cancer Research, London), a software program designed to calculate the x-ray spectra that emerge from a tungsten anode x-ray tube [34]. SpekCalc uses pre-calculated electron distributions within the anode which were determined using Monte Carlo methods [35]. The electron distributions include the survival probabilities of electrons reaching different depths in the anode, as well as the energy distribution at those depths. A deterministic model then uses the electron distributions to calculate the bremsstrahlung and characteristic x-rays that emerge from the anode [36]. Spekcalc outputs the complete x-ray spectrum and can be adjusted based on the anode angle and filtration within the x-ray tube. The spectrum is divided into discrete energy bins where the bin height is in units of photons per keV $cm^2$ mAs at a distance of 100 cm from the source. In addition, the program also outputs values such as the HVL and the mean energy.

SpekCalc has been shown to produce spectra with good agreement to spectra that were produced using BEAMnrc Monte Carlo, which has been demonstrated to accurately predict spectra from experimental measurements [37]. The maximum discrepancy in the HVL between the two methods for various tube potentials, filtrations, and anode angles was found to be up to 5% [34]. SpekCalc has also been compared to measured data, resulting in agreements of the HVLs within 5%, with the main limitations being attributed to determining the actual total filtration within an x-ray unit [33]. The software was tested to ensure that the spectra used in the DRR calculations accurately represented the spectra that emerge from the x-ray tube.

The SpekCalc software was used to calculate the spectrum of an open 100 kVp beam using a 14 degree anode angle, which is the anode angle on the OBI x-ray tube [27]. Since the total filtration of the tube was not known, the values were adjusted to match the HVL produced by SpekCalc to the one that was measured on the unit. The parameters in the program were then tested by comparing the calculated HVLs

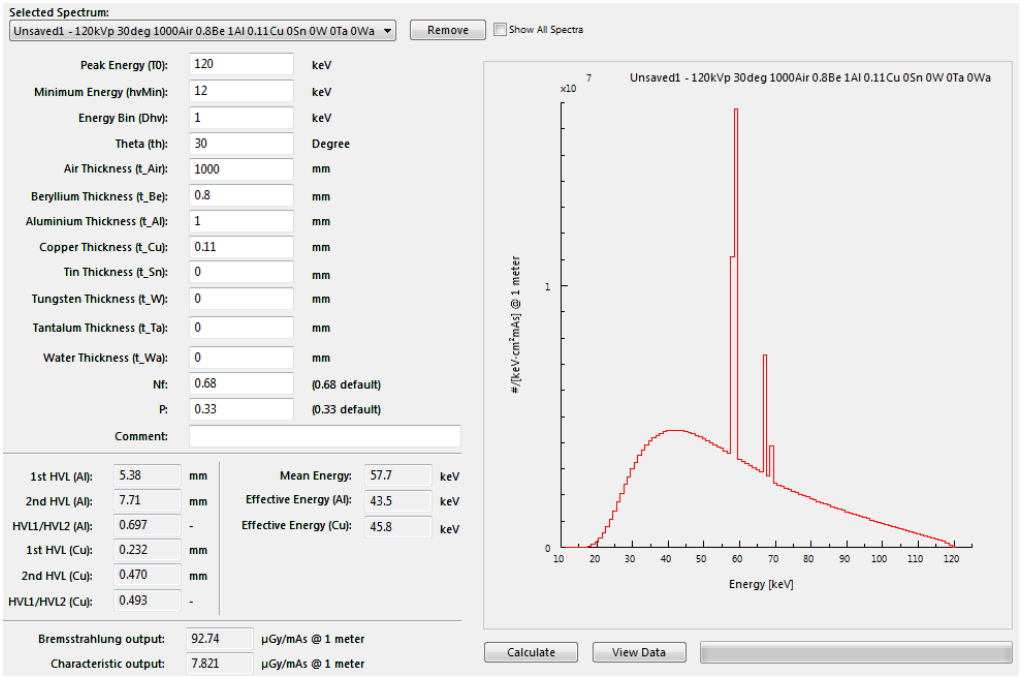


Figure 3.2: The graphical user interface of the SpekCalc software.

for various tube potentials (40 to 150 kVp) to the measured value. To further test the spectra, HVLs were measured for 65, 80, 100, and 120 kVp beams filtered by combinations of water and aluminium, and compared to the values calculated by SpekCalc. A good agreement was found between the values produced by SpekCalc and the values that were measured on the OBI, so the spectra produced by the software would subsequently be used for DRR calculations.

### 3.2.2 Volumetric Datasets

Calculation of a DRR uses a volumetric data set which simulates the imaged object. The attenuation properties of the imaged object are determined by its CT dataset. All datasets for the research were acquired using a GE LightSpeed RT[16] CT scanner (GE Medical Systems, Waukesha, Wi). As discussed in Section 2.3.3, the values of a CT dataset are given in HU. In order to determine the intensity of x-rays that emerge from an imaged object, the HU must be used to determine the attenuation properties of the material. Given the similarities in energy between the x-rays used to acquire CT images and those used to take radiographic images (30 to 120 keV), the HU in an object can be related to the attenuation coefficients associated with the attenuation of a radiographic x-ray beam travelling through the object [9, 30, 32].

The HU in an image can be converted to the linear attenuation coefficient by constructing a conversion curve of the linear attenuation coefficient as a function of the HU for several known materials [30]. The conversion curve was constructed by scanning the CIRS 062M Electron Density Phantom (CIRS Inc., Norfolk, Va) and the Catphan 504 CT Phantom (The Phantom Laboratory Inc., Greenwich, NY) [38, 39]. The phantoms each contain several cylindrical inserts (9 in the CIRS phantom and 6 in the Catphan) composed of known materials that represent the range of HU that is seen during a patient CT scan (-800 to 900 HU). The linear attenuation coefficients of each of the inserts in the Catphan were given in the user manual [39]. The linear attenuation coefficients of each of the inserts in the CIRS phantom were determined using NIST's XCOM Photon Cross Section Database[1], which calculates the attenuation coefficients for materials based on their atomic compositions (provided by CIRS Inc.) [40]. Since the linear attenuation coefficients are energy dependent (Section 2.1.2), the values had to be calculated for each energy in the diagnostic spectrum (in 2 keV intervals). A conversion curve was generated for each energy by plotting the linear attenuation coefficients of the different inserts as a function of their HU. Therefore, given any HU, the linear attenuation coefficient of any photon energy in the spectrum could be determined by interpolating the values on the appropriate curve.

The CIRS phantom was also used to convert the HU to the relative electron density of the material. Since the scatter fraction was measured in terms of the thickness of Solid Water, different types of material were required to be converted to an *equivalent thickness*. Scattered photons are the result of Compton interactions, and the probability of a Compton interaction is dependent on the electron density of a material (Section 2.1.2). Therefore, a thickness of any material was converted to a water equivalent thickness using the electron densities. The conversion was done by plotting the HU of the inserts in the CIRS phantom against their electron densities (relative to water). By multiplying the thickness of a material by its relative electron density, the water equivalent thickness could be determined. For example, 5 cm of a material with a relative electron density of 1.2 would be equivalent in scattering to 6 cm of water.

[1] http://physics.nist.gov/xcom

### 3.2.3 Ray Trace Algorithm

The DRR calculation algorithm begins by taking a spectrum produced by SpekCalc and a CT dataset as inputs. The output that was measured on the unit for the desired kVp is used to scale the spectrum. Scaling is done by integrating the spectrum using Equation 2.8. Integrating the spectrum given by SpekCalc results in a KERMA with units given in keV $g^{-1}$ $mAs^{-1}$. The KERMA ($K$) is converted to $\mu$Gy/mAs ($\mu$J $kg^{-1}$ $mAs^{-1}$) and the fluence of each energy bin ($\Phi(E)_o$) is normalized and multiplied by the physical output

$$\Phi(E)_F = Output \times \frac{\Phi(E)_o}{K}, \tag{3.7}$$

where $\Phi(E)_F$ is the new bin height and $Output$ is the measured output (converted from mR/mAs to $\mu$Gy/mAs using Equation 2.9).

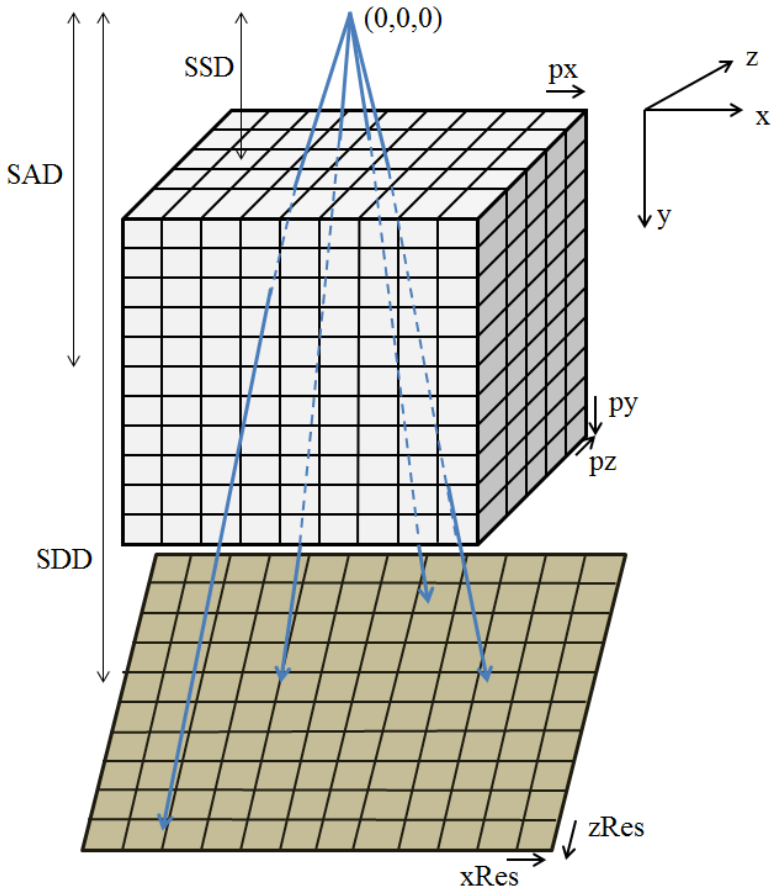


Figure 3.3: Geometry of the DRR calculation. Each ray passes through the voxalized CT data from the isotropic source to various points on the detector.

Each slice of the CT dataset is combined into a single 3D voxel array (Figure 3.3). The size of the voxels are dependent on the scan parameters. The pixels on the plane of each slice define the $x$ and $y$ dimensions of the voxel (defined as $px$ and $py$), and the slice thickness defines the $z$ dimension ($pz$). A coordinate system was defined with the source (with no rotation) at the origin (0,0,0). The source to surface distance (SSD) is the distance from the origin to the top of the CT volume along the y-axis. The volume is scanned with the center at isocenter, so the SSD can be calculated by subtracting half of the volume height from the SAD. The volume may be scanned with slight isocenter shifts so the volume can be shifted accordingly.

A virtual detector is also defined in the computer algorithm. Each pixel on the detector corresponds to the point in space ($x$,$SDD$,$z$) as the detector is perpendicular to the y-axis when there is no gantry rotation. The detector width and height (in number of pixels) can be adjusted depending on the desired resolution. The x-resolution is equal to 397 mm divided by the detector width, and the z-resolution is equal to 298 mm divided by the detector height (based on the real detector's width and height). With no gantry rotation, the position of each detector pixel ($Det_x, Det_z$) is equal to the $x$ and $z$ distance from the central pixel, equivalent to the number of pixels from the center times the detector resolution. If the gantry is rotated by an angle $\theta$ clockwise around the isocenter, the coordinates of the source ($x_s, y_s$) and detector pixels ($x_d, y_d$) are defined by:

$$\begin{bmatrix} x_s \\ y_s \end{bmatrix} = \begin{bmatrix} \cos\theta & -\sin\theta \\ \sin\theta & \cos\theta \end{bmatrix} \begin{bmatrix} 0 \\ -SAD \end{bmatrix} + \begin{bmatrix} 0 \\ SAD \end{bmatrix}, \tag{3.8}$$

and

$$\begin{bmatrix} x_d \\ y_d \end{bmatrix} = \begin{bmatrix} \cos\theta & -\sin\theta \\ \sin\theta & \cos\theta \end{bmatrix} \begin{bmatrix} Det_x \\ SDD - SAD \end{bmatrix} + \begin{bmatrix} 0 \\ SAD \end{bmatrix}. \tag{3.9}$$

Since $\theta$ is a rotation in the $xy$ plane, the $z$ position of the source ($z_s = 0$) and the detector ($z_d = Det_z$) are maintained. Using the source and detector positions, a vector can be created that represents the ray from the source to a detector pixel. A unique ray is created for each pixel on the detector array. As discussed in Section 2.3, each pixel on the detector is exposed to a different spectrum that emerges from the imaged volume. Therefore, by tracing and attenuating the incident spectrum through the volume for each ray, a DRR is produced.

The attenuation of the volume is determined using the data gathered in Section

3.2.2. Each voxel in the volume is converted from HU to the linear attenuation coefficient by interpolating the values of the conversion curves. As mentioned previously, the conversion from a CT number to a linear attenuation coefficient is unique for each energy. Since the entire energy spectrum is used in image production, the CT volume is converted to attenuation coefficients for each energy bin used in the DRR calculation. This method essentially results in a number of individual images (equal to the number of energy bins in the spectrum) being produced. Each image, which corresponds to a particular energy, will have pixel values representing the fluence of photons at that energy, emerging from the imaged object and reaching the detector.

To produce an image, each ray is traced though the volume to determine the net attenuation at a specific energy. The direction of the ray ($V$) travelling from the source position $(x_s, y_s, z_s)$ that exposes a single pixel located at $(x_d, y_d, z_d)$ is calculated by:

$$\begin{bmatrix} V_x \\ V_y \\ V_z \end{bmatrix} = \begin{bmatrix} x_d \\ y_d \\ z_d \end{bmatrix} - \begin{bmatrix} x_s \\ y_s \\ z_s \end{bmatrix}. \tag{3.10}$$

The ray is normalized and then extended from the source to the point where it first interacts with the volume. The linear attenuation coefficient of the voxel at the start location is recorded and the ray then proceeds to step through the volume. At the end of each step, the attenuation coefficient of the voxel that the ray is located in is added to the total attenuation coefficient of the ray. Constant step sizes, which are smaller than the dimensions of the voxel (less than 0.5 mm), are used in the ray trace. Figure 3.4 shows a ray trace with a larger step size that misses voxels 2 and 3, and is recorded in voxel 4. Therefore, the attenuation between the first and second step is calculated to be the attenuation coefficient of voxel 4 times the step size, and so information about everything in between is lost. A smaller step size will produce more accurate results by ensuring that no small details are missed, with the only trade-off being increased computation time [32].

The ray continually steps through the volume and sums the attenuation coefficients until it exits the CT volume, which may occur at any point on the volume's surface depending on positioning and divergence, as shown in Figure 3.3. The value that exits the volume is projected to the detector (minimal attenuation is assumed in air) and the final fluence ($\Phi(E)_F$) for the energy at the detector pixel is calculated

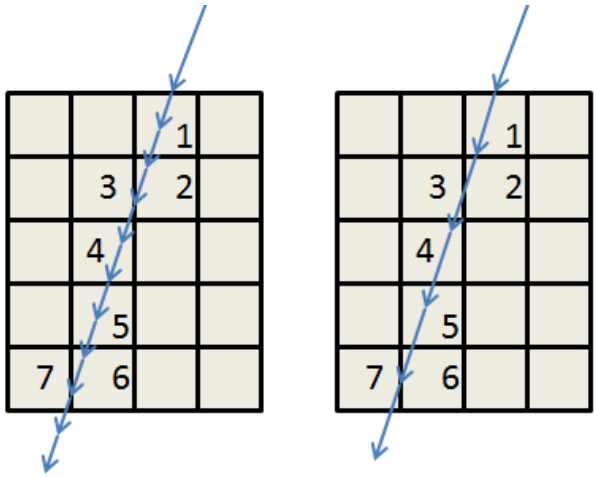


Figure 3.4: A ray steps through the volume and is attenuated by each voxel. Large step sizes (right) may result in the attenuation from certain voxels (2,3,6) to be missed.

by:

$$\Phi(E)_F = \Phi(E)_o \, e^{-S \sum_{i=1}^{n} \mu_i}, \tag{3.11}$$

for $n$ steps of size $S$ (cm). The ray tracing process is repeated for every pixel on the detector, and then for every energy in the spectrum. When images have been produced for each energy, the fluence values can be combined, resulting in each pixel on the detector containing the new energy spectrum that emerges from the imaged volume.

In addition to the attenuation along each ray for each energy being recorded, the water equivalent thickness that each ray travels through is also recorded. The total thickness is determined in a similar process to the summing of the attenuation for one energy, but instead of converting the HU to linear attenuation coefficients they are converted to relative electron density by the process described in Section 3.2.2. Each step size is therefore converted to an equivalent step size in water and summed to get the total water equivalent thickness of the object for each ray. Scatter fractions were measured in terms of the thickness of Solid Water, and therefore the calculated water equivalent thicknesses are converted to the Solid Water equivalent thicknesses so that the data acquired in Section 3.1.3 can be used to determine the scatter fractions. The Gammex Solid Water has an electron density of 1.012 relative to water. Dividing the water equivalent thickness by the relative electron density of Solid Water results in the material's equivalent thickness of Solid Water. The distance calculation only needs to be completed once for each ray since the electron density is a physical property

dependent on the material, not on the interacting photons.

### 3.2.4 DRR Calculation

The calculated spectra on the final image are used with the measured model to determine the physical values of the DRR. The spectra at each pixel are converted to the exposure using Equations 2.8 and 2.9. Since the initial spectrum was scaled to the output at the unit's isocenter, the values are corrected using the inverse square law (Equation 2.10) to give the mR/mAs at the surface of the detector.

In order to use the system model to determine the detector response, the HVL of the final spectra are also required. The HVL is calculated for a spectrum of energies by simulating the HVL measurements described in Section 3.1.1. The attenuation of each energy in the spectrum is calculated for a thickness of aluminium. After attenuating, the exposure for the new spectrum is calculated. The thickness of aluminium is increased in 0.05 mm increments and the calculation is repeated until the exposure is less than half of the initial exposure. By interpolating the thicknesses of the increments immediately before and after the incident exposure has be reduced by half, the HVL can be determined. The HVL of the spectrum at each pixel is determined using this process, resulting in a map of HVLs for the image.

With the mR/mAs and the HVL of each point on the image, Equation 3.6 can be used to determine the level of detector saturation per mAs. The $\%Sat$/mR is determined at each pixel by using the response model created in Section 3.1.2. Multiplying the $\%Sat$/mR of each pixel by the exposure (mR/mAs) at each pixel results in the $\%Sat$/mAs of the primary radiation that reaches the detector.

The effects of scattered radiation must also be included in the model to determine the total response of the detector in an imaging situation. Using the imaged field size, tube potential, and the water equivalent thickness that was determined from the ray trace, the scatter fraction is determined using the data measured in Section 3.1.3. Changes in the equivalent thickness can result in relatively steep gradients in the scatter, which is generally not seen in a diagnostic image [30]. The scatter values across the image were therefore simply blurred using a mean filter. The scatter fractions were also weighted radially based on the distance from the center of the image due to the fact that no scattered radiation will come from outside of the field of view.

Scatter calculations results in a value for the scatter fraction at each pixel in the

image. Using these values in Equation 3.6 along with the primary values produces the total level of detector saturation per mAs at every point in the image. The values in the entire image can simply be multiplied by a predetermined mAs in order to compare the results to measured data. A desired maximum $\%Sat$ can also be defined and divided by the $\%Sat$/mAs (Equation 3.1) in the region of greatest response in the image in order to determine the maximum mAs that can be used in image without saturating any point.

## 3.3 Experimental Validation

Combining the experimental model with the calculated DRRs allowed for the prediction of the detector response for an image taken of any object that has an associated volumetric dataset CT. Validation of the process was done through comparisons between calculated and measured images in order to ensure that the values calculated by the software accurately predicted the level of saturation produced on the OBI.

### 3.3.1 Phantom Tests

Initial validation was done by testing the accuracy of the software in predicting the exposure and HVL after the beam had been attenuated by various thicknesses of material (phantoms). Three phantoms were composed of 10 cm of Solid Water, 2 cm of polystyrene between 10 cm of Solid Water, and 5 cm of polystyrene and 3 cm of PMMA between 10 cm of Solid Water. Data was measured using small field sizes and large air gaps to ensure only the comparison of primary radiation. Combinations of the different materials and kVp were used to test a wide range of data. Each of the phantoms were imaged with the CT scanner and the exposures and HVL were calculated and compared to the measured data. The $\%Sat$/mAs that was produced from the primary exposures were also recorded, as well as the responses from the same phantoms placed at isocenter with large field sizes. Since the phantoms were just stacks of material, no contrast was produced in the image, but the central pixel values were compared in order to test the program's ability to predict the primary and total (by testing the scatter fraction calculations) response for simple phantoms.

Calculation of the scatter fraction based on the water equivalent thickness was also tested. The scatter fraction for phantoms with various of thicknesses and densities were measured using the same process described in Section 3.1.3. These phantoms

Table 3.2: Compositions of three phantoms used to test the system scatter model.

| Phantom1 | Phantom2 | Phantom3 |
|---|---|---|
| Solid Water - 2 cm | Solid Water - 2 cm | Solid Water - 2 cm |
| Plywood - 1.5 cm | Urethane foam - 4cm | MDF - 2 cm |
| Polystyrene - 2 cm | PMMA - 3 cm | Plywood - 1.5 cm |
| PMMA - 3 cm | MDF - 2 cm | Solid Water - 2 cm |
| MDF - 2 cm | Urethan foam - 4 cm | |
| Plywood - 1.5 cm | Solid Water - 2 cm | |
| Solid Water - 3 cm | | |


Figure 3.5: The Alderson Radiation Therapy anthropomorphic phantom.

were composed of the stacks of material shown in Table 3.2, and the scatter fractions were measured for 80, 100, and 120 kVp with field sizes of 10 $\times$ 10 cm$^2$, 15 $\times$ 15 cm$^2$, and 25 $\times$ 25 cm$^2$. After measurements, the phantoms were scanned and the volumetric data sets were used to calculate the water equivalent thickness based on the electron densities. The scatter fractions on the central axis were calculated for these thicknesses for the different kVP and field sizes and compared to the measured results.

With the successful calculations of simple block phantoms, the program was tested to evaluate its ability to calculate attenuations from a wider range of materials and to observe the contrast and spatial resolution created from imaging more complex phantoms. The Alderson Radiation Therapy (ART) anthropomorphic phantom (Alderson

Research Laboratories, Inc., Long Island City, NY) was used to simulate chest and abdominal radiographs. Exposures of the ART phantom were taken at different orientations (anterior-posterior, lateral), field sizes, and kVP while varying the mAs. The resulting images were converted to $\%Sat$ values and normalized by their corresponding mAs to produce images with pixel values of $\%Sat$/mAs, which could be compared to the calculated values. Comparisons were done by plotting profiles (arrays of values in a straight line across the image) of the two images and observing the absolute difference in the exposure values at any point on the image as well as differences in exposure gradients and spatial resolution.

### 3.3.2 Clinical Data Tests

Verification of the calculated results for the various phantoms described in the previous section ensured that the DRR calculation program was functioning as expected. To test if the program would be able to accurately predict patient specific exposure factors, calculations were performed on clinical datasets and compared to the images that had been acquired during patient treatment.

The anonymized CT datasets of two previously treated patients were acquired, along with the chest radiographs that were taken during the course of their IGRT treatments. Patients receiving lung treatments were chosen because images of the chest are the most likely to become saturated due to the low attenuation of the lung tissues. The OBI images of one patient were not saturated and were used to determine the accuracy of the calculation in the different tissues that are present in a chest radiograph. The images of the other patient were entirely saturated in the lung region. The saturated image was used to test the software's ability to calculate the mAs that would be required to produce an image with no saturation.

# Chapter 4

# System Model Results

The OBI system was modelled in terms of the x-ray tube output and the detector response. The measurements that were outlined in Chapter 3 were designed to determine the exposure rates and beam qualities produced by the x-ray tube, the response of the detector to various exposures, and the scatter produced in clinically relevant imaging situations. Several tests were also performed to ensure the accuracy and consistency of the measured data that was used in the model. The following chapter presents the results of the data that was used to construct the OBI model.

## 4.1 X-ray tube output

The x-ray tube output for the OBI as a function of the mAs for various kVp is shown in Figure 4.1. As expected, the exposure is seen to increase linearly with mAs due to the directly proportional relationship between mAs, interacting electrons in the x-ray tube, and the subsequent x-rays that are produced. The slopes of each of the lines in Figure 4.1 represent the x-ray tube's output in mR/mAs at the system's isocenter. The outputs for 40, 65, 80, 100, and 120 kVp are listed in Table 4.1. The uncertainties on the outputs are given as the standard error in the measured values.

Due to the observation of slight fluctuations in the output of the system, measurements at 80 and 100 kVp were performed over a 14 week period to observe any trends in the output. Figure 4.2 shows the mR/mAs of the system measured at different points in time. The outputs appear to fluctuate around the mean values of 7.98 and 11.95 mR/mAs with standard deviations of 0.12 and 0.19 mR/mAs for 80 and 100 kVp, respectively. No long term trends in the output were observed. Measurements

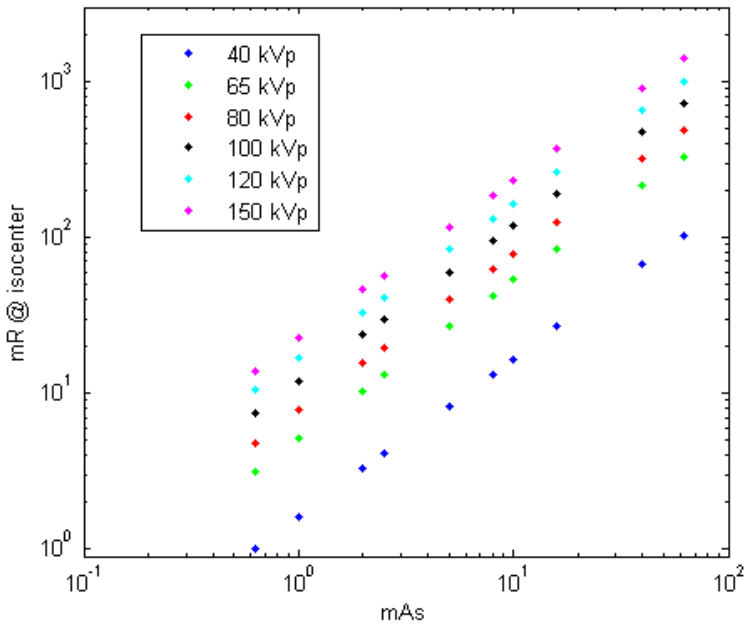


Figure 4.1: System output (mR) measured at the unit's isocenter as a function of the mAs.

Table 4.1: X-ray tube outputs measured at the system's isocenter for the full range of kVp available on the OBI

| kVp | mR/mAs |
|---|---|
| 40 | 1.66 ± 0.03 |
| 65 | 5.28 ± 0.04 |
| 80 | 7.93 ± 0.04 |
| 100 | 11.88 ± 0.03 |
| 120 | 16.19 ± 0.05 |
| 150 | 22.89 ± 0.08 |

were performed when the x-ray tube was cold (immediately after start-up), after prolonged use of the x-ray tube, and after the system had been used clinically. Outputs measured at different times on the same day were seen to vary similarly to weekly variations, and no correlations between the output and the time of measurement were observed.

In addition to the exposure produced by the x-ray tube, the beam qualities of the fields were required to characterize the system. The half-value layers of the beams used for the system model were measured using the Unfors Xi diode which has a given uncertainty of ±10% [29]. In order to ensure the accuracy of the diode, HVLs that

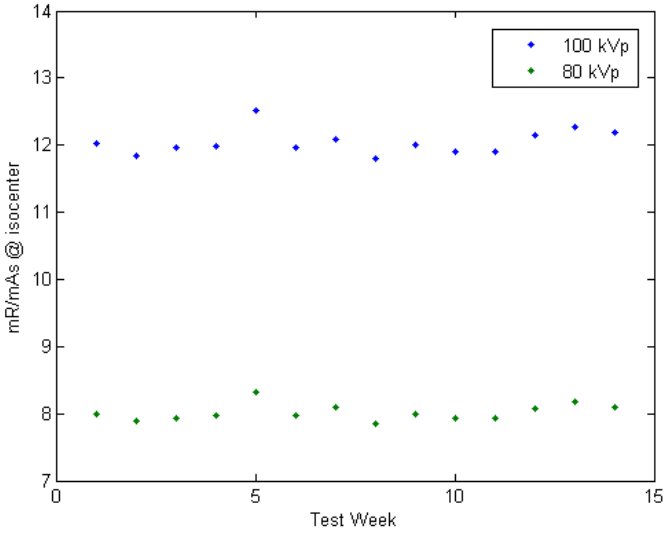


Figure 4.2: System output (mR/mAs) measured at the unit's isocenter for 80 and 100 kVp measured over 14 weeks.

were measured with the diode were compared to the HVLs measured using the manual method described in Section 3.1.1. Table 4.2 shows the HVLs determined using the two different methods for a variety of beam qualities. All of the measurements were well within the specified uncertainty of the diode, with the worst difference being measured for the 65 kVp open field.

Table 4.2: Comparison of the HVLs measured by manually attenuating beams (IC) and measurements made with the Unfors Xi diode (Xi).

| kVp / Filtration | IC (mmAl) | Xi (mmAl) | Difference (%) |
|---|---|---|---|
| 65 kVp / Open | 2.63 | 2.53 | -3.80 |
| 100 kVp / Open | 3.96 | 3.94 | -0.51 |
| 120 kVp / Open | 4.80 | 4.77 | -0.63 |
| 65 kVp / 5 cm polystyrene | 3.15 | 3.13 | -0.63 |
| 100 kVp / 5 cm polystyrene | 4.99 | 4.96 | -0.60 |
| 120 kVp / 5 cm polystyrene | 5.92 | 5.91 | -0.17 |
| 65 kVp / 10 cm polystyrene | 3.66 | 3.66 | 0.00 |
| 100 kVp / 10 cm polystyrene | 5.88 | 5.83 | -0.85 |
| 120 kVp / 10 cm polystyrene | 6.89 | 6.84 | -0.73 |
| | | Mean (%) | -0.88 |

The exposure and HVLs of the open field beams were used to define the spectra that were used for DRR calculation. Scaling the spectra outputs to the measured

outputs allowed for the software to perform calculations based on the exposures actually produced by the system. Creating spectra that had the same HVLs that were measured on the OBI would ensure accurate calculations of the attenuation. The application of the measured HVLs in the production of the spectra is discussed further in Section 5.1.1.

## 4.2 Detector Response Model

The second part of the system model required that the detector be characterized in order to determine how it responds to different exposures. The characteristic curves of the detector for various open fields are shown in Figure 4.3. The pixel values measured on the detector were converted to a saturation percentage (Equation 3.2) and plotted as a function of the mR at the detector surface. The error bars on the points represent the standard deviations of the pixels values in the image ROI. The slope of each line is called the "detector response" to the various beam qualities (Table 4.3). The level of detector saturation increases linearly with the exposure to the detector until it saturates, resulting in no further change in the pixel value regardless of the increase in exposure. The characteristic curves display the distinct energy dependence of the detector. Each kVp that was used resulted in saturation at different exposure levels, meaning that the saturation rate varied as a function of the beam quality. As shown in Table 4.3, the detector saturates at a rate of 11.13% per mR when exposed to a 150 kVp beam. This response is significantly higher than the 2.56%$Sat$/mR seen at 40 kVp. The characteristic curves also display how the energy dependence changes with increasing beam quality. The difference in response between 65 and 80 kVp is 1.83%$Sat$/mR, while the difference in detector response between 135 and 150 kVp is only 0.30%$Sat$/mR. The change in the rate of saturation shows that the detector is significantly more sensitive to changes in beam quality at lower energies.

Due to the energy dependence of the detector and the fact that beams exiting imaged objects can have a wide range of beam qualities, the response of the detector was modelled based on the HVL of the x-rays reaching the detector. The response of the detector to different HVLs was determined by plotting the slopes of the open field characteristic curves (Table 4.3) as a function of their corresponding HVLs. As mentioned in Section 3.1.2, the model was extended to higher HVLs by hardening the beams by different thicknesses of material (Table 3.1) and measuring the detector response.

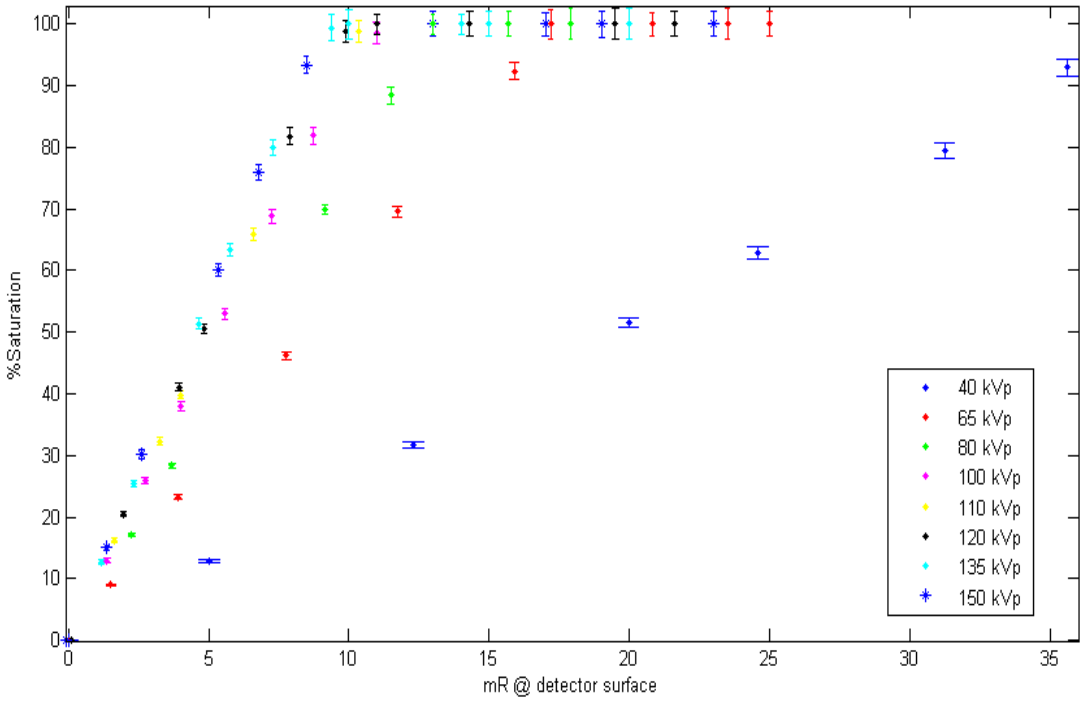


Figure 4.3: Characteristic curves for open field exposures.

Table 4.3: Detector response to open field exposures.

| Tube potential (kVp) | Detector Response (%Sat/mR) |
|---|---|
| 40 | 2.56 |
| 65 | 5.84 |
| 80 | 7.67 |
| 100 | 9.20 |
| 110 | 9.73 |
| 120 | 10.20 |
| 135 | 10.83 |
| 150 | 11.13 |

In order to verify that only the primary radiation was measured, the air gap used for the measurements was tested with a 135 kVp beam hardened by 15 cm of Solid Water and 5 cm of polystyrene. Figure 4.4 shows that as the air gap between the exit side of the material and the ionization chamber at isocenter is increased, the exposure measured at isocenter decreases. The decrease in exposure is due to the decrease in scattered radiation at the point of measurement. It can be seen that as the air gap increased from 40 to 50 cm, the exposure decreased by 1.6%. Increasing the air gap to 58 cm by placing the material directly against the source housing only decreased

the exposure by an additional 0.3%. Therefore, with a 58 cm air gap (the maximum that could be achieve for this setup), scattered radiation had been effectively removed from the measurement as additional increases in the air gap would result in negligible decreases in the exposure. Since this setup would result in the greatest amount of scatter based on thickness and kVp, it can be assumed that scattered radiation was negligible in the other measurements used in creating the model as well. The OBI detector was also an additional 50 cm from the ionization chamber so scattered photons from the material would not effect the pixel values produced during imaging.

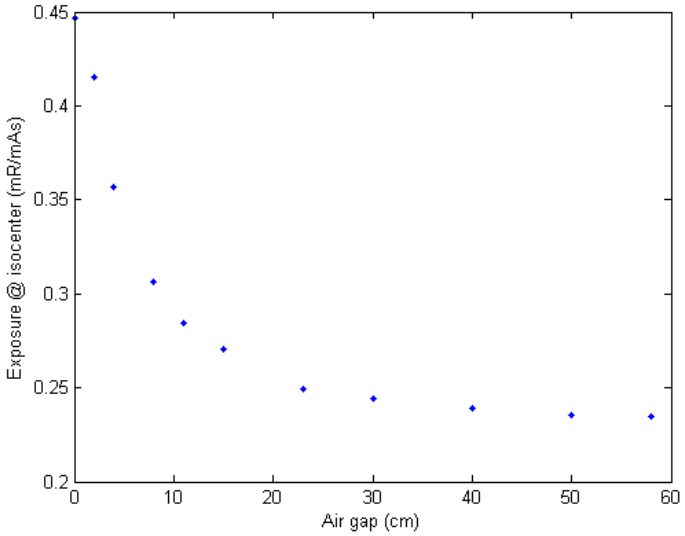


Figure 4.4: The total exposure decreases with increasing air gap and approaches a limit where scattered radiation has been completely eliminated from the measurement.

The data used to model the detector response is shown in Figure 4.5. The points representing the open field response displays how the change in response decreases with increasing HVL as the curve is clearly not linear. The data from the hardened fields appear to continue the trend, with responses measured for beam qualities up to 10.5 mmAl. A logarithmic curve was fit to the data, giving an equation for the detector response (%Sat/mR) as a function of the half-value layer:

$$\frac{\%Sat}{mR} = a\ \ln(HVL) + b, \tag{4.1}$$

where

$$a = 6.87 \pm 0.50,\ \ b = -0.14 \pm 0.92. \tag{4.2}$$

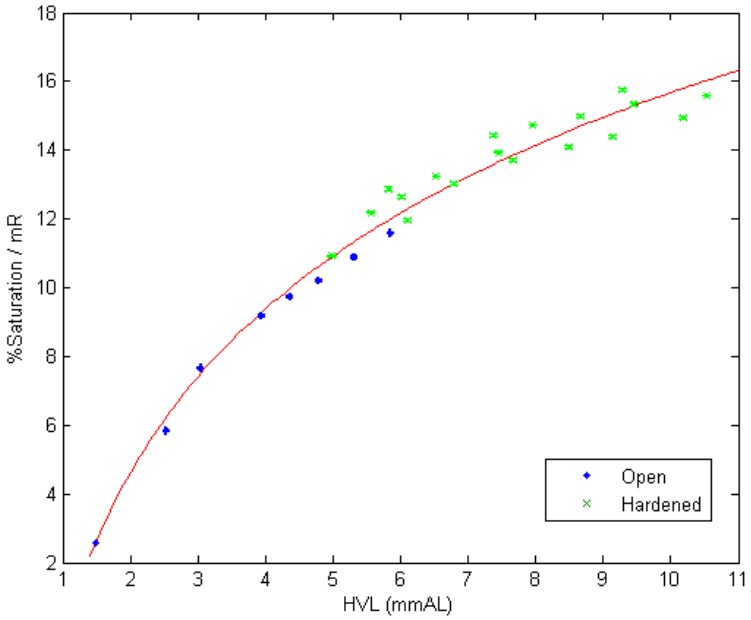


Figure 4.5: Response of the OBI detector to various beam qualities. Error bars on the plot are smaller than the data points.

The uncertainties on the coefficients $a$ and $b$ are the 95% confidence bounds on the values, given the data from Figure 4.5. Each data point in Figure 4.5 represents the mean of several measurements (exposures at various mAs) and the errors bars represent the standard error in the measurements. The errors on the points were less than 1% and too small to display on the figure as scaled. However, the data points are scattered around the trend line, as shown by the relatively high uncertainties on the coefficients of the curve. The values calculated by the trend line vary from the measured data up to 7.2%, with a mean absolute percent error of 3.1% and a mean percent error of 0.1%. The mean percent error shows that the curve is equally likely to over predict the response given a HVL as it is to under predict.

Figure 4.6 shows the response curve that was created for a separate OBI system by repeating the same set of measurements outlined in Section 3.1.2. The response of the second system appeared very similar to the original OBI system, except for a slight scaling in the $\%Sat/\text{mR}$. The measured points fluctuate around the trend line in a very similar matter seen in Figure 4.5. The mean absolute percent error and mean percent error are 3.1% and 0.1%, and are equivalent to the values measured on the original system. The similarities between the curves on the two systems shows

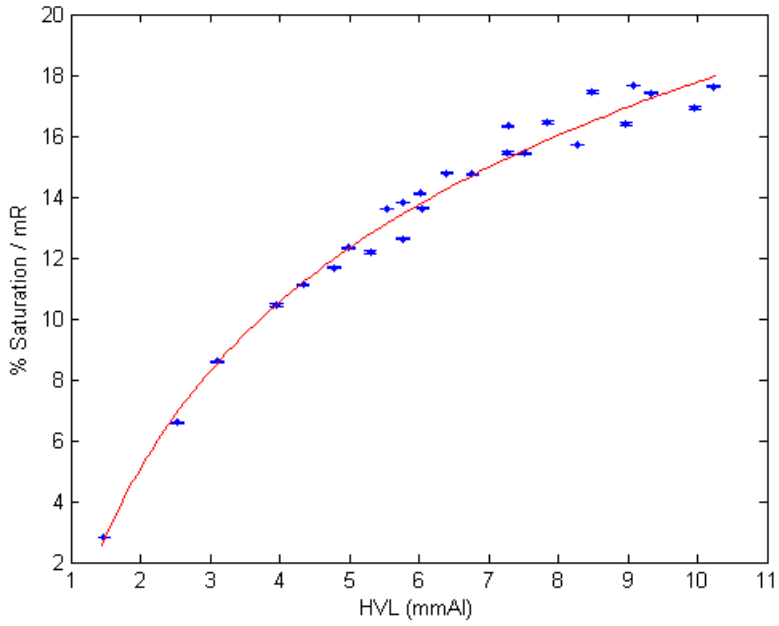


Figure 4.6: Detector response curve for a second OBI system

that the deviation of the measured data is unlikely due to random measurement error. More likely, the lack of a smooth curve is a product of the energy dependence of the detector and its response to different energy spectra.

Two field can potentially have the same HVL but different overall spectra, causing the detector to respond at unequal rates. For example, the 150 kVp open beam causes a detector response of 11.1 $\%Sat$/mR, while the 100 kVp beam filtered by 10 cm of polystyrene resulted in a detector response of 12.9 $\%Sat$/mR, even though the two fields have very similar HVLs (5.84 and 5.82 mmAl, respectively). The energy dependence of the detector was shown in Figure 4.3 where lower energies result in less detector saturation. The 150 kVp spectrum contains low energy photons that contribute to the measured exposure (mR), but not to the $\%Sat$ at the same rate, therefore resulting in a lower $\%Sat$/mR. The 10 cm of polystyrene filters out (hardens) the 100 kVp beam and removes many of the lowest energy photons. The remaining photons that contribute to the exposure also contribute more to the detector saturation, and therefore the $\%Sat$/mR is greater for the filtered 100 kVp field than for the open 150 kVp field. Due to the dependence of the detector on the energy distribution of the spectrum, solely using the HVL to predict the detector response is subject to inaccuracies.

The detector was monitored to observe any trends in the response over time, as was done for the system output. Figure 4.7 shows the $\%Sat/\text{mR}$ of the detector measured over the same 14 week period. Similar to the system output, the response of the detector was seen to fluctuate around the mean values of 7.61 and 9.27 $\%Sat/\text{mR}$ for 80 and 100 kVp beams, respectively. The standard deviations of the data for the two energies were 0.06 and 0.05 $\%Sat/\text{mR}$. Similar to the data measured for the x-ray tube, no long term trends were seen in the detector response and there was no correlation between the response and time of measurement with respect to the system's use.

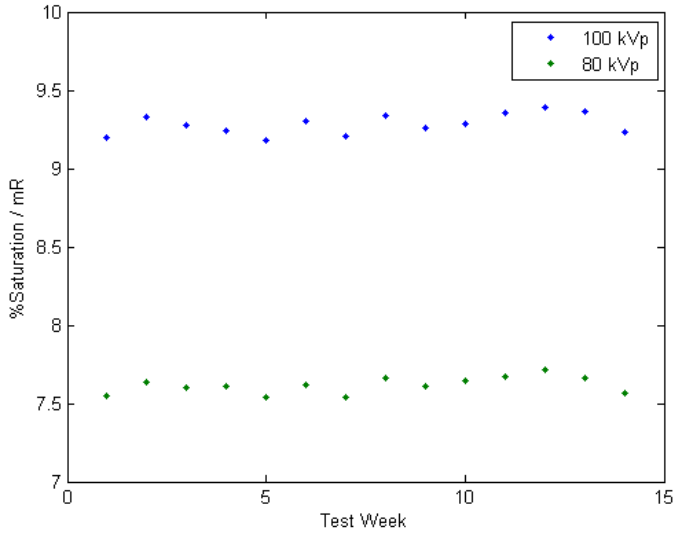


Figure 4.7: Detector response ($\%Sat/\text{mR}$) for 80 and 100 kVp measured over 14 weeks.

## 4.3 Scatter Model

The data presented in Section 4.2 allows for the detector response to be calculated given the exposure and quality of a beam incident on the OBI detector's surface. However, the response model was based on primary measurements only and does not include the addition of scattered photons that will effect the exposure and contribute to the detector saturation. In order to include the scatter, data was gathered to model the scatter fraction under various exposure situations. The scatter fraction was modelled based on the patient thickness, imaging field size, and the tube potential.

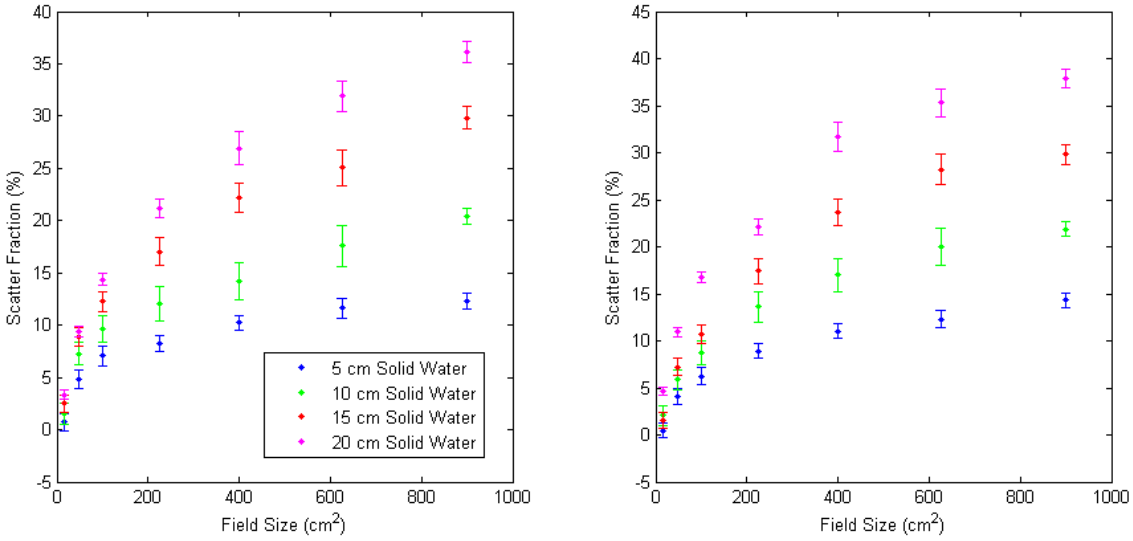


Figure 4.8: Scatter fraction as a function of field size for various thicknesses of scattering material for 100 kVp (left) and 135 kVp (right) x-rays.

Figure 4.8 shows how the scatter fraction (in percent of the total exposure) changes as a function of the field size for different thicknesses of Solid Water placed at isocenter. Each data point represents the mean of several measurements performed at various mAs, and the error bars in the plots represent the standard errors in the measured data. Changes in small field sizes, for example from a $4 \times 4$ cm$^2$ field to a $7 \times 7$ cm$^2$, result in the greatest change in the scatter fraction, as seen by the steep gradient of the plots close to zero. Further increases in the field size causes the scatter fraction to approach a limit, due to the finite range of scattered photons. Smaller thicknesses of scattering material appear to reach this plateau more rapidly. Figure 4.8 also shows how differences in the kVp can effect the change in the scatter fraction. The set of data on the right (taken at 135 kVp) appears to have slightly greater scatter fractions than the data on the left (taken at 100 kVp), but the overall shapes of the curves are maintained. Figure 4.9 shows the scatter fraction as a function of the kVp for a $25 \times 25$ cm$^2$ field. There is a small increase in the scatter fraction with increasing kVp and is greatest for larger thicknesses of scattering material. When increasing the tube potential from 80 to 135 kVp, the scatter fraction for 5 cm of Solid Water increases from $11.6 \pm 0.3\%$ to $12.3 \pm 2.0\%$, while the scatter fraction for 20 cm of Solid Water increases from $30.2 \pm 0.2\%$ to $35.3 \pm 2.5\%$.

The increase in the scatter fraction with greater object thickness is due to the presence of more scattering material, but also partially due to the decreased air gap

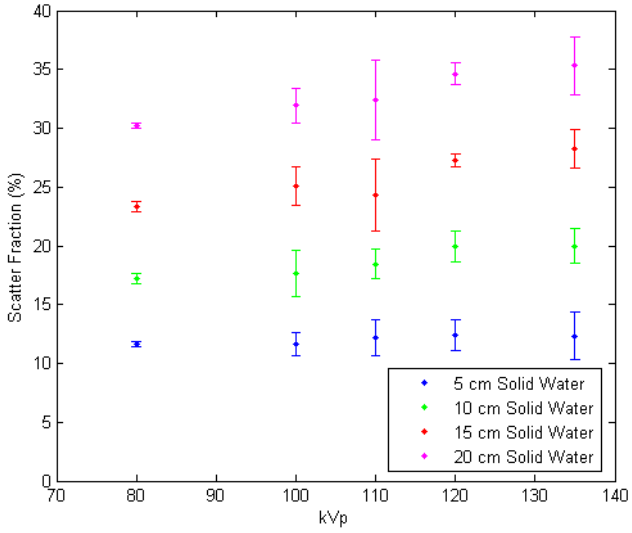


Figure 4.9: Scatter fraction as a function of kVP for various thicknesses of scattering material for a 25 × 25 cm$^2$ field.

since the material was centred at isocenter. The values were measured with the material at isocenter in order to replicate what would be seen in actual treatment scenarios. Therefore, the values for the scatter fraction measured here are unique to the setup used in on-board imaging. The measured scatter fraction data gives an approximation of the scatter fraction for any exposure situation within the limits of the measurements. The data was compiled into tables (Tables A.1 and A.2) that could be used to calculate the scatter fraction by interpolating thicknesses and field sizes and scaling based on the tube potential. Therefore, the contributions of scatter to the detector saturation per mAs could be determined assuming that the primary detector response is known (Equation 3.5).

## 4.4 Model Summary

The measurements discussed in the previous sections were performed to characterize the Varian OBI in order to determine whether the detector response could be predicted for any exposure situation. By modelling the response, based on the characteristic curves of the detector, a response equation (Equation 4.1) was determined as a function of the half-value layer of the x-ray spectrum that interacts with the

detector. Substituting the response equation in Equation 3.6 gives

$$\frac{\%Sat}{mAs} = \frac{mR}{mAs_{(P)}} \times [6.87\ln(HVL) - 0.14] \times (1 - SF)^{-1} . \tag{4.3}$$

The values for the scatter fraction ($SF$) were measured based on field size, object thickness, and tube potential. Knowing the exposure specific scatter fractions will allow one to calculate the total $\%Sat/$mAs given that the output and the beam quality are known. Therefore, for any given exposure, the mAs required to achieve any desired level of detector saturation can be determined as long as information about the x-ray spectrum incident on the detector is known.

# Chapter 5

# Calculation Results

The data presented in Chapter 4 was used to characterize the OBI system and develop a system model. The system model is used along with virtual spectra and CT datasets of an imaged object to determine the attenuation and subsequent detector response via the ray trace algorithm described in Chapter 3. The following chapter presents the results of the DRR calculations when applied to phantoms with varying degrees of complexity, as well as to clinical patient data.

## 5.1 DRR Production Results

### 5.1.1 X-Ray Spectrum Production

The calculation of DRRs required passing a virtual spectrum though the imaged object. As discussed in Section 3.2.1, the spectrum was the only part of the DRR calculation that was not directly measured and modelled. In order to ensure the accuracy of the SpekCalc software, the calculated HVLs were compared to the values measured on the OBI. Table 5.1 shows that the absolute differences between the measured an calculated values are fairly uniform over the range of kVp measured, varying by an average of 0.03 mmAl. The differences resulted in the greatest relative percent differences in the lower beam qualities (-3.42% at 40 kVp). The mean of the percent difference (-0.51%) showed that SpekCalc tended to slightly under predict the HVLs, but the differences were generally within the measurement uncertainty. Overall, SpekCalc was able to accurately determine the HVLs for the range of tube potentials on the OBI.

Different spectra can potentially have the same HVL, so it was important to ensure

Table 5.1: Comparison of the HVLs measured for open beams on the OBI to the values calculated by the SpekCalc software.

| kVp | Measured (mmAl) | SpekCalc (mmAl) | Difference (%) |
|---|---|---|---|
| 40 | 1.46 ± 0.02 | 1.41 | -3.42 |
| 65 | 2.53 ± 0.01 | 2.49 | -1.58 |
| 80 | 3.04 ± 0.01 | 3.08 | 1.32 |
| 100 | 3.94 ± 0.01 | 3.96 | 0.51 |
| 110 | 4.36 ± 0.01 | 4.35 | -0.23 |
| 120 | 4.77 ± 0.01 | 4.73 | -0.84 |
| 135 | 5.31 ± 0.01 | 5.30 | -0.19 |
| 150 | 5.84 ± 0.02 | 5.86 | 0.34 |
| | | Mean (%) | -0.51 |

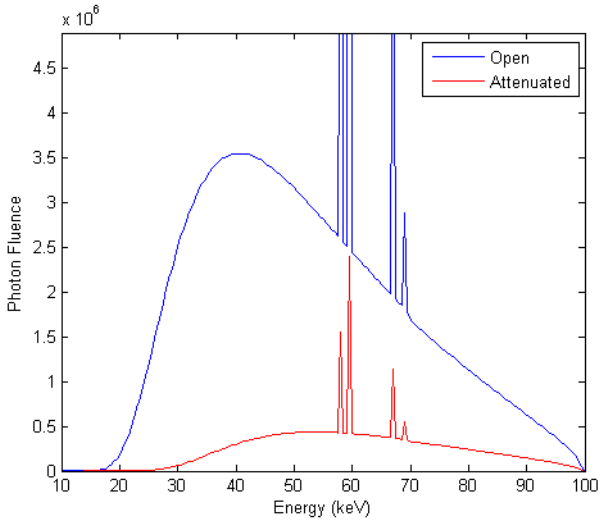


Figure 5.1: The change in an x-ray spectrum when an open 100 kVp beam (blue) is attenuated by 75 mm of water and 3 mm of Al (red).

that the overall shape of the spectra produced by SpekCalc were accurate. Figure 5.1 shows how the spectrum for a 100 kVp beam changes as it is attenuated by 7.5 cm of water and 3 mm of aluminium. The attenuated spectrum is dependent on the shape of the incident spectrum. The HVL of different spectra may be equal, but the attenuation of the overall spectra will not be the same. Therefore, the HVLs of the spectra will change at different rates as they are attenuated. If SpekCalc can predict the HVL of beams that have been attenuated by various amounts of material then the incident spectra produced by SpekCalc will be shown to accurately represent the spectra produced by the OBI. Table 5.2 shows the comparisons between

several measured and calculated HVLs of beams that have been hardened by various thicknesses of water and aluminium. A comprehensive list of measurements is given in Table A.3.

Table 5.2: Comparison of the HVLs measured for hardened beams on the OBI to the values calculated by the SpekCalc software.

| Filtration | kVp | Measured (mmAl) | SpekCalc (mmAl) | % Difference |
|---|---|---|---|---|
| 5 cm water, 3 mm Al | 100 | 6.98 ± 0.02 | 6.89 | -1.29 |
| 5 cm water, 3 mm Al | 120 | 7.99 ± 0.02 | 7.92 | -0.88 |
| 7.5 cm water | 65 | 4.20 ± 0.02 | 4.33 | 3.09 |
| 7.5 cm water | 100 | 6.51 ± 0.03 | 6.56 | 0.77 |
| 7.5 cm water, 3 mm Al | 65 | 4.76 ± 0.02 | 4.93 | 3.57 |
| 7.5 cm water, 3 mm Al | 100 | 7.35 ± 0.01 | 7.39 | 0.54 |
| 1 mm Al | 65 | 2.91 ± 0.01 | 3.05 | 4.81 |
| 1 mm Al | 100 | 4.52 ± 0.02 | 4.58 | 1.33 |

SpekCalc was able to determine the HVLs for the hardened beams within 5% of the measured data. The majority of the calculated values were within 2% of the measured data, with the greatest differences appearing at the lower energies (65 and 80 kVp), possibly due to differences in the very low energy fluences that are filtered out from the spectrum. As the amount of filtration increased, the differences tended to decrease. Overall, the mean percent difference between the calculated and measured values was 0.85%, showing that SpekCalc tended to slightly over predict the HVLs for hardened beams. Despite the large amounts of filtration used, the two methods were very comparable. The results show that the incident spectra that are produced by SpekCalc, along with the inputs that were selected for the OBI, accurately model the spectra emerging from the x-ray tube.

### 5.1.2 CT Data Conversion

In order to calculate the attenuation of the incident spectra through an imaged object, the CT data must be converted to linear attenuation coefficient values for each of the energies in the spectra. The linear attenuation coefficients of the inserts in the Catphan and CIRS phantoms were plotted as a function of their CT numbers to generate a HU to $\mu$ conversion curve, as discussed in Section 3.2.2. Due to the change in the attenuation coefficient with energy, a separate curve was generated for every energy from 0 to 150 keV (in 2 keV intervals). Figure 5.2 shows the conversion for

several energies in the diagnostic spectrum and clearly displays why different curves are needed for each energy due to the large change in the attenuation coefficients with energy, especially in higher HU material. By a similar process, the electron densities (relative to water) were plotted as a function of the HU of the different materials in the CIRS phantom. The electron density conversion curve (Figure 5.3) that was generated using the CIRS data was used to determine the water equivalent thickness of the imaged object.

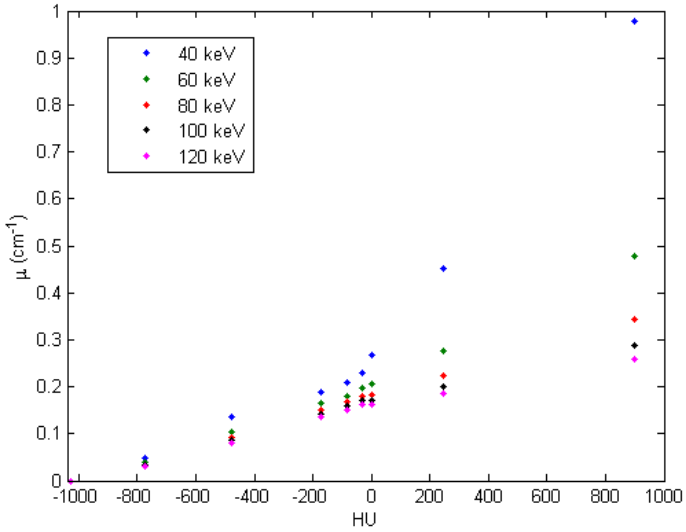


Figure 5.2: Conversion from HU of CT data to the linear attenuation coefficient ($\mu$) for several energies in the diagnostic spectrum.

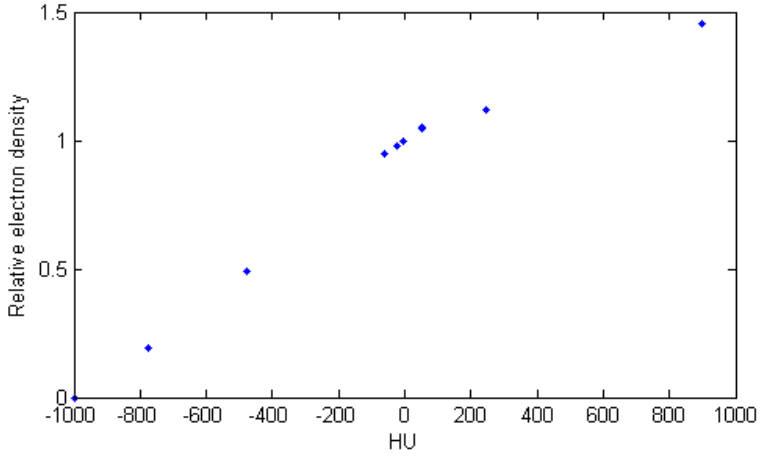


Figure 5.3: Conversion from HU of CT data to the electron density relative to water.

### 5.1.3 Ray Trace Validation

The spectra produced by SpekCalc were used in the ray trace program with CT data generated for three simple block phantoms. Due to the uniformity of the image (no contrast), the emerging spectra were only calculated in a small (15 × 15 pixel) ROI in the center of the image and the mR/mAs and HVL were compared to the values that were measured for the same phantoms on the OBI. Tables 5.3 and 5.4 compare the exposures (mR/mAs) and the HVLs (mmAl) of four different tube potentials attenuated by the phantoms. The measured data represents the primary radiation only, as the measurements were performed with a $4 \times 4$ cm$^2$ field size and the material placed at the source housing. Uncertainties on the measured data are given by the standard errors of the mean of the measurements.

Table 5.3: Comparison of the outputs (mR/mAs) measured for attenuated beams on the OBI at isocenter to values calculated by the ray trace program.

| Material | kVp | Measured (mR/mAs) | Calculated | % Difference |
|---|---|---|---|---|
| 10 cm Solid Water | 65 | 0.215 ± 0.001 | 0.207 | -3.78 |
| | 80 | 0.419 ± 0.001 | 0.424 | 1.21 |
| | 100 | 0.814 ± 0.002 | 0.826 | 1.54 |
| | 120 | 1.348 ± 0.005 | 1.366 | 1.39 |
| 10 cm Solid Water, | 65 | 0.140 ± 0.001 | 0.130 | -6.94 |
| 2 cm polystyrene | 80 | 0.275 ± 0.002 | 0.273 | -0.55 |
| | 100 | 0.544 ± 0.001 | 0.544 | -0.08 |
| | 120 | 0.912 ± 0.002 | 0.916 | 0.53 |
| 10 cm Solid Water, | 80 | 0.066 ± 0.001 | 0.061 | -8.16 |
| 5 cm polystyrene, | 100 | 0.144 ± 0.001 | 0.134 | -6.24 |
| 3 cm PMMA | 120 | 0.252 ± 0.001 | 0.233 | -7.45 |

The data presented in Tabel 5.3 shows that the outputs calculated by the ray trace program were generally comparable with the measured outputs. Outputs calculated for phantoms composed of only Solid Water and polystyrene were within 2% of the measured data, except for the outputs measured at 65 kVP (-3.78% and -6.94% for the two phantoms). The results for the third phantom had differences of -6.24% for 100 kVp to 8.16% for 80 kVp. The greater difference in outputs appears to result from the addition of PMMA. Solid water and polystyrene have average CT numbers of approximately 30 and -30 HU respectively. As shown in Figure 5.2, the majority of the data used in the HU to $\mu$ curve were around water (0 HU). PMMA has a CT number of approximately 135 HU. Therefore, the attenuation coefficients for higher

HU materials appear to be slightly over predicted.

Table 5.4: Comparison of the HVLs (mmAl) measured for attenuated beams on the OBI to values calculated by the ray trace program.

| Material | kVp | Measured (mmAl) | Calculated | % Difference |
|---|---|---|---|---|
| 10 cm Solid Water | 65 | 4.73 ± 0.02 | 4.78 | 1.27 |
| | 80 | 5.96 ± 0.02 | 5.93 | -0.50 |
| | 100 | 7.35 ± 0.01 | 7.28 | -0.95 |
| | 120 | 8.48 ± 0.01 | 8.41 | -0.83 |
| 10 cm Solid Water, | 65 | 4.88 ± 0.02 | 4.93 | 1.02 |
| 2 cm polystyrene | 80 | 6.16 ± 0.01 | 6.13 | -0.49 |
| | 100 | 7.60 ± 0.01 | 7.53 | -0.92 |
| | 120 | 8.67 ± 0.03 | 8.66 | 0.12 |
| 10 cm Solid Water, | 80 | 6.70 ± 0.01 | 7.20 | 7.46 |
| 5 cm polystyrene, | 100 | 8.23 ± 0.01 | 8.74 | 6.19 |
| 3 cm PMMA | 120 | 9.37 ± 0.02 | 9.94 | 6.08 |

The results for the exposure calculations are mirrored in the comparison of the measured and calculated HVLs (Table 5.4). The exposures that had the highest agreement between measured and calculated outputs also had the highest agreement in the HVLs, all within 1% of the measured values. Similarly, the exposures that resulted in the worst agreements in the outputs has the worst agreements in the HVLs. The correlation between the values is expected because the spectrum that emerges from the volume is used to calculate both the output and the HVL. An over prediction of the attenuation, resulting in an under prediction in the output, implies that the beam hardening, and hence the HVL, is also being over predicted. The effects of the attenuation are seen in the PMMA phantom where the calculated outputs were less than the measured outputs, and the calculated HVLs were greater than the measured HVLs.

The calculated outputs (corrected to the detector surface) and HVLs were used in the detector response model (Equation 4.3) to determine the level of detector saturation per mAs resulting from each exposure. Table 5.5 shows the comparison of the calculated values to the values actually produced by the OBI detector for each phantom and kVp combination. The accuracy of the calculation in predicting the detector saturation varied widely between the different exposures. The differences agree with the phantoms and kVps that had large differences in the calculated HVLs and outputs, as these values were obviously used to calculate the detector satura-

tion. However, even some of the calculated outputs and HVLs that agreed with the measured values resulted in larger differences in the response. For example, the output and HVL of the 80 kVp field attenuated by 10 cm of Solid Water and 2 cm of polystyrene were both within 1% of the measured values, but the $\%Sat/\text{mAs}$ was -7.6% lower than the response produced by the detector. The difference in the results relates to the uncertainties in the response curve discussed in Section 4.2, which was shown to deviate from the modelling data by up to 7%.

Table 5.5: Comparison of the detector saturation ($\%Sat/\text{mAs}$) measured for attenuated beams on the OBI to values calculated by the ray trace program.

| Material | kVp | Measured ($\%Sat/\text{mAs}$) | Calculated | % Difference |
|---|---|---|---|---|
| 10 cm Solid Water | 65 | 1.00 ± 0.01 | 0.98 | -2.69 |
| | 80 | 2.42 ± 0.01 | 2.28 | -5.82 |
| | 100 | 5.26 ± 0.03 | 4.96 | -5.74 |
| | 120 | 8.75 ± 0.07 | 8.80 | 0.53 |
| 10 cm Solid Water, | 65 | 0.66 ± 0 | 0.63 | -5.41 |
| 2 cm polystyrene | 80 | 1.62 ± 0 | 1.50 | -7.59 |
| | 100 | 3.51 ± 0.03 | 3.32 | -5.37 |
| | 120 | 6.02 ± 0.04 | 5.99 | -0.59 |
| 10 cm Solid Water, | 80 | 0.42 ± 0 | 0.36 | -13.99 |
| 5 cm polystyrene, | 100 | 0.97 ± 0.01 | 0.88 | -10.06 |
| 3 cm PMMA | 120 | 1.71 ± 0.01 | 1.62 | -4.81 |

The data presented in Table 5.5 gives the detector response to primary radiation only. The same set of measurements were performed with larger field sizes ($10 \times 10$ and $20 \times 20$ cm$^2$) with the phantoms placed at the system's isocenter. The scatter fractions for the measurements were determined using the data from Section 4.3 along with the calculated Solid Water equivalent thicknesses of the phantoms. The phantom composed of 10 cm of Solid Water was obviously determined to have a Solid Water equivalent thickness of 10 cm. The addition of 2 cm of polystyrene increased the equivalent thickness to 11.9 cm, while the addition of 5 cm of polystyrene and 3 cm of PMMA resulted in an equivalent thickness of 18.1 cm. The total exposures, with the addition of scatter are shown in Tables 5.6 and 5.7.

The calculated detector responses with the addition of scattered radiation showed similar agreement with the measured values as the primary data. No significant changes in the difference between the measured and calculated values were observed, showing that the addition of scatter resulted in only minor additional uncertainties.

Scatter fractions for the different exposures ranged from 0.09 to 0.28 depending on the thickness, field size, and kVp. The majority of the calculated values were within 5% of the measured values. Again, several large differences were observed, despite the accurate calculation of the HVL, primary outputs, and scatter fractions, resulting from the uncertainty in the response equation. The absolute differences in the $\%Sat$/mAs however are very small, many of which are within the uncertainties of the measured data. Despite relative differences on the order of 5 to 10%, the differences in the actual response have a minimal effect on the ability to predict the detector saturation. For example, a 0.3 $\%Sat$/mAs difference in the response will only result in a 3 $\%Sat$ difference in the total detector saturation for a 10 mAs exposure.

Table 5.6: Comparison of the detector saturation ($\%Sat$/mAs) measured for attenuated beams on the OBI to values calculated by the ray trace program for a 10 × 10 field with the material placed at the system's isocenter.

| Material | kVp | Measured ($\%Sat$/mAs) | Calculated | % Difference |
|---|---|---|---|---|
| 10 cm Solid Water | 80 | 2.61 ± 0.01 | 2.50 | -4.25 |
| | 100 | 5.63 ± 0.02 | 5.47 | -2.88 |
| | 120 | 9.45 ± 0.13 | 9.67 | 2.25 |
| 10 cm Solid Water, | 80 | 1.76 ± 0 | 1.65 | -5.94 |
| 2 cm polystyrene | 100 | 3.84 ± 0.04 | 3.69 | -3.81 |
| | 120 | 6.49 ± 0.10 | 6.65 | 2.44 |
| 10 cm Solid Water, | 80 | 0.48 ± 0 | 0.42 | -12.4 |
| 5 cm polystyrene, | 100 | 1.11 ± 0.01 | 1.01 | -8.38 |
| 3 cm PMMA | 120 | 1.91 ± 0.03 | 1.88 | -1.49 |

Table 5.7: Comparison of the detector saturation ($\%Sat$/mAs) measured for attenuated beams on the OBI to values calculated by the ray trace program for a 20 × 20 field with the material placed at the system's isocenter.

| Material | kVp | Measured ($\%Sat$/mAs) | Calculated | % Difference |
|---|---|---|---|---|
| 10 cm Solid Water | 80 | 2.81 ± 0.01 | 2.67 | -4.99 |
| | 100 | 6.15 ± 0.04 | 5.80 | -5.65 |
| | 120 | 10.21 ± 0.12 | 10.49 | 2.79 |
| 10 cm Solid Water, | 80 | 1.92 ± 0.01 | 1.79 | -6.92 |
| 2 cm polystyrene | 100 | 4.09 ± 0.18 | 3.97 | -2.72 |
| | 120 | 7.29 ± 0.11 | 7.33 | 0.47 |
| 10 cm Solid Water, | 80 | 0.54 ± 0 | 0.47 | -13.1 |
| 5 cm polystyrene, | 100 | 1.28 ± 0.02 | 1.17 | -8.69 |
| 3 cm PMMA | 120 | 2.15 ± 0.02 | 2.23 | 4.14 |

Table 5.8: Measured and calculated scatter fraction for three phantoms measured with a 15 × 15 cm$^2$ field size at 80, 100, and 120 kVp.

| Phantom & Field Size | kVp | Measured SF | Calculated SF | % Difference |
|---|---|---|---|---|
| Phantom1 | 80 | 14.8 ± 0.3 | 13.9 | -5.98 |
| 15 × 15 cm$^2$ | 100 | 15.7 ± 1.2 | 14.3 | -8.93 |
| | 120 | 16.4 ± 1.1 | 14.6 | -11.2 |
| Phantom2 | 80 | 10.2 ± 0.9 | 10.6 | 4.40 |
| 15 × 15 cm$^2$ | 100 | 11.0 ± 1.6 | 10.7 | -2.52 |
| | 120 | 11.7 ± 1.3 | 10.9 | -6.3 |
| Phantom3 | 80 | 9.53 ± 0.41 | 9.7 | 1.77 |
| 15 × 15 cm$^2$ | 100 | 9.17 ± 1.67 | 9.17 | -0.02 |
| | 120 | 9.56 ± 0.50 | 9.36 | -2.04 |

The ability of the model to predict the scatter fractions for a wider range of materials was tested using the phantoms shown in Table 3.2. The calculated Solid Water equivalent thicknesses of the three phantoms (Phantom1, Phantom2, and Phantom3) were 13.1, 8.6, and 6.1 cm. Using the equivalent thicknesses, the scatter fractions were calculated and compared to the measured values. The comprehensive list of results is given in Table A.4. A sample of the results for the 15 × 15 cm$^2$ fields is given in Table 5.8. Most of the calculated scatter fractions were within the standard errors in the measured data.

## 5.2 Image Results

The previous section presented the comparisons of the calculated detector response in a point to the measured response produced in a small ROI on the OBI. To evaluate the program's ability to predict the saturation in entire images, calculations of 256 × 192 pixel (1.6 mm per pixel) images were created and compared to the full field images acquired on the OBI. The resolution of the images were reduced from the actual OBI resolution (1024 × 768 pixels) in order to decrease calculation times.

### 5.2.1 Phantom Images

Figure 5.4 shows a 20 × 20 cm$^2$ image taken of a phantom composed of a stack of Solid Water and polystyrene where the middle 2 blocks had air cavities drilled through the center along one axis (and arranged perpendicular to each other). The

phantom was imaged on the OBI at 100 kVp and 15.63 mAs. The calculated image (bottom) appears to spatially agree with the image taken on the OBI (top). The obvious difference between the images appears at the field edges. When setting the limits of the calculated images, no points outside of the set bounds were calculated and the detector saturation is left at zero. The actual image taken on the OBI shows how the divergence of the beam and scattered radiation can provide small levels of exposure to the out of field areas.

Profiles through the measured and calculated images were taken in the X-direction at Z = 40. Figure 5.5 shows the two profiles, as well as the percent difference between them at each point. The top set of profiles compares the image taken on the OBI to the primary calculated exposure only. Clearly, the calculated values are approximately 10% lower than the measured values, except for the center peak (crossing the air cavity) that reaches saturation in both images. The addition of the scatter fraction into the image increases the exposure in the calculated image to the levels measured on the OBI. The mean absolute percent difference between the calculated and measured profiles is 2.2%. The greatest difference in the profiles occur at steep gradients in the exposure due to differences in the lower spatial resolution of the calculated values, and at the field edges for the reasons discussed above. It can also be noted that the saturation level at the field edges in the measured profile varies from 82.1 $\%Sat$ to 77.9 $\%Sat$, while the calculated profile is essentially uniform around the central axis. As the x-position of the detector is in the cathode-anode direction of the OBI, the reduction of the beam intensity on the anode side of the field is likely caused by the Heel Effect, the attenuation of the x-rays by the anode itself [22]. This was not an effect that was modelled in the DRR calculation software, therefore resulting in a larger difference in the calculated values near the field edges.

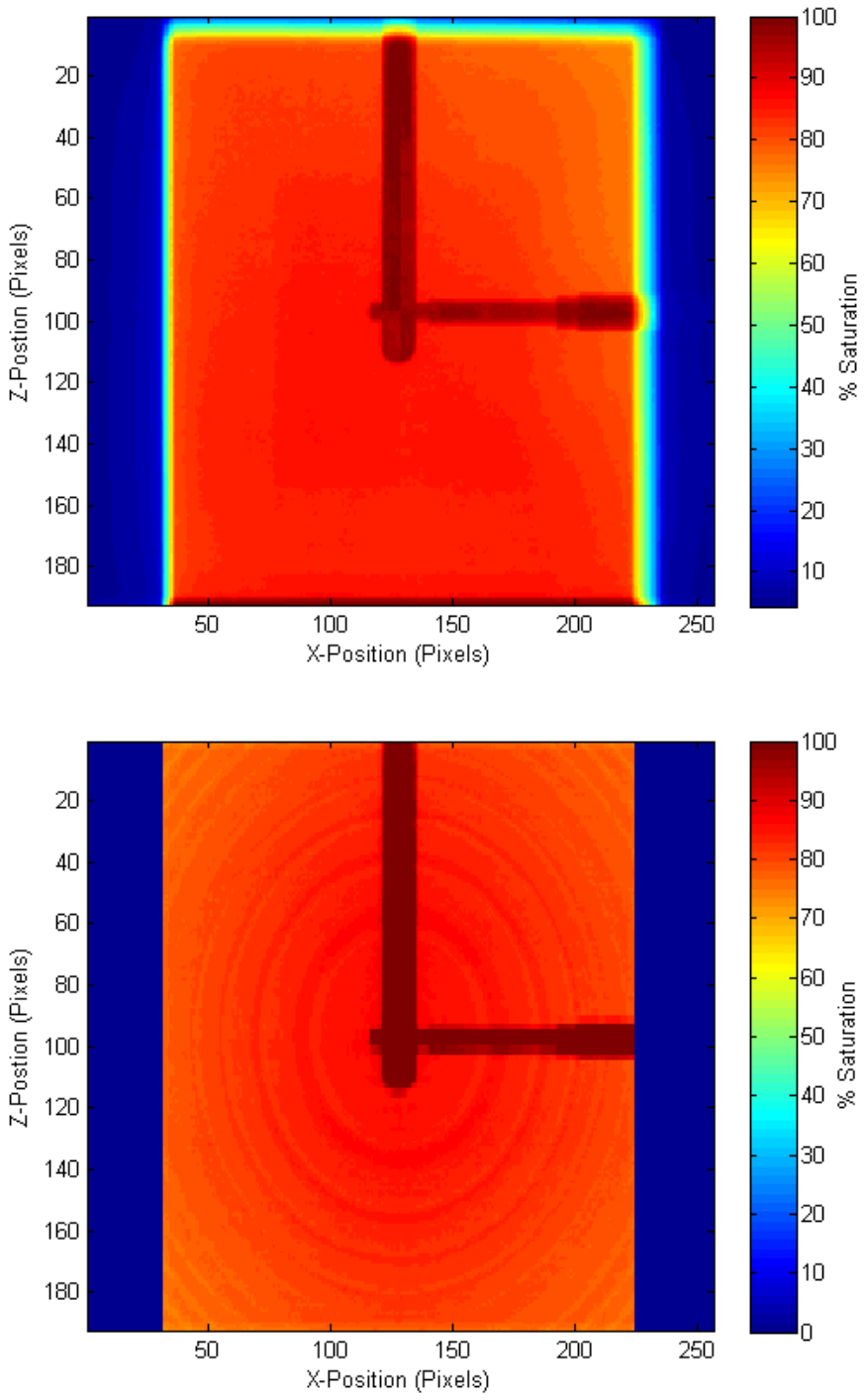


Figure 5.4: The OBI (top) and calculated (bottom) images of a block phantom with air cavities.

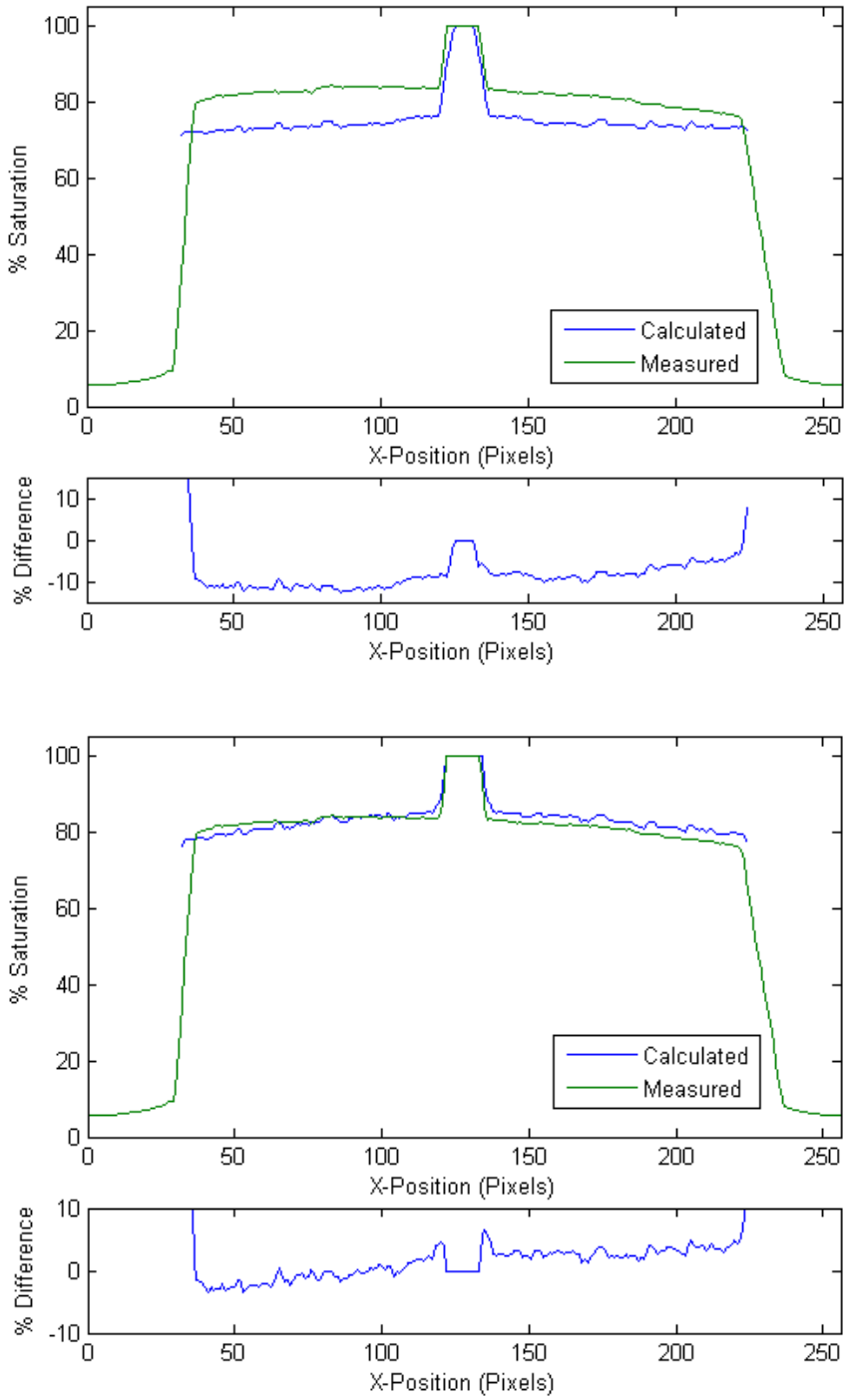


Figure 5.5: Comparison between the measured and calculated x-profiles at z = 40 for the block phantom for primary (top) and total (bottom) exposures.

The DRR calculation software was tested on the significantly more complex Alderson Radiation Therapy (ART) anthropomorphic phantom in order to further observe the calculation accuracy in high contrast objects containing a wider range of materials. Figure 5.6 shows and anterior-posterior 20 $\times$ 20 cm$^2$ radiograph of the upper abdomen of the ART phantom taken on the OBI at 100 kVp and 40 mAs (top), as well as the calculated primary radiograph for the same exposure. Again, the two images appear very similar, with minor spatial differences due to the slight differences between the phantom position in the CT and when the radiograph was taken. Both images clearly display imager saturation in the lung region (upper and lower right corner of the image), even without the addition of scatter in the calculated image. The major difference in the two images appears in the abdominal region (left side of the image), where the radiograph appears to be approximately 10 $\%Sat$ more saturated than the DRR.

The scatter fraction for the upper abdominal radiograph is shown in Figure 5.7 (top). A higher scatter fraction appears in the center of the image as well as in the more dense regions of the phantom, as expected due to the dependence of the field size and equivalent thickness on the scatter fraction. The scatter fractions in the high scatter regions were seen to exceed 0.3, while the scatter fractions in the lung regions near the field edge did not exceed 0.1. With the addition of the scatter fraction, the abdominal radiograph (Figure 5.7 (bottom)) more closely resembles the image taken on the OBI in terms of the saturation level in the abdominal regions.

Profiles through the images are given in Figure 5.8, which displays the comparison of the measured and calculated primary and total values. The X-profile, taken at Z = 161, displays the significant ($\sim$30%) difference in the measured and primary values in the abdominal region. The difference in the two images is not observable in the lung region as both images are saturated, even without the addition of scatter. The bottom image in Figure 5.8 shows that with the addition of scatter the saturation percentage in the abdominal region is increased to the levels seen in the measured values. Based on this profile, the two images appear to agree very well. The mean absolute percent difference between the points in the two profiles is 4.4%. The greatest differences appeared in the steep gradient regions and dense "bone" regions, resulting in differences of approximately 5 to 10%. The sharp increases in the saturation (X = 115, 139) are due to the gaps between slices of the phantom, and appear as the lines in the Z-direction in Figure 5.6. Despite setup deviations, the two images agree very well spatially, with large calculated peaks and valleys in the saturation level

appearing within 3 pixels (4.8 mm) of the measured points. Most importantly, the DRR calculation was able to accurately predict where the detector would become saturated.

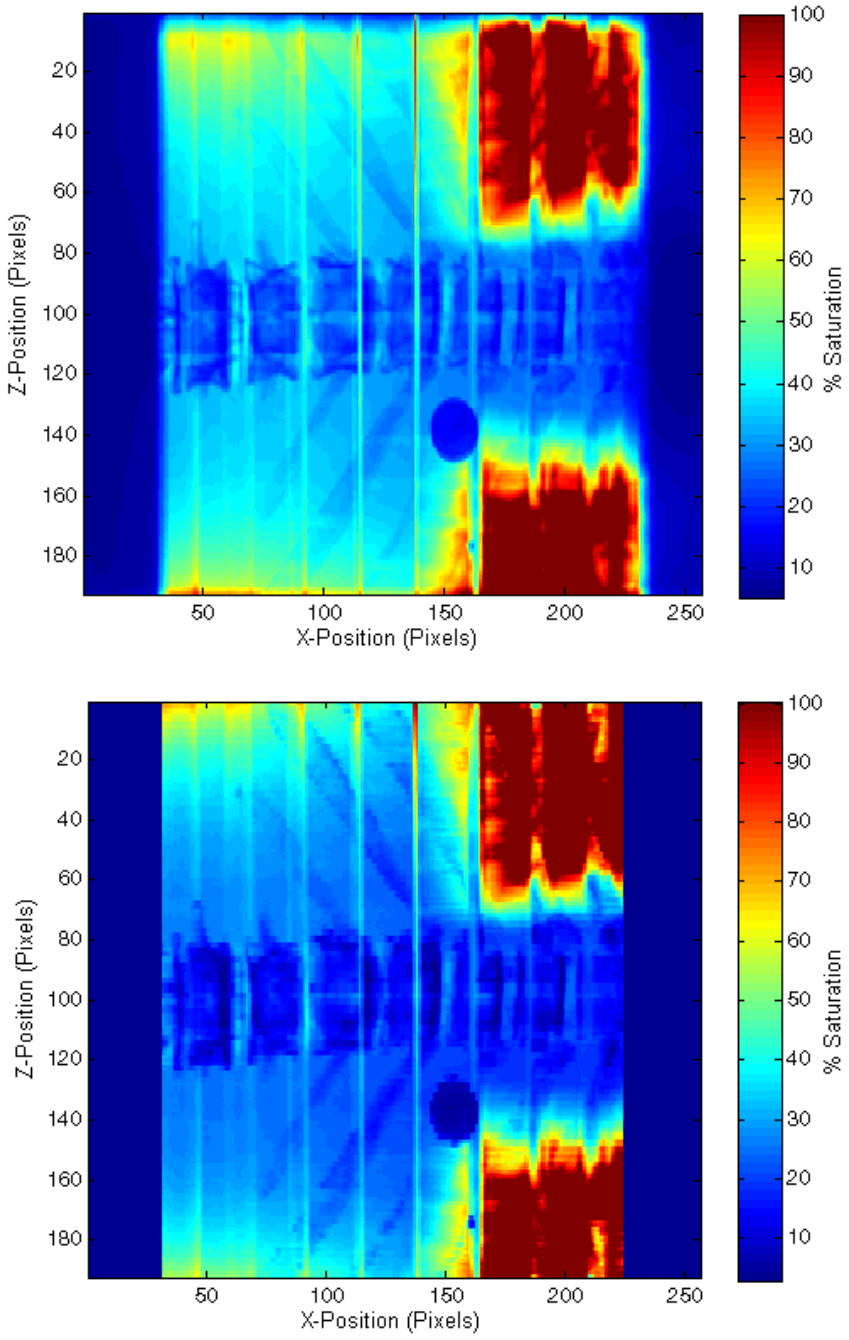


Figure 5.6: A 100 kVp, 40 mAs upper abdominal radiograph of the ART phantom taken on the OBI (top) and calculated by the DRR software (bottom). The calculated image displays only the primary radiation from the exposure.

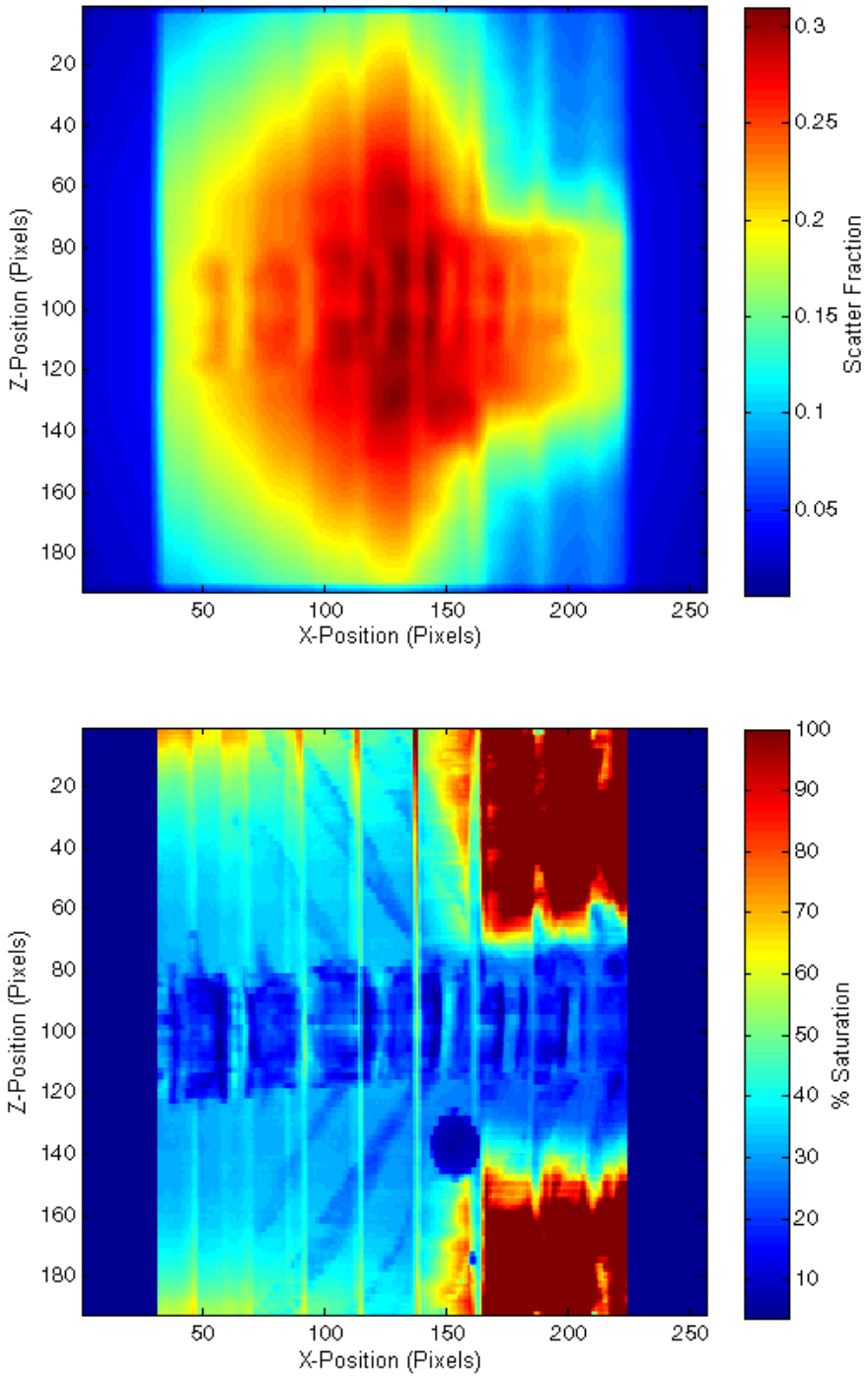


Figure 5.7: Calculated map of the scatter fraction for a 100 kVp upper abdominal radiograph of the ART phantom (top) and the total calculated image with the addition of scatter (bottom).

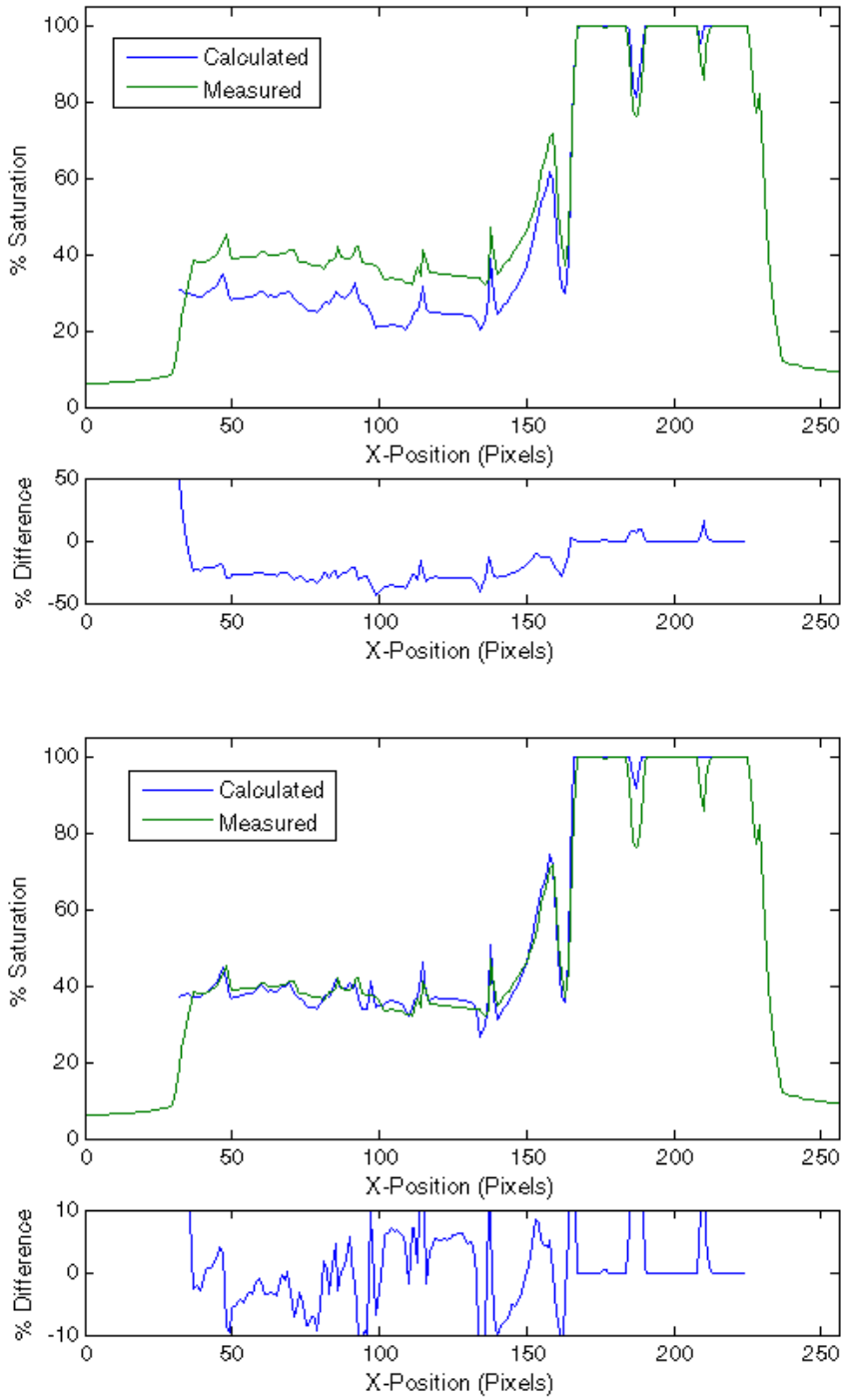


Figure 5.8: Profiles taken through the X-direction of the images in Figure 5.6 at Z = 161, comparing the measured values with the primary (top) and total (bottom) exposures

.

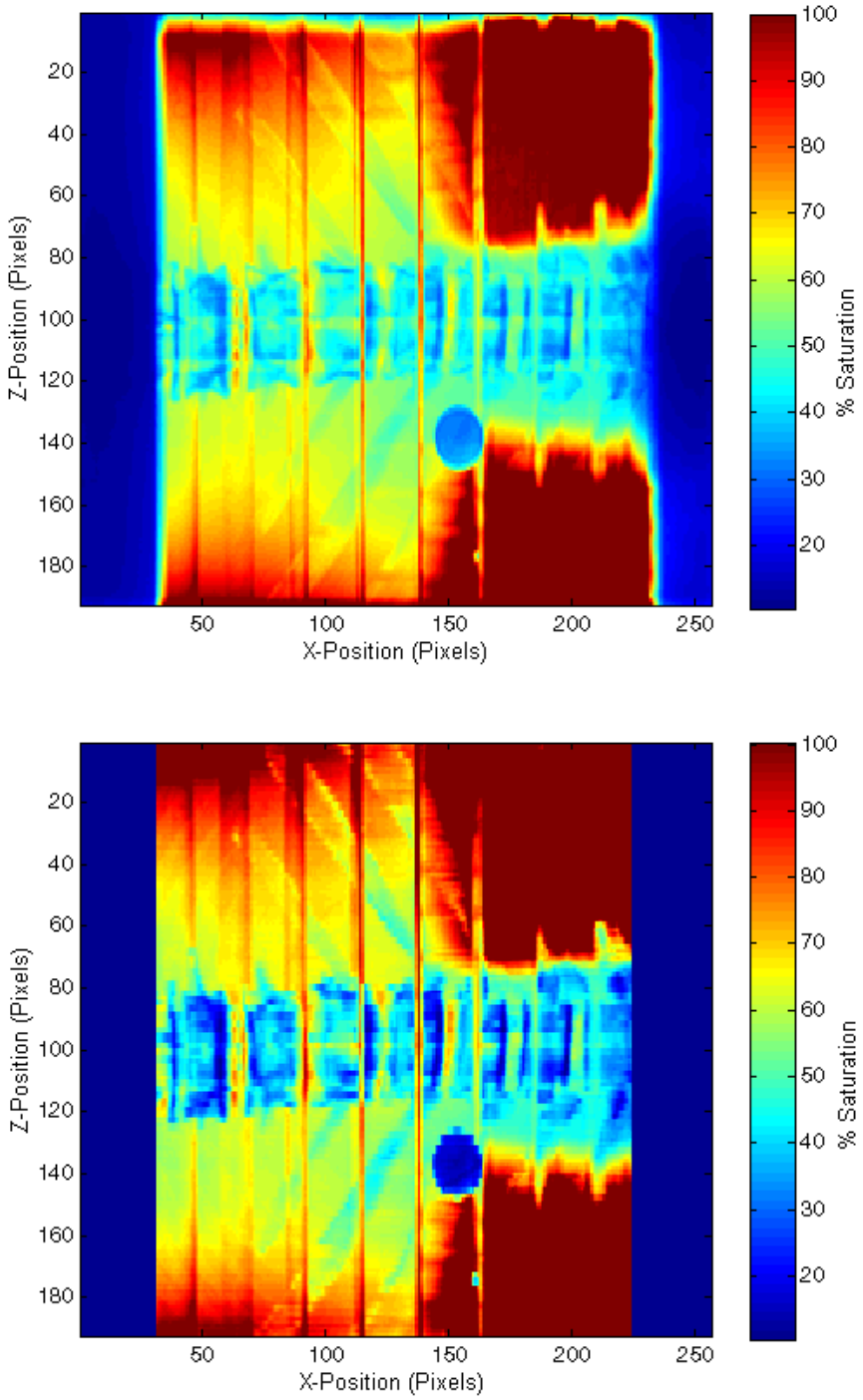


Figure 5.9: A 120 kVp, 40 mAs thoarx radiograph of the ART phantom taken on the OBI (top) and calculated by the DRR software (bottom).

Figure 5.9 shows the same abdominal image taken at 120 kVp and 40 mAs. As expected, the image taken on the OBI (top) is more saturated than the 100 kVp image due to the higher beam quality and mR/mAs. The calculated image (bottom), including scatter, closely resembles the actual saturation levels. The major differences between the two images occur in the under prediction of the detector response in the dense bone regions. The profiles in Figure 5.10 show good agreement between the measured and calculated values, with a mean absolute percent difference of 2.7%, limited mostly by the spatial resolution and the attenuation calculation through dense materials. The DRR calculation was again able to predict where the detector would saturate, with the only difference appearing as a 14.3% over prediction of the saturation for 1 pixel (1.6 mm) at the edge of the saturated volume.

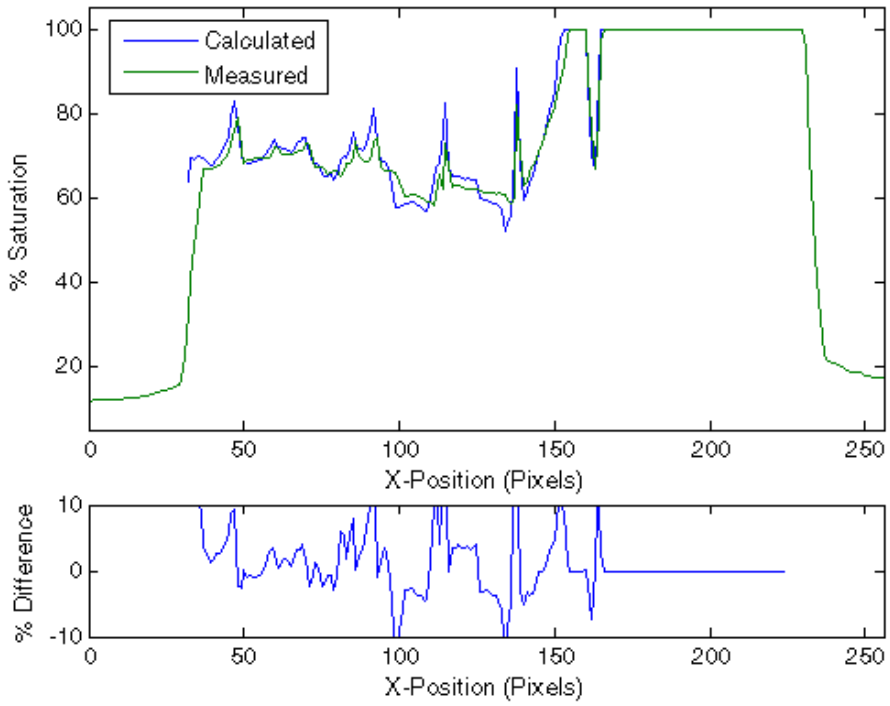


Figure 5.10: X-profile through Z = 161 of the images in Figure 5.9, comparing the calculated and measured values.

Chest radiographs are the most likely to saturate due to the low attenuation of the lung tissue relative to the other anatomy. Figure 5.11 shows a chest radiograph of the ART phantom taken at 120 kVp with 15.63 mAs, where the lungs occupy the majority of the imaged volume. The measured (top) and calculated (bottom) images compare similarly to the trends seen in the abdominal image. The lung region of the images are almost completely saturated. Small regions within the lungs appear to drop in saturation and vary slightly in size between the two images. Figure 5.12 shows the comparisons of an X-profile taken at Z = 40 (top), and a Z-profile taken at X = 145 (bottom). Again, the profiles display good agreement between the measured and calculated values with mean absolute percent differences of 5.2 and 7.4% for the X and Z-profiles, respectively. The larger difference in the Z-profile is due to the 10 to 17% difference in the attenuation across the spine region (Z = 57 to 148). The small differences in the saturated volume did not exceed 5%, except at the edges of steep gradients.

As mentioned in Section 1.2.1, kV setup images are generally taken in orthogonal pairs. A lateral 20 $\times$ 20 cm$^2$ lung image of the ART phantom was taken using 120 kVp and 62.5 mAs. The measured and calculated images are shown in Figure 5.13. The areas of saturation are predicted in all of the areas that were saturated in the measured image. Some of the saturated areas appear larger in the calculated image compared to the measured image. The DRR appears to slightly over predict the saturation in points adjacent to saturated areas. An X-profile through the main saturated area at Z = 100, shown in Figure 5.14 (top), displays how several small drops in the saturation within the saturated area (X = 119) in the measured profile do not appear in the calculated profile. The small peaks are most likely blurred out due to the spatial resolution in the calculated image. Regardless, the overall shapes of the two profiles match very well with a mean absolute percent difference of 4.9% in the lung region, with greater differences (up to 20%) seen near the field edges. The Z-profile in Figure 5.14 was taken through a non-saturated region in the image (X = 165). Within the center of the image, the measured and calculated profiles have a mean absolute percent difference of 6.4%. The profiles appear to match well within the central region but rapidly separate near the field edges, once again clearly showing the large differences in the attenuation calculated for higher density materials.

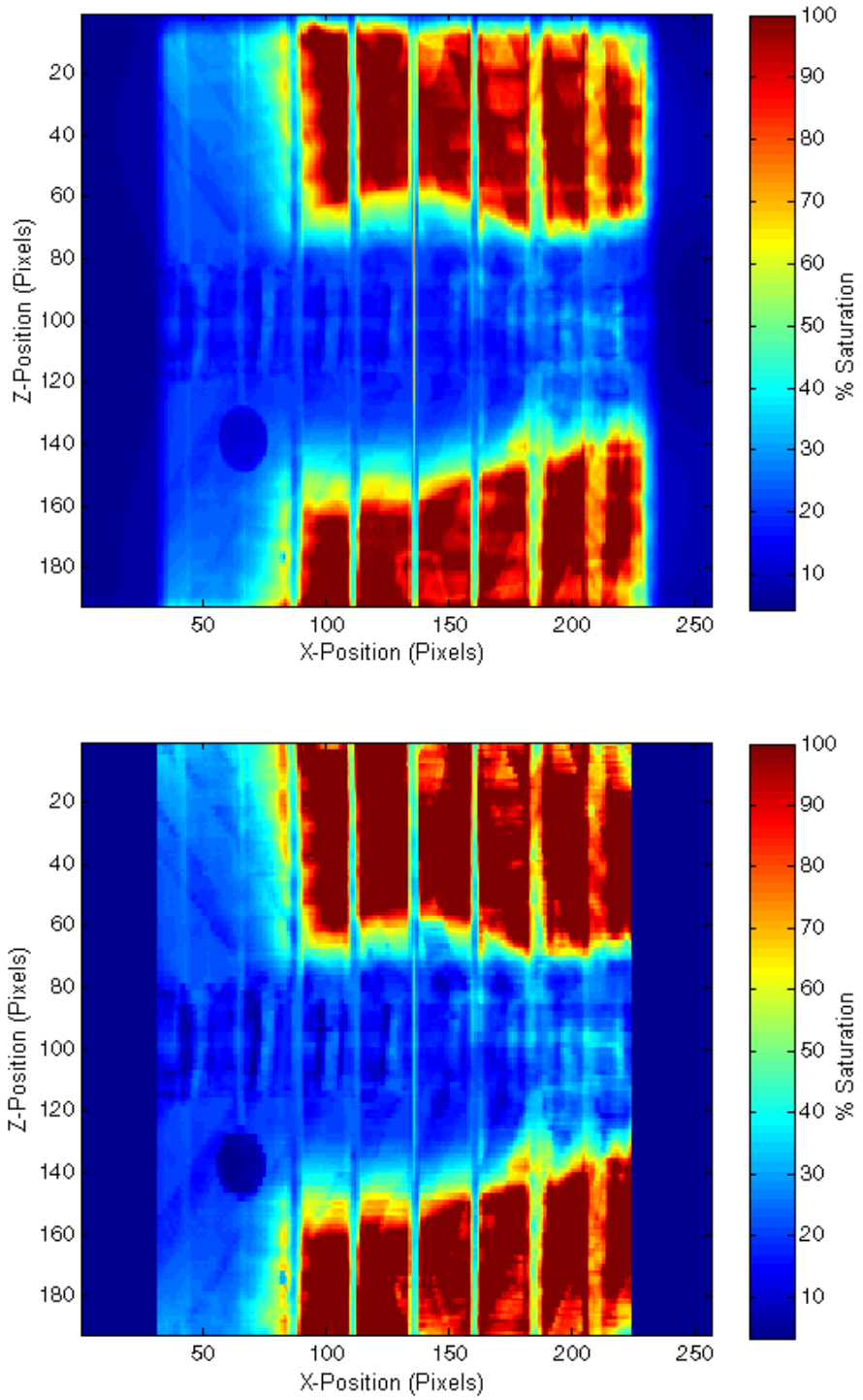


Figure 5.11: Anterior-posterior chest radiograph of the ART phantom taken at 120 kVp and 15.63 mAs on the OBI (top) and calculated by the DRR software (bottom).

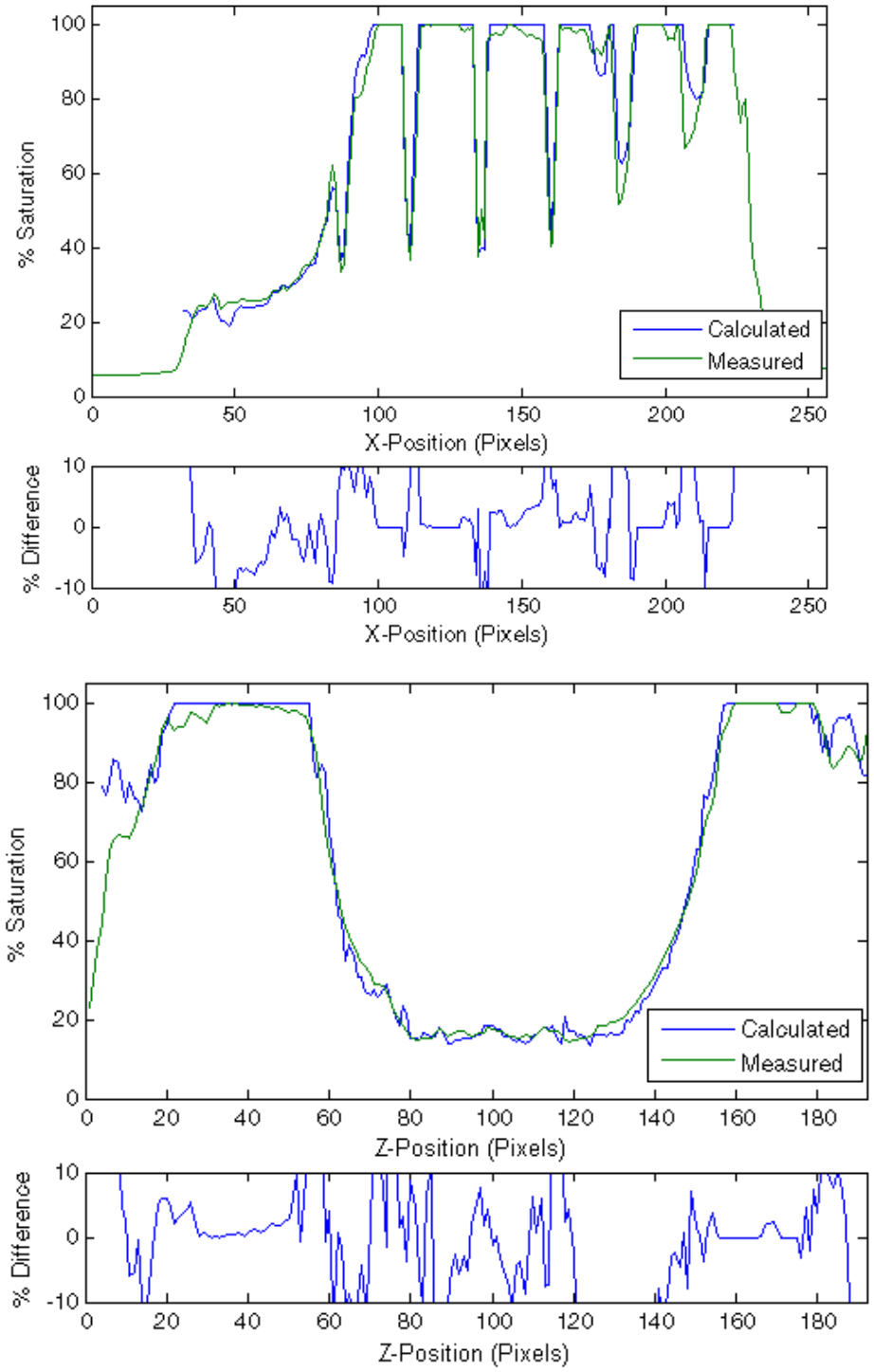


Figure 5.12: Profile comparison through the images shown in Figure 5.11 through the X-direction at Z = 40 (top) and Z-direction at X = 145.

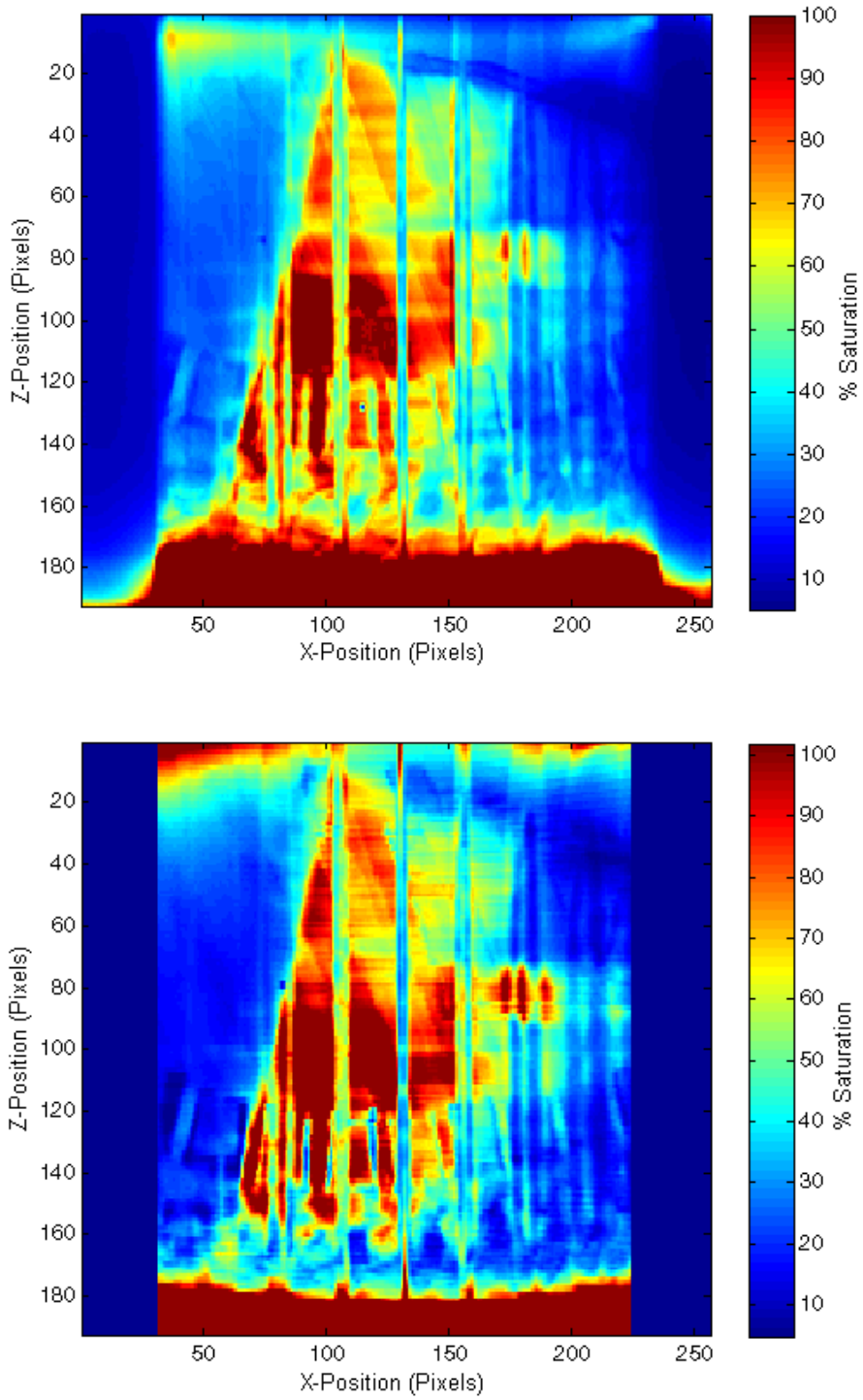


Figure 5.13: Lateral chest radiograph of the ART phantom taken at 120 kVp and 62.5 mAs on the OBI (top) and calculated by the DRR software (bottom).

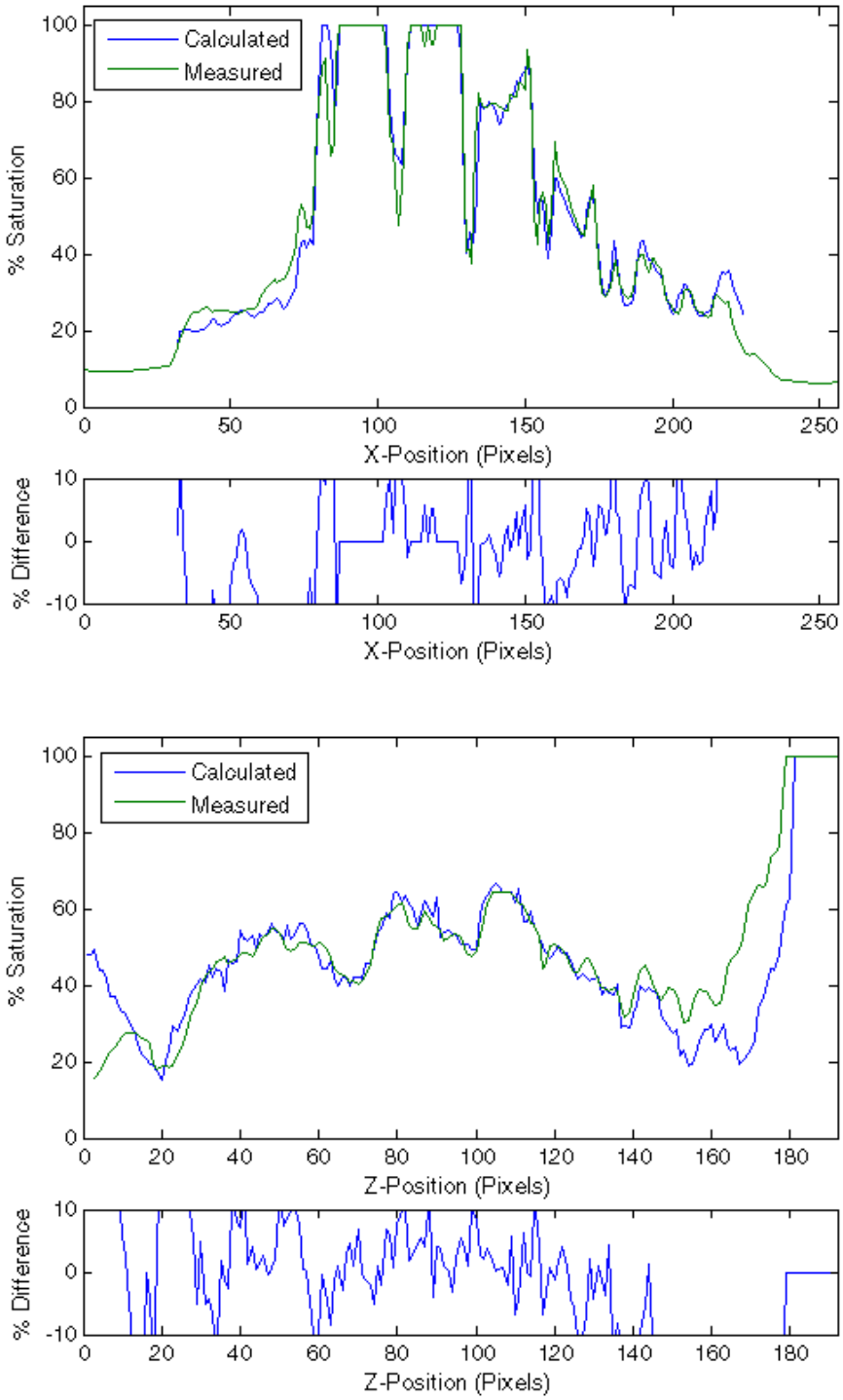


Figure 5.14: Profile comparison through the images shown in Figure 5.13 through the X-direction at Z = 100 (top) and Z-direction at X = 165 (bottom).

### 5.2.2 Patient Images

The results presented in the previous section showed that the DRR calculation software was able to generate images that closely agreed with images that were taken on the OBI for a variety of different exposure situations. Most importantly, the software was able to predict the saturated areas in the lung regions of the anthropomorphic phantom. Calculations were performed on two real patient datasets in order to verify that the same level of accuracy could be achieved in anatomical materials. Figure 5.15 (top) shows the chest radiograph taken of a patient during a course of IGRT. The image was acquired with 120 kVp and 8 mAs. The planning CT dataset for this patient was used in the DRR software to calculate the image shown in Figure 5.15 (bottom). The calculated image appears very similar to the image acquired of the patient on the OBI. Differences in the patient setup, as well as breathing motion, causes slight differences in the positioning of the two images. The lower region of the lung can be seen to be the most exposed, but does not achieve complete saturation.

The profiles through the chest radiograph are shown in Figure 5.16. The X-profile (bottom) was taken through the most saturated portion of the image at Z = 160. The detector is never fully saturated, with a maximum 57.3 $\%Sat$. The calculated values are within 5% of the measured values in the lung region of the image. Once again, a larger discrepancy is seen across the spinal region, with differences up to 60%. However, the large percent differences come from comparing measured values of around 3 $\%Sat$ to calculated values of around 1.5 $\%Sat$, a very small absolute difference. The Z-profile in Figure 5.16 (bottom), taken at X = 180, shows that the agreement throughout the entire lung region is generally within 10%, where the largest differences appeared in the areas intersecting tissues causing steep drops in the profile. The entire profile in the lung region had a mean absolute percent difference of 7.2%. Overall, the calculated image appears to be a fairly accurate representation of the saturation levels that were observed for the patient on the OBI.

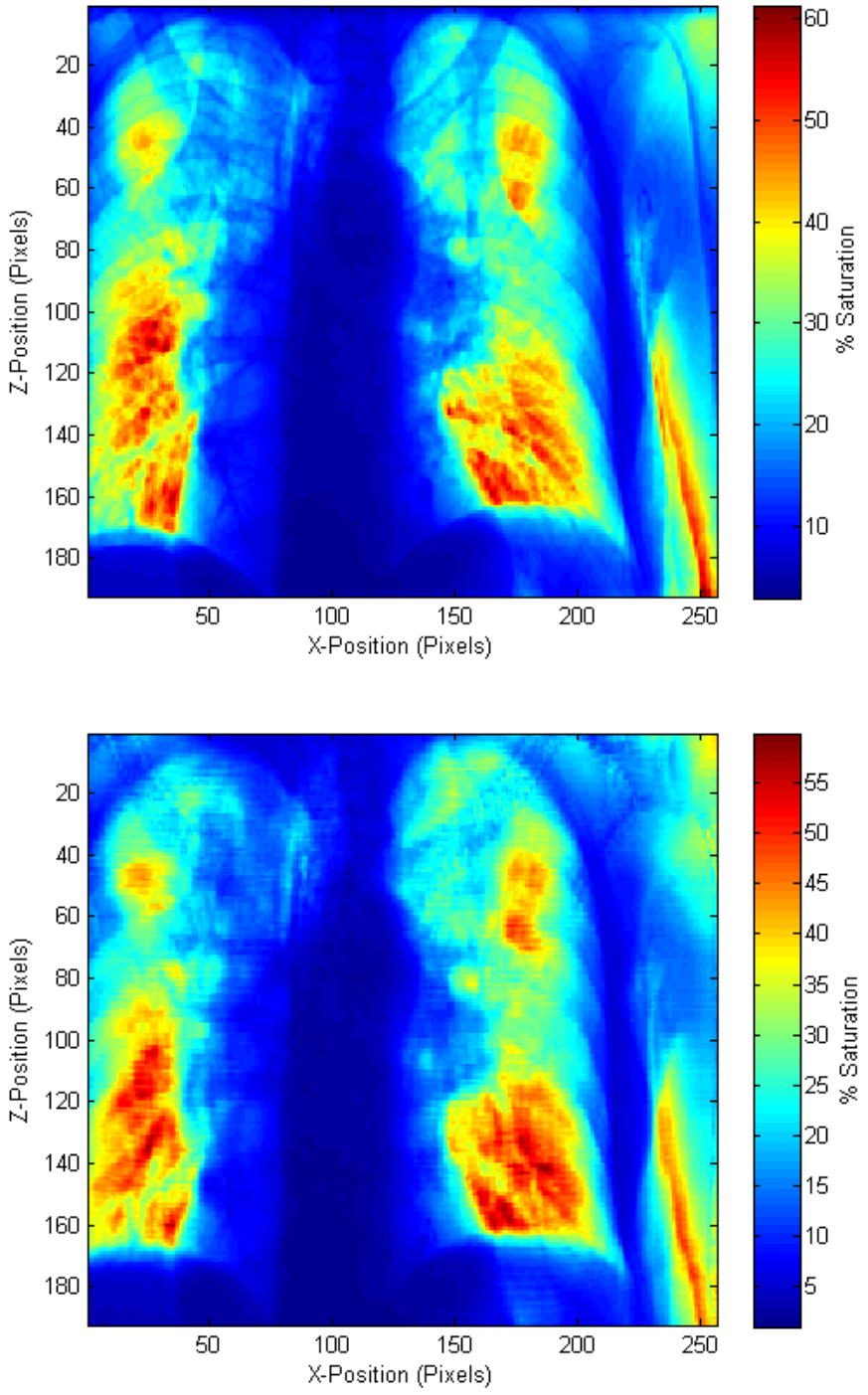


Figure 5.15: Chest radiograph of a patient acquired at 120 kVp and 8 mAs. The top image was taken of the patient during a fraction of IGRT and the bottom image was calculated by the DRR software.

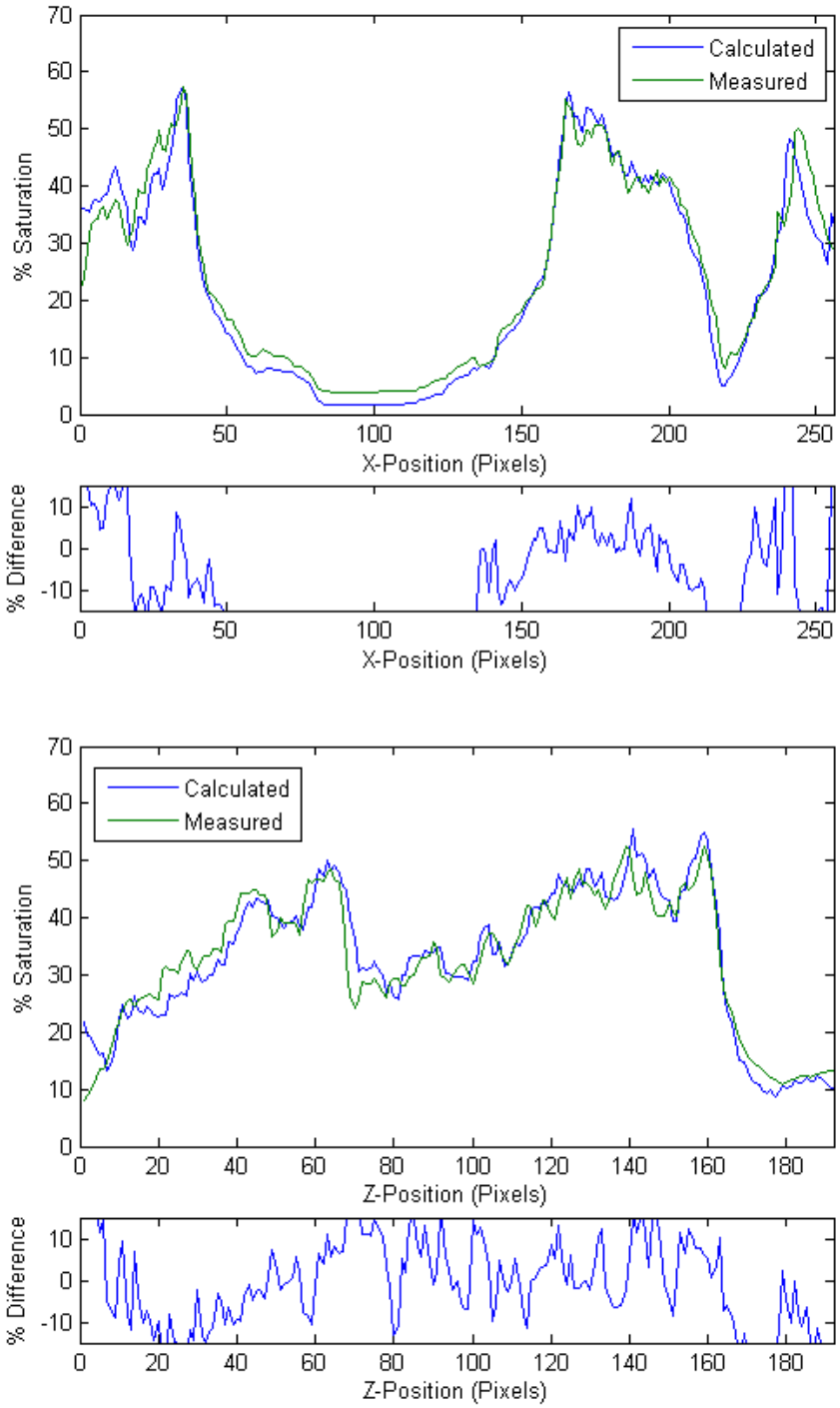


Figure 5.16: Profile comparison through the images shown in Figure 5.15 through the X-direction at Z = 160 (top) and Z-direction at X = 180 (bottom).

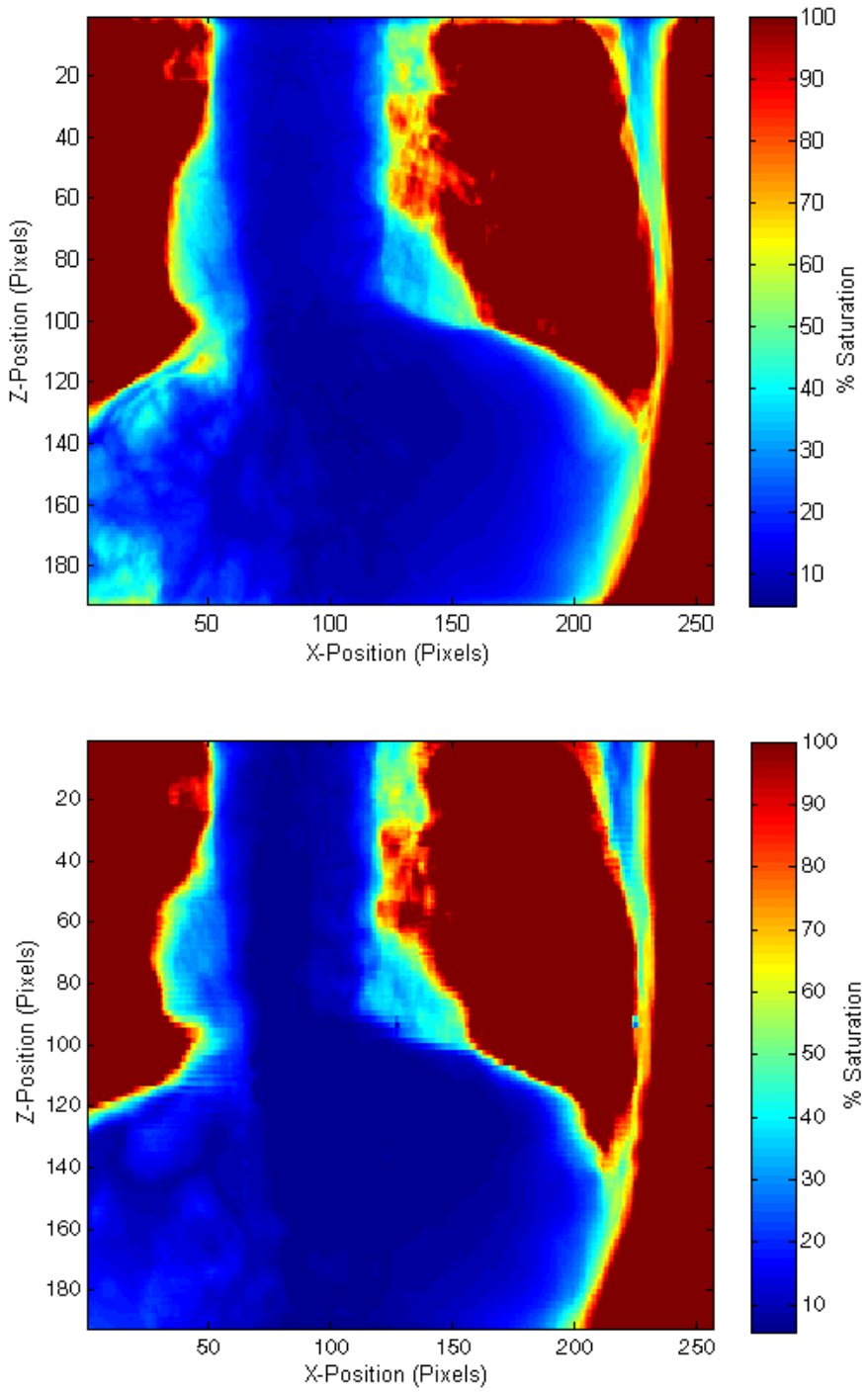


Figure 5.17: Esophagus radiograph of a patient acquired at 120 kVp and 8 mAs. The top image was taken of the patient during a fraction of IGRT and the bottom image was calculated by the DRR software.

Figure 5.17 shows another 120 kVp, 8 mAs chest radiograph of a different patient which results in significant detector saturation in the lung region. All anatomical data within the lung area has been completely removed from the image due to the saturation, possibly compromising the image matching process used in IGRT. The calculated image verifies the amount of saturation appearing in the measured image, except for small difference due to breathing motion. Figure 5.18 gives the calculated image in terms of the $\%Sat/\text{mAs}$. The regions that result in the greatest detector response do not exceed 27 $\%Sat/\text{mAs}$ and occur in the central regions of the lung. Therefore, reducing the exposure to 4 mAs would allow for the highest exposure while nearly completely eliminating saturation from the image (using Equation 3.1). This example shows how the DRR calculation program can be used to predict the optimal mAs before the patient is imaged in order to avoid detector saturation.

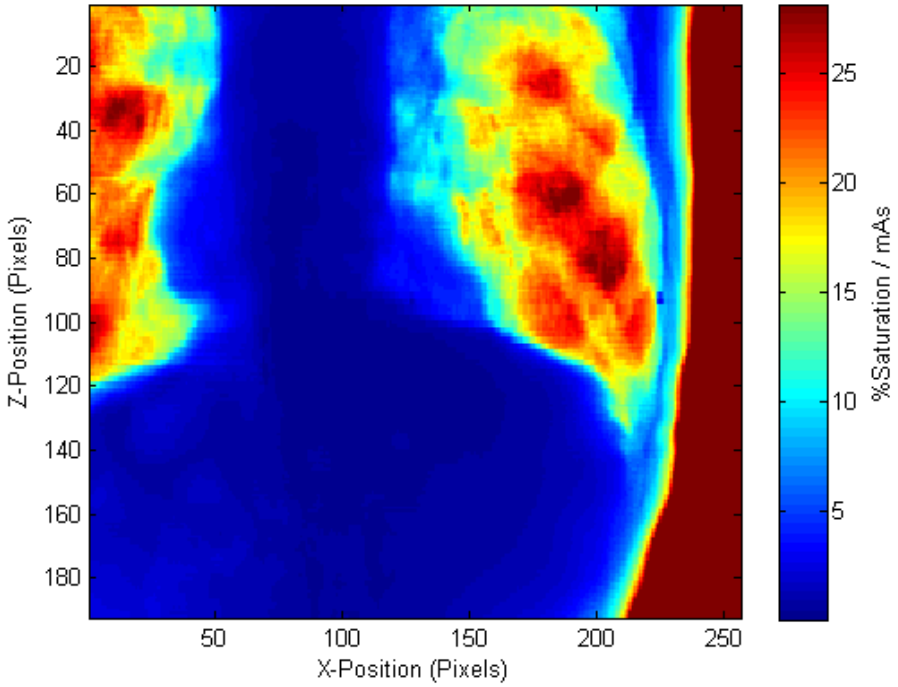


Figure 5.18: The total calculated $\%Sat/\text{mAs}$ of the patient shown in Figure 5.17.

## 5.3 Summary

Using the model data from Chapter 4, the ray tracing software was able to calculate the spectra that emerged from an imaged object, and hence the response of the OBI

detector to various exposures. The DRR calculations produced virtual radiographs for phantoms of varying degrees of complexity. The calculated images were able to accurately predict the regions of saturation that were produced when imaging the phantoms on the OBI. Patient data was used to test the software's ability to calculate the detector response for real IGRT cases, and were comparable to the results that were seen in the phantoms images. Therefore, the DRR calculation software has been shown to potentially be able to predict the optimal mAs required to eliminate saturation during patient imaging.

# Chapter 6

# Discussion

The results presented in Chapters 4 and 5 outlined the data used to generate the OBI system model and the comparisons of the calculations to values that were measured on the OBI. The following chapter discusses the results of the calculations while assessing the uncertainties of the model and their overall effects on the results. The DRR calculation software is evaluated for phantoms of varying degrees of complexity, as well as for patient images to determine the feasibility of the software's implementation clinically.

## 6.1 System Modelling

The comprehensive set of measurements presented in Chapter 4 were used in order to create a model of the OBI. The goal of this model was to be able to accurately characterize the system in terms of the x-ray tube output and the detector response to different qualities of beams. Measurements of the output and HVL of the incident x-rays were used to characterize the spectra that emerge from the x-ray tube. Multiple measurements of the HVL using two different methods verified the accuracy of the HVL emerging from the tube within a 1% uncertainty. The output of the tube was observed to fluctuate slightly between sets of measurements, so a mean value needed to be used in the calculations. Due to the variations around the mean, using the average value introduces a slight uncertainty into the calculations. Monitoring the output of 80 and 100 kVp beams over 14 weeks found average deviations from the mean of 1.5 and 1.6% respectively. The only way that this small uncertainty could be further reduced would be by measuring the systems output and performing the

DRR calculation immediately before the patient is imaged, which is infeasible in the clinical environment due to time constraints. The deviations in the detector response over the same period of time were each seen to be less than 1%, and would therefore have a minimal effect on the results.

The greatest uncertainty in the system characterization arises from the response model. As discussed in Section 4.2, the curve that was fit to the measured data to model the response of the detector deviated from the measured points by an average of 3.1%. The detector was clearly shown to have an energy dependence based on the characteristic curves (Figure 4.3), but uncertainties arose from using the HVL to describe this energy dependence. Several of the data points that were used to model the response had very similar HVLs but resulted in widely different responses from the detector. The difference was discussed to be a product of the energy response of the detector, where a lower kVp beam with a greater amount of filtration would result in a higher $\%Sat/\text{mR}$ than a higher kVp beam with less filtration and the same HVL. The response curve was a best fit line to all of the measured points and therefore the calculated values could potentially deviate from the actual response for a given exposure situation (by up to 7.2% in the model). Therefore, the response curve was able to predict the overall trend in the detector response based on the HVL, but to reduce the uncertainties a more robust model would be required. For example, hardening a single kVp beam would result in a smoother curve as it would eliminate the possibility of different spectra with the same HVL being present in the model. Therefore, an individual response curve could be produced for each kVp used in the generation of images to achieve a more accurate calculation of the detector response.

### 6.1.1 Scatter Model

The last component of the model was to design a way to approximate the scatter fraction resulting from any exposure situation. The scatter fraction was determined based on the imaging field size, kVp, and the object thickness (when centred at isocenter). The model data was based on the measured scatter fractions in the center of a field for thicknesses of Solid Water, and therefore the values needed to be adjusted to match the actual exposure situation. Using the Solid Water equivalent thickness of an imaged object to determine the scatter fraction was subject to errors due to the fact that the inherent scatter reduction due to the presence of air gaps is included

in the thickness component of the model. Therefore, phantoms with vastly different Solid Water equivalent thicknesses compared to their actual thicknesses would result in larger differences in the air gap and therefore the scatter reduction due to the air gap may be over or under predicted.

The scatter fraction calculations were tested on three different phantoms (Table 3.2). When compared to the measured scattered fractions, the calculated values were generally found to agree within the standard errors of the measured data (Table A.4). The calculated Solid Water equivalent thickness for Phantom2 was 8.6 cm, compared to its actual thickness of 17 cm. Using the Solid Water equivalent thickness, the model essentially assumed the presence of a 45.7 cm air gap, compared to the 41.5 cm air gap that was actually present during imaging. The air gap was discussed to be a major factor in scatter reduction. However, the differences between the measured and calculated scatter fractions were comparable to the other two phantoms which had equivalent thicknesses that were similar to the actual thicknesses. As shown in Figure 4.4, the difference in the scatter fraction between a 45.7 and 41.5 cm air gap is less than 1% for a 135 kVp with a $5 \times 5$ cm$^2$ field size, and would therefore have a small overall effect in this imaging situation.

Overall, the scatter fractions were generally calculated within the uncertainties of the measurements. Despite several larger percent differences between the measured and calculated values, the absolute differences would result in much less severe differences in the effects on the detector response to an exposure. For example, the calculated scatter fraction resulting from an 80 kVp $10 \times 10$ cm$^2$ field through Phantom2 (0.081) was 17.8% greater than the measured value ($0.068 \pm 0.009$). However, using the measured and calculated values for the scatter fraction in Equation 3.6 results in only a 1.3% difference in the total detector response. Therefore, despite the uncertainties in the empirical scatter model, the data can be used to approximate the scatter fractions and provide a reasonable estimate of the effects of the scatter on the total exposure.

## 6.2 Phantom Studies

Two phases of phantom studies were performed in order to test the accuracy of the DRR calculation compared to measured values. The first tests involved the comparisons of the outputs, HVLs, and detector responses between point measurements in small ROIs in the measured and calculated images. The purpose of the point

measurements was to determine the accuracy of the attenuation calculation in the DRR software compared to ideal measurements without uncertainties resulting from spatial resolution and positional differences. The results of these measurements were discussed in Section 5.1.3, and generally had very good agreement between the measured and calculated outputs and HVLs, with many of the points being calculated to within 1% of the measured values.

Differences in the output can be attributed to the uncertainties in the open field output discussed above. There also exists uncertainties in the calculation of the attenuation of the beam, where the attenuation coefficients were converted from the CT values, which also results in the differences in the calculated HVLs. The NIST XCOM database, which was used to determine the attenuation coefficients from the material properties of the phantom, gives a maximum 10% error in the calculated attenuation coefficients [30, 40] . Additionally, only two high HU data points were used in the conversion curve (Figure 5.2) which causes additional uncertainties in the calculated linear attenuation coefficients. The effects of these uncertainties can clearly be seen in the calculations of the attenuation with the addition of PMMA, which increased the differences in the measured and calculated values by more than 6% when compared to the phantoms which were composed of only Solid Water and polystyrene.

The results presented in Tables 5.5 to 5.7 showed a wide range of differences in the measured and calculated detector responses. Referring to equation 3.6, it can be seen that differences in the attenuation calculations affect the response calculation in various ways. For example, a 5% difference in the calculated mR/mAs will result in a 5% difference in the response, where the same difference in the calculated HVL may have less or more of an effect on the response depending on its location on the response curve. Additionally, the uncertainties on the response curve discussed in Section 6.1 can account for the differences in the total calculated $\%Sat$/mAs when the output and HVL were calculated to be nearly equivalent to the measured values for the same exposures. The addition of scatter did not widely effect the differences in the response due to the reasons discussed in Section 6.1.1. Overall, the calculated responses were generally within 5 to 10% of the measured values, which is reasonable considering the uncertainties associated with the system output, attenuation calculation, scatter fraction, and detector response model discussed above. Again, as discussed in Section 5.1.3, the small absolute differences in the measured and calculated responses ($<$0.3 $\%Sat$/mAs) do not inhibit the software's ultimate goal of predicting regions of

detector saturation.

The second phase of the phantom studies involved producing full field images in order to observe the contrast and spatial resolution of the images. Phantoms were used to test a wider range of materials than were used in the previous measurements while reducing the uncertainties associated with motion and misalignment. Profiles were produced to visualize the differences in the measured and calculated detector responses across the beam as it is attenuated by various types of materials. The full field profiles in Figure 5.5 show how the intensity of the measured beam varies with the off-axis positioning. The intensity of the beam profile varies with distance from the central axis due to the divergence of the beam, as well as the Heel effect which attenuates and hardens the beam on the anode side of the x-ray tube. The variations of the intensity and the spectrum resulted in small (<5%) differences in the actual detector response that were not modelled in the calculation. Off-axis effects could be accounted for using a flood-field correction by normalizing the calculated values by a measured full field open image. Applying a field correction would therefore scale the calculated values to represent the machine specific off-axis effects that were not included in the system model.

Despite the increasing complexity of the phantom images analysed, the calculated values generally agreed very well with the values measured on the OBI with less than 5% differences in the more homogeneous regions. The phantom calculations were subject to the same uncertainties associated with the point measurements discussed above, as well as additional uncertainties in the geometries of the image. Efforts were taken to position the phantoms for OBI imaging as they were during CT imaging, but small (mm) differences are practically unavoidable. Despite the differences, the measured and calculated profiles spatially agreed very well, with peaks in the response generally appearing within 2 pixels (3.2 mm) of each other. As a result of the alignment, steep gradients in the detector response were the cause of the greatest percent differences in the measured and calculated values.

The importance of the addition of scatter to the images was displayed in Figures 5.5 and 5.8. The scatter fractions obtained from the empirical scatter model accurately increased the level of detector saturation in the calculated images to the levels that were observed on the OBI. While the scatter fractions in the lung regions are small (<0.1), it can be seen how the scatter can potentially cause the detector to saturate in areas that would not become saturated due to the primary radiation only, particularly in the periphery of the lung region. With the inclusion of scatter, the

DRR calculation was able to accurately determine the areas in the images that would become saturated. The calculated saturation values were shown to deviate the most from the actual values in denser regions and areas near the field edges, for the reasons discussed previously. While the presence of the bony anatomy is critical for image matching, the profiles show a significantly lower response in these regions compared to the lung regions. Therefore, as the detector is highly unlikely to become saturated in the dense regions, the ability of the software to determine the optimal mAs for an exposure to prevent saturation is not affected by these uncertainties. Overall, the calculated images accurately represented the images that were taken on the OBI and show that the DRR software can be used to predict the detector saturation in complex phantoms.

## 6.3 Clinical Data

While the DRR calculation software has been shown to be able to predict areas of saturation in OBI images of an anthropomorphic phantom, human anatomy is obviously composed of different materials. Additionally, patient anatomy is more complex and is subject to motion and positioning deviations, particularly breathing motion in the lungs, which were not introduced in the phantom image. The purpose of the clinical data presented in Section 5.2.2 was to determine the feasibility of the software's use on real patients.

The patient radiographs shown in Figure 5.15 were used to determine if the accuracy in the calculations shown in the phantom images could be reproduced in clinical images. The results of the patient image were comparable to the results generated in the phantom images. Overall, the calculated saturation values in the lung regions, the areas of interest in a chest radiograph, agreed with a mean absolute percent difference of 7.2%. Again, a large discrepancy was seen in the attenuation in the bony anatomy, and a major source of the difference between the measured and calculated values appears to arise from the alignment of the two images. The motion and alignment in the images causes the pixel-to-pixel comparison to have larger differences in high gradient regions. The higher areas of detector saturation were generally calculated to be at the same level that were observed on the OBI image, but displaced by several pixels in the profile.

The DRR calculation software was designed to predict areas of saturation in OBI radiographs, not to generate exact spatially matched images, a task which is especially

difficult to achieve when considering breathing motion. The radiographs presented in Figure 5.17 show how alignment and motion do not inhibit the ability of the software. Although obvious differences appear in the shape and position of the lungs in the two images, the calculated image clearly shows that the entirety of the lung region becomes saturated with the mAs that was used to acquire the OBI image. The $\%Sat$/mAs can simply be used to determine a more optimal mAs for image acquisition which would result in the lungs appearing less saturated, regardless of positioning and motion. Therefore, despite the uncertainties, the DRR software has been shown to be able to accurately predict areas of detector saturation in patient images, and the concept could be advantageous in reducing the exposure to patients during IGRT.

## 6.4 Summary

Overall, the model and DRR software were observed to generate accurate predictions of the level of detector saturation from images with varying degrees of complexity. Peaks in the detector response, the most important areas when predicting detector saturation, were accurately calculated. The largest differences between measured and calculated images occurred in dense, low exposure regions as well as areas affected by motion and alignment. These differences have been discussed to have minimal impact on the software's ability to predict saturation in the images.

# Chapter 7

# Conclusions & Future Work

The purpose of this thesis was to outline the development of a software based automatic exposure control to compensate for a lack of such a device on the Varian on-board imaging system. The software based AEC could be used to predict the level of detector saturation that would result from imaging during radiation therapy. In doing so, the optimal mAs could be determined before treatment begins, thus preventing the need for multiple unnecessary exposures. The AEC was developed by using CT datasets to perform a DRR ray trace in combination with an OBI system model to calculate the percentage of detector saturation per mAs for any exposure situation.

Overall, the DRR calculation software was able to predict the regions of detector saturation for images of complex phantoms and real patients. The calculations differed the most from measured data in areas of high attenuation and near the field edges. Alignment and motion during imaging added an additional spatial uncertainty to the calculations. In the absence of positioning errors, the calculated images were seen to align very well with the measured images, with steep gradients in the exposure generally appearing within several pixels. The spatial resolution of the calculated images could be improved by generating higher resolution (small pixels) images, at the cost of computation time. Slight misalignment and motion errors are unavoidable in patient imaging but were shown to have no effect on the software's ability to determine the overall saturation in the images.

## 7.1 Future Work

While it is not within the scope of this thesis to conclude whether the software that was developed could be used clinically, it is clear based on the presented results that some improvements could be made. The level of accuracy required to implement the software for clinical use is left to be determined. Additional testing on patient data would at least be required to build confidence in the software before implementing it to calculate the exposure factors required for patients' treatments. Based on the shortcomings of the results, the software could benefit from addition improvements to the attenuation calculations of the x-rays, especially in high HU material, a flood-field correction to model off-axis effects, as well as an improved detector response curve which could minimize the uncertainty in the HVL to detector response calculation. Additionally, where time and usability are important factors in the clinical environment, optimization of the software would be required before implementation.

Without an AEC on the OBI system, IGRT is subject to uncertainties in the exposure that may result in detector saturation and compromise the image matching used to align patients for treatment. The software that was developed was shown to be a viable alternative method of regulating radiographic exposures. It is reasonable to state that an accurate DRR calculation and robust system model can be used to determine the optimal mAs that would be required on a patient specific basis. Clinical implementation of such a system would result in improved confidence in on-board imaging while potentially reducing patient dose and decreasing overall treatment times by eliminating the need for multiple exposures in the absence of a physical AEC.

# Appendix A

# Additional Information

The data presented in Chapters 4 and 5 outlined the the measurements that were performed to produce and verify the x-ray system model. The following tables present the comprehensive lists of measurements that were used to characterize the scatter fraction in on-board imaging (Tables A.1 and A.2). The list of measurements that were performed to test the accuracy of the SpekCalc software in determining the HVLs of hardened beams (Table A.3), as well as the comparison of measured and calculated scatter fractions for several phantoms (A.4) are also given. All of the measured data are presented with uncertainties represented by the standard errors of the measurements.

Table A.1: List of measured scatter fractions (%) for field sizes from 4 × 4 cm$^2$ to 15 × 15 cm$^2$ for various kVp and thicknesses of Solid Water.

| | 4 × 4 cm$^2$ | 7 × 7 cm$^2$ | 10 × 10 cm$^2$ | 15 × 15 cm$^2$ |
|---|---|---|---|---|
| 80 kVp | | | | |
| 5 cm | 0.73 ± 0.58 | 4.85 ± 0.56 | 6.52 ± 0.50 | 8.19 ± 0.32 |
| 10 cm | 1.73 ± 0.57 | 6.79 ± 0.51 | 9.25 ± 0.53 | 12.1 ± 0.5 |
| 15 cm | 1.87 ± 0.43 | 7.8 ± 0.5 | 11.2 ± 0.4 | 15.9 ± 0.4 |
| 20 cm | 3.2 ± 2.1 | 9.5 ± 0.3 | 14.2 ± 0.4 | 20.4 ± 0.2 |
| 100 kVp | | | | |
| 5 cm | 0.71 ± 0.78 | 4.9 ± 0.9 | 7.1 ± 0.9 | 8.3 ± 0.8 |
| 10 cm | 1.6 ± 1.0 | 7.3 ± 1.1 | 9.7 ± 1.3 | 12.0 ± 1.6 |
| 15 cm | 2.51 ± 0.84 | 8.92 ± 0.89 | 12.3 ± 1.0 | 17.1 ± 1.3 |
| 20 cm | 3.34 ± 0.41 | 9.36 ± 0.49 | 14.3 ± 0.6 | 21.2 ± 0.9 |
| 110 kVp | | | | |
| 5 cm | 0.81 ± 0.95 | 4.7 ± 1.4 | 6.8 ± 1.5 | 8.4 ± 1.4 |
| 10 cm | 0.64 ± 0.74 | 5.33 ± 0.58 | 8.03 ± 0.66 | 12.5 ± 1.0 |
| 15 cm | 1.7 ± 1.1 | 7.9 ± 1.3 | 11.6 ± 1.5 | 16.4 ± 1.9 |
| 20 cm | 3.1 ± 1.2 | 9.2 ± 1.5 | 14.4 ± 1.6 | 21.3 ± 2.3 |
| 120 kVp | | | | |
| 5 cm | 0.45 ± 0.35 | 5.2 ± 1.1 | 7.4 ± 1.2 | 8.5 ± 1.1 |
| 10 cm | 1.4 ± 1.2 | 5.3 ± 1.5 | 8.1 ± 1.6 | 12.3 ± 2.1 |
| 15 cm | 1.7 ± 1.2 | 8.5 ± 1.3 | 12.2 ± 1.5 | 16.9 ± 0.6 |
| 20 cm | 4.3 ± 1.3 | 10.5 ± 1.3 | 15.6 ± 1.4 | 21.9 ± 1.4 |
| 135 kVp | | | | |
| 5 cm | 0.48 ± 0.45 | 4.1 ± 1.7 | 6.2 ± 1.7 | 8.9 ± 2.0 |
| 10 cm | 2.1 ± 1.0 | 5.9 ± 1.0 | 8.7 ± 1.1 | 13.6 ± 1.2 |
| 15 cm | 1.7 ± 1.7 | 7.2 ± 2.0 | 10.7 ± 2.3 | 17.4 ± 2.9 |
| 20 cm | 4.6 ± 2.2 | 10.9 ± 2.5 | 16.8 ± 2.1 | 22.1 ± 3.4 |

Table A.2: List of measured scatter fractions (%) for field sizes from 20 × 20 cm$^2$ to 30 × 30 cm$^2$ for various kVp and thicknesses of Solid Water.

| | 20 × 20 cm$^2$ | 25 × 25 cm$^2$ | 30 × 30 cm$^2$ |
|---|---|---|---|
| 80 kVp | | | |
| 5 cm | 10.8 ± 2.2 | 11.6 ± 0.3 | 12.8 ± 1.4 |
| 10 cm | 14.6 ± 2.0 | 17.3 ± 0.4 | 17.7 ± 0.7 |
| 15 cm | 20.1 ± 1.8 | 23.3 ± 0.5 | 25.8 ± 1.7 |
| 20 cm | 26.1 ± 0.4 | 30.2 ± 0.2 | 33.3 ± 0.4 |
| 100 kVp | | | |
| 5 cm | 10.2 ± 0.7 | 11.6 ± 1.0 | 12.3 ± 0.8 |
| 10 cm | 14.2 ± 1.7 | 17.6 ± 2.0 | 20.5 ± 0.8 |
| 15 cm | 22.2 ± 1.4 | 25.1 ± 1.7 | 29.8 ± 1.1 |
| 20 cm | 26.9 ± 1.5 | 31.9 ± 1.5 | 36.1 ± 1.0 |
| 110 kVp | | | |
| 5 cm | 10.0 ± 0.6 | 12.2 ± 1.5 | 12.6 ± 0.6 |
| 10 cm | 15.6 ± 0.9 | 18.4 ± 1.3 | 20.2 ± 1.3 |
| 15 cm | 23.4 ± 1.0 | 24.3 ± 3.1 | 29.2 ± 1.4 |
| 20 cm | 27.2 ± 3.4 | 32.4 ± 3.4 | 36.9 ± 2.1 |
| 120 kVp | | | |
| 5 cm | 11.2 ± 0.6 | 12.4 ± 1.3 | 13.8 ± 0.9 |
| 10 cm | 16.8 ± 1.1 | 19.9 ± 1.3 | 21.8 ± 1.1 |
| 15 cm | 22.8 ± 0.6 | 27.3 ± 0.5 | 29.2 ± 0.8 |
| 20 cm | 30.7 ± 1.3 | 34.6 ± 0.9 | 38.7 ± 1.8 |
| 135 kVp | | | |
| 5 cm | 11.1 ± 1.8 | 12.3 ± 2.0 | 14.3 ± 0.9 |
| 10 cm | 17.0 ± 1.4 | 20.0 ± 1.5 | 21.9 ± 2.1 |
| 15 cm | 23.6 ± 0.7 | 28.2 ± 1.7 | 29.8 ± 2.2 |
| 20 cm | 31.7 ± 3.1 | 35.3 ± 2.5 | 38.7 ± 1.2 |

Table A.3: Comparison of the HVLs (mmAl) measured for hardened beams on the OBI to the values calculated by the SpekCalc software.

| Filtration | kVp | Measured (mmAl) | SpekCalc | % Difference |
|---|---|---|---|---|
| 5 cm water | 65 | 3.80 ± 0.01 | 3.88 | 2.11 |
| | 80 | 4.73 ± 0.02 | 4.75 | 0.42 |
| | 100 | 5.91 ± 0.01 | 5.87 | -0.68 |
| | 120 | 6.88 ± 0.02 | 6.86 | -0.29 |
| 5 cm water, 1 mm Al | 65 | 4.07 ± 0.01 | 4.14 | 1.72 |
| | 80 | 5.06 ± 0.01 | 5.07 | 0.20 |
| | 100 | 6.28 ± 0.01 | 6.25 | -0.48 |
| | 120 | 7.28 ± 0.01 | 7.26 | -0.27 |
| 5 cm water, 3 mm Al | 65 | 4.56 ± 0.01 | 4.59 | 0.66 |
| | 80 | 5.68 ± 0.03 | 5.63 | -0.88 |
| | 100 | 6.98 ± 0.02 | 6.89 | -1.29 |
| | 120 | 7.99 ± 0.02 | 7.92 | -0.88 |
| 7.5 cm water | 65 | 4.20 ± 0.02 | 4.33 | 3.09 |
| | 80 | 5.24 ± 0.02 | 5.32 | 1.53 |
| | 100 | 6.51 ± 0.03 | 6.56 | 0.77 |
| | 120 | 7.51 ± 0.02 | 7.60 | 1.20 |
| 7.5 cm water, 1 mm Al | 65 | 4.42 ± 0.01 | 4.55 | 2.94 |
| | 80 | 5.52 ± 0.02 | 5.59 | 1.27 |
| | 100 | 6.83 ± 0.01 | 6.86 | 0.44 |
| | 120 | 7.86 ± 0.02 | 7.92 | 0.76 |
| 7.5 cm water, 3 mm Al | 65 | 4.76 ± 0.02 | 4.93 | 3.57 |
| | 80 | 5.99 ± 0.02 | 6.06 | 1.17 |
| | 100 | 7.35 ± 0.01 | 7.39 | 0.54 |
| | 120 | 8.40 ± 0.01 | 8.46 | 0.71 |
| 1 mm Al | 65 | 2.91 ± 0.01 | 3.05 | 4.81 |
| | 80 | 3.55 ± 0.02 | 3.70 | 4.23 |
| | 100 | 4.52 ± 0.02 | 4.58 | 1.33 |
| | 120 | 5.40 ± 0.01 | 5.42 | 0.37 |
| 3 mm Al | 65 | 3.62 ± 0.01 | 3.72 | 2.76 |
| | 80 | 4.48 ± 0.01 | 4.52 | 0.89 |
| | 100 | 5.58 ± 0.02 | 5.56 | -0.36 |
| | 120 | 6.51 ± 0.01 | 6.49 | -0.31 |
| 5 mm Al | 65 | 4.19 ± 0.02 | 4.24 | 1.19 |
| | 80 | 5.18 ± 0.02 | 5.17 | -0.19 |
| | 100 | 6.40 ± 0.01 | 6.32 | -1.25 |
| | 120 | 7.36 ± 0.01 | 7.28 | -1.09 |
| | | | Mean(%): | 0.87 |

Table A.4: Measured and calculated scatter fraction for various combinations of materials, field sizes, and kVp. Phantom compositions are listed in Tabel 3.2.

| Phantom & Field Size | kVp | Measured SF | Calculated SF | % Difference |
|---|---|---|---|---|
| Phantom1 | 80 | 9.63 ± 0.35 | 10.2 | 5.88 |
| 10 × 10 $cm^2$ | 100 | 11.6 ± 1.03 | 10.8 | -6.94 |
| | 120 | 9.83 ± 1.66 | 10.6 | 8.29 |
| Phantom1 | 80 | 14.8 ± 0.3 | 13.9 | -5.98 |
| 15 × 15 $cm^2$ | 100 | 15.7 ± 1.2 | 14.3 | -8.93 |
| | 120 | 16.4 ± 1.1 | 14.6 | -11.2 |
| Phantom1 | 80 | 21.1 ± 0.3 | 20.1 | -4.88 |
| 25 × 25 $cm^2$ | 100 | 23.9 ± 0.9 | 21.0 | -12.3 |
| | 120 | 24.3 ± 1.3 | 22.9 | -5.91 |
| Phantom2 | 80 | 6.83 ± 0.89 | 8.05 | 17.8 |
| 10 × 10 $cm^2$ | 100 | 7.77 ± 1.33 | 8.70 | 12.1 |
| | 120 | 9.18 ± 1.29 | 8.37 | -8.83 |
| Phantom2 | 80 | 10.2 ± 0.9 | 10.6 | 4.40 |
| 15 × 15 $cm^2$ | 100 | 11.0 ± 1.6 | 10.7 | -2.52 |
| | 120 | 11.7 ± 1.3 | 10.9 | -6.3 |
| Phantom2 | 80 | 14.8 ± 1.2 | 15.1 | 1.87 |
| 25 × 25 $cm^2$ | 100 | 17.8 ± 1.2 | 15.5 | -12.9 |
| | 120 | 18.9 ± 1.6 | 16.9 | -10.6 |
| Phantom3 | 80 | 6.84 ± 0.25 | 7.1 | 3.75 |
| 10 × 10 $cm^2$ | 100 | 6.47 ± 1.54 | 7.17 | 10.8 |
| | 120 | 6.45 ± 0.48 | 7.32 | 13.4 |
| Phantom3 | 80 | 9.53 ± 0.41 | 9.7 | 1.77 |
| 15 × 15 $cm^2$ | 100 | 9.17 ± 1.67 | 9.17 | -0.02 |
| | 120 | 9.56 ± 0.50 | 9.36 | -2.04 |
| Phantom3 | 80 | 13.97 ± 1.2 | 15.1 | 8.37 |
| 25 × 25 $cm^2$ | 100 | 14.36 ± 1.0 | 13.1 | -9.0 |
| | 120 | 14.1 ± 0.6 | 14.3 | 1.09 |

# Bibliography

[1] E. B. Podgorsak, *Radiation Physics for Medical Physicists*. Hidelberg: Springer, 2nd ed., 2010.

[2] P. Mayles, A. Nahum, and J. Rosenwald, eds., *Handbook of Radiotherapy Physics: Theory and Practice*. New York: Taylor & Francis, 2007.

[3] W. J. Meredith, "40 Years of Development in Radiotherapy," *Phys. Med. Biol.*, vol. 29, pp. 115–120, 1984.

[4] H. E. Johns, L. M. Bates, and T. A. Watson, "1000 Curie cobalt units for radiation therapy," *British Journal of Radiology*, vol. 25, pp. 296–302, 1952.

[5] D. Green and R. Errington, "Design of a cobalt 60 beam therapy unit," *British Journal of Radiology*, vol. 25, pp. 309–313, 1952.

[6] M. Joiner and A. van der Kogel, eds., *Basic Clinical Radiobiology*. London: Hodder Arnold, 4th ed., 2009.

[7] S. Webb, *The Physics of Conformal Radiotherapy: Advances in Technology*. Bristol: Institute of Physics Publishing, 1997.

[8] W. R. Hendee, G. S. Ibbott, and E. G. Hendee, *Radiation Therapy Physics*. Hoboken: John Wiley & Sons, 3rd ed., 2005.

[9] S. H. Levitt, J. A. Purdy, C. A. Perez, and P. Poortmans, eds., *Technical Basis of Radiation Therapy*. Hidelberg: Springer, 5th ed., 2012.

[10] H. Thames and T. Schultheiss, "Can modest escalations of dose be detected as increased tumor control?," *Int. J. Radiat. Oncol. Biol. Phys.*, vol. 22, pp. 241–246, 1992.

[11] C. M. van Rij, W. D. Oughlane-Heemsbergen, A. H. Ackerstaff, E. A. Lamers, A. J. M. Balm, and C. R. N. Rasch, "Parotid gland sparing IMRT for head and neck cancer improves xerostomia related quality of life.," *Radiat. Oncol.*, vol. 3, pp. 41–50, 2008.

[12] K. Otto, "Volumetric modulated arc therapy: IMRT in a single gantry arc," *Med. Phys.*, vol. 35, pp. 310–317, 2008.

[13] D. Palma, E. Vollans, K. James, S. Nakano, V. Moiseenko, R. Shaffer, M. McKenzie, J. Morris, and K. Otto, "Volumetric modulated arc therapy for delivery of prostate radiotherapy: comparison with intensity-modulated radiotherapy and three-dimensional conformal radiotherapy.," *Int. J. Radiat. Oncol. Biol. Phys.*, vol. 72, pp. 996–1001, 2008.

[14] J. L. Meyer, B. Kavanagh, J. Purdy, and R. Timmerman, eds., *Frontiers of Radiation Therapy and Oncology IMRT IGRT SBRT: Advances in the Treatment Planning and Delivery of Radiotherapy.* Basel: Karger, 2007.

[15] J. Michalski, M. Graham, and W. Bosch, "Prospective clinical evaluation of an electronic portal imaging device," *Int. J. Radiat. Oncol. Biol. Phys.*, vol. 34, pp. 943–951, 1996.

[16] G. C. Bentel, *Patient Positioning and Immobilization in Radiation Oncology.* New York: McGraw-Hill, 1999.

[17] T. S. Hong, W. A. Tomé, R. J. Chappell, P. Chinnaiyan, M. P. Mehta, and P. M. Harari, "The impact of daily setup variations on head-and-neck intensity-modulated radiation therapy.," *Int. J. Radiat. Oncol. Biol. Phys.*, vol. 61, pp. 779–788, 2005.

[18] T. Fox, C. Huntzinger, P. Johnstone, T. Ogunleye, and E. Elder, "Performance evaluation of an automated image registration algorithm using an integrated kilovoltage imaging and guidance system.," *Journal of Applied Clinical Medical Physics*, vol. 7, pp. 97–104, 2006.

[19] M. J. Murphy, J. Balter, S. Balter, J. a. BenComo, I. J. Das, S. B. Jiang, C.-M. Ma, G. H. Olivera, R. F. Rodebaugh, K. J. Ruchala, H. Shirato, and F.-F. Yin, "The management of imaging dose during image-guided radiotherapy: Report of the AAPM Task Group 75," *Med. Phys.*, vol. 34, pp. 4041–4063, 2007.

[20] E. J. Hall and A. J. Giaccia, *Radiobiology for the Radiologist*. Philadelphia: Lippincott Williams & Wilkins, 6th ed., 2006.

[21] J. R. Perks, J. Lehmann, A. M. Chen, C. C. Yang, R. L. Stern, and J. a. Purdy, "Comparison of peripheral dose from image-guided radiation therapy (IGRT) using kV cone beam CT to intensity-modulated radiation therapy (IMRT).," *Radiother. Oncol.*, vol. 89, pp. 304–310, 2008.

[22] J. Bushberg, A. Seibery, E. Leidholdt, and J. Boone, *The Essential Physics of Medical Imaging*. Philadelphia: Lippincott Williams & Wilkins, 3rd ed., 2012.

[23] H. E. Johns and J. R. Cunningham, *The Physics of Radiology*. Springfiled: Charles C Thomas, 4th ed., 1983.

[24] J. Beutel, H. L. Kundel, and R. L. Van Metter, eds., *Handbook of Medical Imaging: Volume 1. Physics and Psychophysics*. Bellingham: SPIE, 2000.

[25] H. Aichinger, J. Dierker, S. Joite-Barfuß, and M. Säbel, *Radiation Exposure and Image Quality in X-Ray Diagnostic Radiology*. Berlin: Springer-Verlag, 2004.

[26] U. Neitzel, "Grids or air gaps for scatter reduction in digital radiography: A model calculation," *Med. Phys.*, vol. 19, pp. 475–481, 1992.

[27] "Varian G-242," tech. rep., Varian Medical Systems, Salt Lake City, UT, 2007.

[28] "PaxScan 4030CB," tech. rep., Varian Medical Systems, Salt Lake City, UT, 2012.

[29] "Unfors Xi User's Manual," tech. rep., Unfors Instruments, Billdal, Sweden, 2007.

[30] C. S. Moore, G. P. Liney, a. W. Beavis, and J. R. Saunderson, "A method to produce and validate a digitally reconstructed radiograph-based computer simulation for optimisation of chest radiographs acquired with a computed radiography imaging system.," *The British Journal of Radiology*, vol. 84, pp. 890–902, 2011.

[31] G. Sherouse, K. Novins, and E. Chaney, "Computation of digitally reconstructed radiographs for use in radiotherapy treatment design," *Int. J. Radiat. Oncol. Biol. Phys.*, vol. 18, pp. 651–658, 1990.

[32] N. Milickovic, D. Baltast, S. Giannouli, M. Lahanas, and N. Zamboglou, "CT imaging based digitally reconstructed radiographs and their application in brachytherapy.," *Phys. Med. Biol.*, vol. 45, pp. 2787–2800, 2000.

[33] S. Chen, W. Jong, and A. Harun, "Evaluation of x-ray beam quality based on measurements and estimations using SpekCalc and IPEM78 models," *Malaysian Journal of Medical Sciences*, vol. 19, pp. 22–28, 2012.

[34] G. Poludniowski, G. Landry, F. DeBlois, P. M. Evans, and F. Verhaegen, "SpekCalc: A program to calculate photon spectra from tungsten anode x-ray tubes.," *Phys. Med. Biol.*, vol. 54, pp. N433–N438, 2009.

[35] G. G. Poludniowski and P. M. Evans, "Calculation of x-ray spectra emerging from an x-ray tube. Part I. Electron penetration characteristics in x-ray targets," *Med. Phys.*, vol. 34, pp. 2164–2174, 2007.

[36] G. G. Poludniowski, "Calculation of x-ray spectra emerging from an x-ray tube. Part II. X-ray production and filtration in x-ray targets," *Med. Phys.*, vol. 34, pp. 2175–2186, 2007.

[37] E. Mainegra-Hing and I. Kawrakow, "Efficient x-ray tube simulations," *Med. Phys.*, vol. 33, pp. 2683–2690, 2006.

[38] "CIRS Model 062M User Guide & Technical Information," tech. rep., CIRS Inc., Norfolk, Va, 2008.

[39] "Catphan 504 Manual," tech. rep., The Phantom Laboratory, Greenwich, NY, 2012.

[40] M. Berger, J. Hubbell, S. Seltzer, J. Chang, J. Coursey, R. Sukumar, D. Zucker, and K. Olsen, "XCOM: Photon Cross Section Database (version 1.5)," 2010.